Optical Coherence Tomography: Light Scattering and Imaging Enhancement

16

Ruikang K. Wang and Valery V. Tuchin

Contents

R.K. Wang (✉)
University of Washington, Seattle, WA, USA
e-mail: wangrk@u.washington.edu

V.V. Tuchin
Department of Optics and Biophotonics, Saratov State University, Saratov, Russian Federation

Precision Mechanics and Control, Institute of the Russian Academy of Sciences, Saratov, Russian Federation

Optoelectronics and Measurement Techniques Laboratory, University of Oulu, Oulu, Finland
e-mail: tuchinvv@mail.ru

V.V. Tuchin (ed.), *Handbook of Coherent-Domain Optical Methods*,
DOI 10.1007/978-1-4614-5176-1_16, © Springer Science+Business Media New York 2013

Abstract

The fundamental aspects of optical coherence tomography and a brief description of its applications in medicine and biology are presented. The impact of multiple scattering in tissues on OCT imaging performance, and developments in reducing the overwhelming multiple scattering effects and improving imaging capabilities by the use of immersion technique are discussed. A novel technique based on the use of biocompatible and hyperosmotic chemical agents to impregnate the tissue and to enhance the OCT images is described. The mechanisms for improvements in imaging depth and contrast are discussed, primarily through the experimental examples.

16.1 Introduction

Over the last two decades, noninvasive or minimally invasive spectroscopy and imaging have witnessed widespread and exciting applications in biomedical diagnostics. Optical techniques that use the intrinsic optical properties of biological tissues, such as light scattering, absorption, polarization, and autofluorescence, have many advantages over the conventional X-ray computed tomography, MRI, and ultrasound imaging in terms of safety, cost, contrast, and resolution features. Time-resolved and phase-resolved optical techniques are capable of deep-imaging of the tissues that could provide information of tissue oxygenation states and detect brain and breast tumors [1, 2], whereas confocal microscopy and multi-photon excitation imaging have been used to show cellular and subcellular details of superficial living tissues [3, 4]. However, most biological tissues strongly scatter the probing light within the visible and near-infrared range, i.e., the therapeutic and/or diagnostic optical window. The multiple scattering of light is severely detrimental to imaging contrast and resolution, which limits the effective probing depth to several hundred micrometers for the confocal microscopy and multi-photon excitation imaging techniques. However, some clinical applications, such as early cancer diagnosis, require the visualization of intermediate depth range of the localized anatomical structures with micron-scale resolution.

Optical coherence tomography (OCT) fills a nice niche in this regard. It uses low-coherence interferometry to image internal tissue structures to the depth up to 2 mm with micron-scale resolution [5, 6]. Its first applications in medicine were reported more than 20 year ago [7–11], but its roots lie in early work on white-light

interferometry that led to the development of optical coherence-domain reflectometry (OCDR), a one-dimensional optical ranging technique [12]. Although OCDR was developed originally for finding faults in fiber-optic cables and network components [13], its ability to probe the eye [14–16] and other biological tissues [17] was soon realized. The superb axial resolution is achieved by exploiting the short temporal coherence of a broadband light source. Borrowing the concept of confocal microscopy, OCDR was quickly extended to section the biological tissues [7] through the point-by-point scan, so-called optical coherence tomography. OCT enables microscopic structures in biological tissue to be visualized at a depth beyond the reach of conventional confocal microscopes. Probing depth exceeding 2 cm has been reported for transparent tissues, including the eye [18] and frog embryo [19]. To date, successful stories of in vitro and in vivo OCT applications in medicine have been delivered in a wide number of areas, for example, ophthalmology [20], gastrointestinal tract [21–25], dental [26], and dermatology [27–29]. OCT is becoming viable as a clinical diagnostic tool with the recent advent of high-power, low-coherence sources and near real-time image scanning technology [30]. The high resolution (<10 μm) and high dynamic range (>100 dB) of OCT would allow for in vivo tissue imaging approaching the resolution of excisional biopsy. An advantage that OCT has over high-frequency ultrasonic imaging, a competing technology that achieves greater imaging depths but with low resolution [31], is its relative simplicity and cost-effectiveness of the hardware on which OCT systems are based.

This chapter introduces the fundamental aspects of optical coherence tomography and briefly discusses its applications in medicine and biology. In the later parts of chapter, we will discuss how multiple scattering of tissue would impact the OCT imaging performance, and the developments in reducing the overwhelming multiple scattering effects and improving imaging capabilities by the use of immersion techniques.

16.2 Optical Coherence Tomography: The Techniques

16.2.1 Introduction

OCT is analogous to ultrasonic imaging that measures the intensity of reflected infrared light rather than reflected sound waves from the sample. Time gating is employed so that the time for the light to be reflected back, or echo delay time, is used to assess the intensity of backreflection as a function of depth. Unlike ultrasound, the echo time delay of an order of femtosecond cannot be measured electronically due to the high speed associated with the propagation of light. Therefore, the time-of-flight technique has to be engaged to measure such ultrashort time delay of light backreflected from the different depth of sample. OCT uses an optical interferometer to solve this problem. Central to OCT is a low-coherence optical reflectometry (LCR) that can be realized by a Michelson or a Mach-Zehnder interferometer illuminated by a low coherent light source.

16.2.2 Low Coherence Reflectometry

LCR, or "white light interference," has been used for centuries in industrial metrology, e.g., to measure the thickness of thin film [32], as a position sensor [33], and with other measurands that can be converted to a displacement [34]. At present, all OCT techniques use LCR to obtain the depth-resolved information of a sample, an example of which is shown in Fig. 16.1.

One arm of the interferometer is replaced by the sample under measurement. The reference mirror is translated with a constant velocity v_r to produce interference modulation with Doppler frequency $f_D = 2v_r/\lambda_0$ for optical heterodyne detection, where λ_0 is the central wavelength of a low-coherence light source. Then the interference can occur only when the optical path lengths of light in both the sample arm and reference arm are matched to within the coherence length of light source.

The principle of LCR can be analyzed in terms of the theory of two-beam interference for partially coherent light. Assuming that the polarization effects of light are neglected, $E_s(t - L_s/c)$ and $E_r(t - L_r/c)$ are scalar complex functions that represent the light fields from the sample and reference arms of a Michelson interferometer, respectively. L_s and L_r are the corresponding optical path lengths. Given the assumption that the photodetector captures all of the light from the reference and sample arms, due to time invariance of the light field, the resultant intensity at detector PD is then:

$$I_d(\tau) = \langle [E_s(t) + E_r(t+\tau)][E_s(t) + E_r(t+\tau)]^* \rangle, \tag{16.1}$$

where the angular brackets denote the time average over the integration time at the detector; $\tau = \Delta L/c$ is the time delay corresponding to the round-trip optical path length difference between the two beams, i.e., $\Delta L = L_s - L_r = 2n_0(l_{s0} - l_{r0})$; $n_o \cong 1$, is the refractive index of air; and l_{s0} and l_{r0} are the geometric lengths of two arms, as indicated in Fig. 16.1. Because $I_s = \langle E_s(t)E_s^*(t) \rangle$ and $I_r = \langle E_r(t+\tau)E_r^*(t+\tau) \rangle$, equation (16.1) can then be written as:

$$I_d(\tau) = I_s + I_r + 2\mathrm{Re}\{<E_s(t)E_r^*(t+\tau)>\}. \tag{16.2}$$

The last term in the above equation, which depends on the optical time delay τ set by the position of the reference mirror, represents the amplitude of interference fringes that carry information about the structures in the sample. The nature of the interference fringes, or whether any fringes form at all, depends on the degree to which the temporal and spatial characteristics of E_s and E_r match. Thus, the interference functions as a cross-correlator and the amplitude of interference signal generated after integration on the surface of the detector provides a measure of the cross-correlation amplitude. The first two terms in (16.1) contribute to the dc signal only in the interference signal detected by photodetector. To facilitate the separation of cross-correlation amplitude from the dc component of detected intensity, various techniques have been realized to modulate the optical time delay, i.e., τ. A few of these techniques will be discussed later.

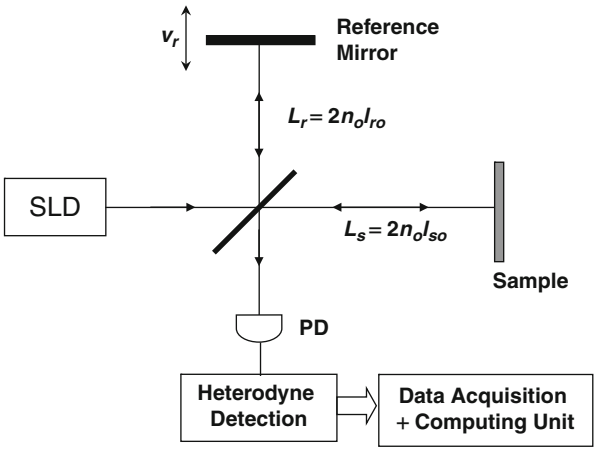

Fig. 16.1 Schematic of low-coherence interferometer

Under the assumption that the sample behaves as a perfect mirror that leaves the sample beam unchanged, the correlation amplitude depends on the temporal-coherence characteristics of the source, according to

$$\mathrm{Re}\{<E_s(t)E_r^*(t+\tau)>\} = |G(\tau)|\cos[2\pi f_0\tau + \phi(\tau)], \tag{16.3}$$

where is the central frequency of the source with c the speed of light, and $G(\tau)$ is its complex temporal coherence function with an argument of $\phi(\tau)$. According to the Wiener-Khinchin theorem, $G(\tau)$ is related to the power spectral density of the source, $S(f)$, as [35, 36]

$$G(\tau) = \int_0^\infty S(f)\exp(-j2\pi\tau)df. \tag{16.4}$$

It follows from this relationship that the shape and width of the emission spectrum of the light source are important variables in the low-coherence interferometry, and thereby OCT, because of their influence on the sensitivity of the interferometer to the optical path length difference between the sampling and reference arms. Light sources with broad bandwidth are desirable because they produce interference signals of short temporal extent. The relationship between $S(f)$ and $G(\tau)$ can be seen clearly when both are represented by Gaussian functions:

$$S(f) \leftrightarrow G(\tau) \tag{16.5}$$

with

$$S(f) = \frac{2\sqrt{\ln 2/\pi}}{\Delta f}\exp\left[-4\ln 2\left(\frac{f-f_0}{\Delta f}\right)^2\right], \tag{16.6}$$

and

$$G(\tau) = \exp\left[-\left(\frac{\pi \Delta f \tau}{2\sqrt{\ln 2}}\right)^2\right] \exp(-j2\pi f_{0\tau}). \tag{16.7}$$

In these equations, the full-width-half-maximum bandwidth Δf represents the spectral width of the source in the optical frequency domain. The corresponding measure of the correlation width, derived from (16.7), is the correlation length (in free space), given by

$$l_c = \frac{2c \ln 2}{\pi} \cdot \frac{1}{\Delta f} \approx 0.44 \frac{\lambda_0^2}{\Delta \lambda}, \tag{16.8}$$

where $\Delta\lambda$ is the full-width of the coherence function at half-maximum measured in wavelength units. Other definitions of the coherence length yield similar expressions, but with a different constant factor. For example, defined as the speed of light in medium times the area under the squared amplitude of the normalized temporal coherence function, $l_c \approx 0.66\, \lambda_0^2/\Delta\lambda$ [35]. In the OCT community, (16.8) is often used.

16.2.3 Noise

One of the main noise sources in LCR is mechanical $1/f$ noise. To achieve shot-noise-limited detection, a heterodyne technique can be used. The most straightforward and simplest technique in optics is to use the Doppler effect, e.g., simply moving the reference mirror with constant speed v. Thus the time delay will be

$$\tau = \frac{2vt}{c}. \tag{16.9}$$

Then we have the ac term of detected interference signal time-modulated by

$$\mathrm{Re}\{<E_s(t)E_r^*(t+\tau)>\} = |G(\tau)| \cos[4\pi f_0 vt/c + \phi(\tau)]. \tag{16.10}$$

From here, the central Doppler frequency will be

$$f = \frac{2f_0 v}{c} = \frac{2v}{\lambda_0}. \tag{16.11}$$

Figure 16.2a shows an example of a time-modulated interference signal detected by the photodetector. The detected ac signal is bandpass filtered with respect to the central Doppler frequency as the center frequency, then rectified and low-pass filtered. The output of the low-pass filter is the envelope of the time-modulated ac interference signal, which is equivalent to the cross-correlation amplitude

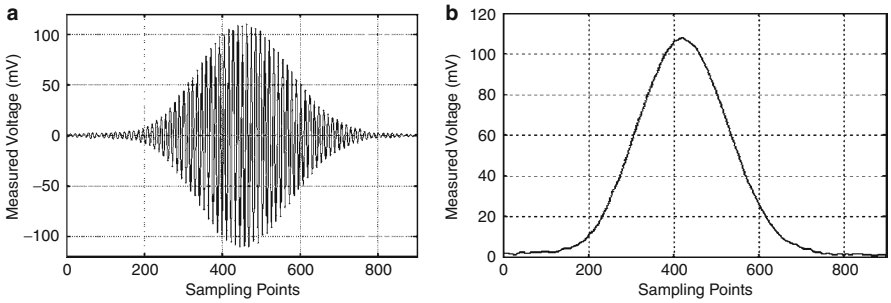

Fig. 16.2 (**a**) Time-modulated ac term of interference signal, (**b**) corresponding cross-correlation amplitude, i.e., envelope

mentioned above. Figure 16.2b gives an example of the detected envelope corresponding to Fig. 16.2a.

In addition to $1/f$ noise, there are several other noise sources such as quantum noise, shot noise, and electronic noise. The impact of these noise disturbances on the measurement can be described by signal-to-noise ratio (SNR), which is the ratio of the expected mean photocurrent power to its standard deviation. The dynamic range (DR) of an instrument is defined by the ratio of the maximum to the minimum measurable photocurrent power P of the interference signal:

$$DR = 10\log\frac{P_{\max}}{P_{\min}} = 10\log(SNR_{\max}). \tag{16.12}$$

Photocurrent power P is proportional to the square of the light intensity impinging at the photodetector, hence

$$\frac{P_{\max}}{P_{\min}} = \frac{R_{\max}^2}{R_{\min}^2} = \frac{1}{R_{\min}^2} \quad \Rightarrow DR = -20\log(R_{\min}), \tag{16.13}$$

where $R_{\min}$ is the minimal reflectivity in the sample beam producing a photodetector signal power equal to the standard deviation of the photocurrent power generated by a reflectivity of $R_{\max} = 1$. In case of LCR and OCT, the intensity at photodetector is caused by the interference of the sample beam with the reference beam. Hence, according to the interference law, the signal intensity at the photodetector is proportional to the square root of the object intensity and we have in this case:

$$DR = -10\log(R_{\min}). \tag{16.14}$$

The LCR and OCT have been designed near the shot noise limit by choosing a proper Doppler frequency to avoid low frequency $1/f$ noise [13], a proper balanced-detector scheme to reduce the excess photon noise [37], and a proper

transimpedance amplifier resistance voltage to overcome thermal noise [38]. The simplest method for choosing a proper Doppler frequency is to mount the reference mirror on a linear translation stage moving at a chosen constant velocity. The other methods include the fiber stretching via a piezoelectric crystal [39], and frequency domain scanning by introduction of a grating-based phase control delay line [40].

16.2.4 Optical Coherence Tomography

Optical coherence tomography performs cross-sectional imaging by measuring the time delay and magnitude of optical echoes at different transverse positions, essentially by the use of a low-coherence interferometry. A cross-sectional image is acquired by performing successive rapid axial measurements while transversely scanning the incident sample beam onto the sample (see Fig. 16.3). The result is a two-dimensional data set, which represents the optical reflection or backscattering strength in a cross-sectional plane through a material or biological tissue. OCT was first demonstrated in 1991 [7]. Imaging was performed in vitro in the human retina and in atherosclerotic plaque as examples of imaging in transparent, weakly scattering media, as well as highly scattering media. The system implemented by the optic fiber couplers, matured in the telecommunication industry, offers the most advantage for the OCT imaging of biological tissues because it can be integrated into almost all currently available medical imaging modalities, for example, endoscope and microscope. Figure 16.4 gives an example of the optic-fiber versions of OCT [25, 29]. In this type of optic-fiber version of interferometer, light from a low-coherence light source is coupled to a single-mode fiber coupler where half of light power is conducted through the single-mode fiber to the reference mirror. The remaining half enters the sample via proper focusing optics. The distal end of the fiber in the sample arm serves a dual role as a coherent light receiver and spatial filter analogous to a confocal pinhole. Because the dc signal and intensity noise generated by the light from the reference arm add to the interference signal, it makes the system prone to the photon excess noise. One way to reduce this type of noise is to use a balanced detection configuration as shown in Fig. 16.4 that would make the background noise components cancelled by subtracting the photocurrents generated by two photodetectors. The interference signals at the output of the detectors add because they vary out of phase [50].

OCT has the advantage that it can achieve very high axial image resolution independent of the transverse image resolution. The axial resolution is determined by the coherence length of light source used, i.e., (16.8), which is independent of the sampling beam focusing conditions. From (16.8), the axial resolution is inversely proportional to the spectral bandwidth of light source. Thus, the higher axial resolution can be achieved by the use of a wider spectral bandwidth of light sources. Table 16.1 lists characteristics of a variety light sources suitable for use in OCT systems [6]. The most commonly used sources in the current OCT systems are the superluminescent diodes (SLDs) with peak emission wavelengths in either 820 nm

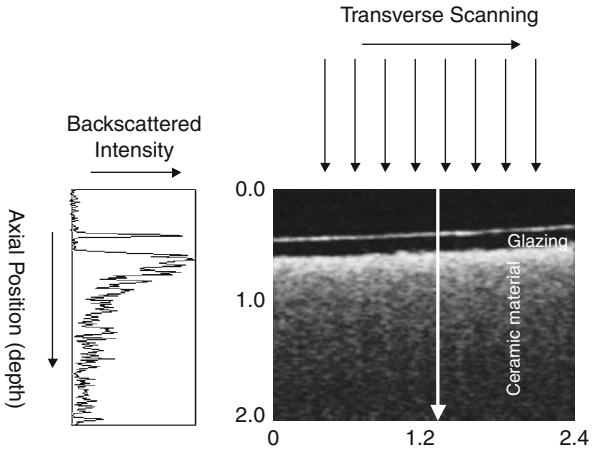

Fig. 16.3 OCT images are generated by performing measurements of the echo time delay and magnitude of back-scattered light over a range of transverse positions. OCT are two- or three-dimensional data sets that represent the optical backscattering in a cross section or volume of the tissue (Courtesy of Cranfield Biophotonics Group)

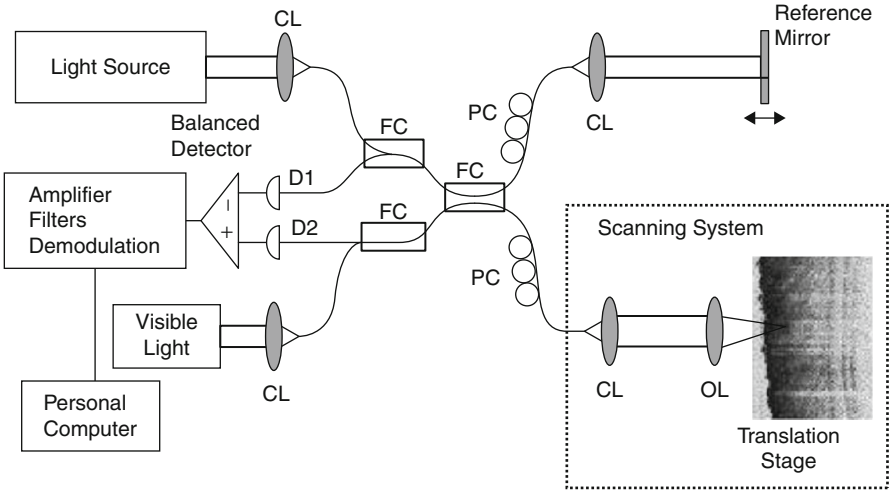

Fig. 16.4 Example of the fiber-optic versions of OCT systems where *CL* is the collimating lens, *FC* the fiber coupler, *PC* the polarization controller, *OL* the objective lens, and *D* the detector

or 1,300 nm fiber-optic telecommunication bands because of their high irradiance, compactness, and relatively low cost. However, the spectral bandwidth of the available SLDs is usually limited, which determines the achievable axial resolution at 7–10 μm for 800 nm and 10–20 μm for 1,300 nm band light sources, which are sometimes not sufficient to meet the resolution requirement for some medical and industrial applications. In order to enhance the axial resolution, a light source with broader spectral bandwidth has to be applied. Researchers attempted to integrate a number of SLDs with non-overlapping central wavelengths into a single broadband source for resolution improvement [41], but the improvement is suboptimal in

Table 16.1 Low-coherence light sources suitable for use in OCT systems

Light source	Central wavelength (nm)	Bandwidth (nm)	Emission power	Reference
Edge-emitting LED	1,300, 1,550	50–100	20–300 μW	[53]
SLD	800, 1,300	20–50	1–10 mW	[41]
Multiple QW	800	90	15 mW	[55]
LED/SLD	1,480	90	5 mW	[56]
Laser-pumped fluorescent organic dye	590	40	9 mW	[54]
Mode-locked Ti:Al_2O_3 laser	820	50–200	400 mW	[42]
Mode-locked Cr^{4+}forsterite laser	1,280	75	30 mW	[42]
Superfluorescent optical fibers:				
Er-doped	1,550	40–80	10–100 mW	[52]
Tm-doped	1,800	80	7 mW	[52]
Nd-/Yb-doped	1,060	65	108 mW	[51]
Supercontinuum	Selectable	200–300	2 W	[49]

terms of emitting wavelength of the multiplexed SLD that is typically centered at >900 nm, overlapping the water absorption at 980 nm that may affect the imaging depth. A number of reports (e.g., [11, 42–44]) have demonstrated the use of state-of-the-art femtosecond lasers to achieve a 2–3 μm axial resolution, but with the disadvantage of being expensive and bulky limits its uses to a few research laboratories. Being spectrally very broad and visually very bright, supercontinuum (SC) light sources have attracted notice as an excellent alternative for OCT imaging to achieve subcellular axial resolution [45–49]. There have also been developments in diode-pumped superfluorescent fiber sources [51, 52] that gained attention because of their low cost and compactness. The high power and wide bandwidth of these light sources make them attractive alternatives for fast, high-resolution OCT imaging of in vivo biological tissues.

The lateral or transverse resolution achieved with an OCT imaging system is determined by the focused spot size limited by the numerical aperture of the lens used to deliver the light onto the sample, and the optical frequency of incident light as in conventional microscopy [57]. The transverse resolution can be written

$$\Delta x = \frac{4\lambda f}{\pi d}, \tag{16.15}$$

where d is the spot size on the objective lens and f is its focal length. High transverse resolution can be achieved by the use of a large numerical aperture of lens and focusing the beam to a small spot size. In addition, the transverse resolution is also related to the depth of focus or confocal parameter, b. The confocal parameter is

twice the Raleigh range, $2z_R$. Its relationship to transverse resolution is described by the formula:

$$b = 2z_R = \pi\Delta x^2/2\lambda. \tag{16.16}$$

In addition to its high-resolution feature, advantages of OCT for medical imaging include its broad dynamic range, rapid data acquisition rate, and compact portable structure. The frame rates for OCT systems are currently at four to eight frames per second [40]. At the beginning of OCT development, the path length in the reference arm was scanned via the use of a moving mirror or galvanometer [7]. However, such scanning would require approximately 40 s to perform imaging of non-transparent tissue [58]. A system similar to this is still in use for imaging the transparent tissue of the eye, and sometimes is sufficient for use as a research tool. Fiber-stretching with a piezoelectric crystal [28] in the reference arm offers a rapid scanning of the optical path length. However, there are disadvantages in the use of such technique, including polarization mode dispersion, hysteresis, crystal breakdown, and high voltage requirement. Presently, the most popular OCT systems employ a variable optical group delay in the reference arm through the introduction of a grating-based phase control delay line [39]. This configuration was originally designed for shaping femtosecond pulses that employ a grating-lens combination and an oscillating mirror to form an optical delay line [59]. It was reported to achieve high data acquisition rates up to 4–8 frames per second [61]. In addition to its high data acquisition rate, the system has two other advantages over the previous configurations. The optical group delay can be varied separately from the phase delay, and the group velocity dispersion can be varied without the introduction of a separate prism [60, 61].

The OCT system described above is the backbone of current OCT system developments, particularly in stimulating new concepts and ideas. This is usually called the time domain approach (TDOCT), i.e., the first generation of the OCT development. There are varieties of other systems developed that operate at different domains or reveal different functionalities of the tissue, but essentially the same mechanism, for example, dual beam OCT [8, 62], en-face OCT [63, 64] (see also ▶ Chap. 19), Fourier domain OCT [65–67], whole-field OCT [68, 69], and functional OCT including polarization sensitive OCT [70–72] (see also ▶ Chap. 21), Doppler OCT [73–78] (see also ▶ Chap. 22), and spectroscopic OCT [79]. For detailed information regarding the different forms of OCT systems, please refer to recent comprehensive review papers [80, 81] and a monograph [82].

With the current shift of OCT application to in vivo imaging applications, one of the most important parameters that must be considered is the imaging speed, because the faster the imaging speed, the better we can manage to minimize the motion artifacts that are inevitable for any in vivo imaging applications. Being the first generation, TDOCT is capable of only up to ~8,000 A-lines per second (with most systems having up to 2 kHz A-scan rate), which is mainly restricted by the employment of a mechanically scanning mirror in the reference arm to provide

depth-resolved axial information of the sample. With this imaging speed, it is sometimes difficult for TDOCT to achieve in vivo 3D scanning. For example, in retinal imaging, only several cross-sectional images could be captured before eye blinking and movements happen [83], which is inevitable for human studies. To increase the imaging speed, a new interferogram detection scheme, Fourier domain OCT (FDOCT), is proposed to directly achieve depth-resolved reconstruction of the biological tissue without the need of mechanically scanning the reference arm [66, 84], a development that represents the second OCT generation (2gOCT). In FDOCT, the interference spectrograms are detected either with a broadband light source and a high-speed spectrometer (i.e., spectral domain OCT [SDOCT]) [66, 84] or a wavelength swept laser and ultrahigh-speed photodetector (swept source OCT [SSOCT]) [85, 86]. Compared with TDOCT, FDOCT has proven to have dramatically improved system sensitivity [87–89], thereby affording much higher imaging speed without losing useful information about the sample. Beginning in 2002 [90], FDOCT has gradually become dominant in OCT development [91–97], allowing a scanning rate at dozens of kilo-A-lines per second (up to ~40 kHz). With this imaging speed, it is possible to visualize the sample in a 3D mode, offering much flexibility in the comprehensive analysis and quantification of the sampled volume. In addition, based on the high-speed FDOCT, several novel imaging processing algorithms have been made possible to achieve in vivo 3D functional imaging of the tissue sample, for example, the blood flow and microvasculature imaging [98–110].

Although 2gOCT has been demonstrated great success in the past few years, the imaging speed is still a barrier to achieve satisfactory 3D imaging on untrained patients due to the inevitable motion during the in vivo imaging. It is now clear that one of the solutions to reduce the motion artifacts in the final results is to further improve the system imaging speed. Recently, the ultrahigh-speed (hundreds of kHz line rate) FDOCT system (the third-generation (3 g) OCT) has become increasingly attractive by employing the frequency domain mode locking (FDML) technology [111–114] in SSOCT and high-speed line scan CMOS camera in SDOCT [115–117]. For example, the 20-MHz system based on a 1,310 nm swept laser source was demonstrated in Ref. [118]. At a different operating wavelength, the 1.3-MHz 1,050 nm system was reported in Ref. [119]. So far, the fastest retinal FDOCT system, which can maintain both the high axial resolution (~7 μm) and the ultrafast imaging speed, is reported in Ref. [111], in which the authors developed an 1-μm SSOCT system running at ~400 k-A-lines per second, realized by combining FDML with a multi-spot detection strategy. It is reported that it is possible with this system to further improve imaging speed to 684 kHz [119]. However, the commercial utilization of such SSOCT is yet to be approved by the FDA. Currently, the commercially available retinal OCT systems are still based on SDOCT, with the imaging speed directly determined by the camera employed in the spectrometer. Until now, the fastest retinal SDOCT system reported is a system working at a 312 kHz A-line rate [115]. However, to reach 312 kHz, it has to sacrifice the spectral resolution by using a part of the CMOS sensor array (576 pixels out of 4,096 pixels). In consequence, the detectable depth is shallow (~2 mm in air) and

the system sensitivity rolling off is relatively high (~25 dB over 2-mm ranging distance). To further increase the imaging speed while maintaining the system axial resolution at less than 10 μm, the acceptable performances, e.g., system sensitivity rolling off and detectable depth range, are still a challenge in the development of a retinal SDOCT system.

16.3 OCT in Imaging

16.3.1 Introduction

OCT was originally developed to image the transparent tissue of the eye at unprecedented resolution [7]. It has been used clinically to evaluate a wide range of retinal-macular diseases [120–122]. Recently, the technology has been advanced to image nontransparent tissue, where penetration of light is limited [125, 126]. Nontransparent tissue has high light scattering in nature, which limits the light penetration depth for OCT imaging. To partially resolve this problem, most OCT imaging of nontransparent tissues is implemented with light having an incident wavelength near 1,300 nm, rather than 820 nm used in the relatively transparent tissues. At the wavelength of 1,300 nm, light scattering is low relative to scattering of light in the visible region. Absorption is low because this wavelength is too long to result in large amounts of electron transitions but is too short to induce extensive vibrational transitions in water. Another method to enhance the OCT imaging depth for nontransparent tissue is to use the immersion technique to interrogate the tissue with biocompatible chemical agents. This will be described later in this chapter.

16.3.2 Ophthalmology

Due to the relatively transparent nature of human eye tissue to near-infrared light, its weakly scattering structures, including the retina, can be imaged by OCT to the full depth with a resolution at 20 μm without difficulty [8, 18, 19, 127, 128]. The diagnostic potential of OCT for non-contact biometry segment of abnormalities of the eye was first demonstrated by Izatt et al. [16]. Using the reflectometer technique at a central wavelength of 1,310 nm, structures such as cornea, sclera, iris, and lens anterior capsule can be clearly visualized. With the 820 nm central wavelength, detailed layered structures within the human retina can now be delineated with high resolution. See Fig. 16.5 for examples.

Many retinal diseases are accompanied by changes in retinal thickness. Hence, high depth resolution is an important feature of any imaging techniques used to diagnose retinal pathology. Current diagnostic tools such as the confocal scanning ophthalmoscope are limited to a depth resolution no better than 300 μm [129]. Towards this, OCT offers a great potential to advance the diagnostic techniques because of its high resolution. Using a wavelength of 830 nm, it can easily differentiate the large-scale anatomical features, such as the fovea, optic disk, and

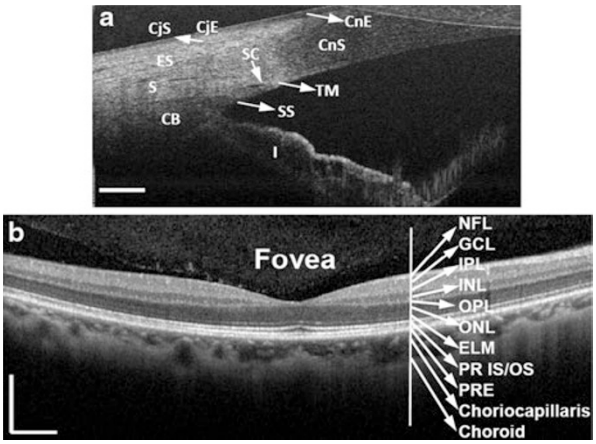

Fig. 16.5 (**a**) In vivo microstructure imaging of the human corneo-scleral limbus from a temporal location, where CnE, corneal epithelium; CnS, corneal stroma; CjE, conjunctival epithelium; CjS, conjunctival stroma; ES, episclera; S, sclera; SS, scleral spur; CB, ciliary body; I, iris; TM, trabecular meshwork; SC, Schlemm's canal. (**b**) In vivo OCT reveals detailed morphological features within retina and choroid, where NFL, Nerve fiber layer; GCL, ganglion cell layer; IPL, inner plexiform layer; INL, inner nuclear layer; OPL, outer plexiform layer; ONL, outer nuclear layer; ELM, external limiting membrane; PR IS/OS, photoreceptor inner and outer segments; RPE, retinal pigment epithelium. The scale bar represents 500 μm (Courtesy of Biophotonics and Imaging Laboratory, University of Washington)

retinal profiles. It can also quantitatively assess retinal thickening caused by macular edema and other diseases. Further studies have shown that the potential of OCT to quantify the amount of serous retinal detachments, macular holes, and macular edema, [130, 131] and to assess glaucoma [132].

With the use of a laboratory-based ultra-broadband femtosecond titanium–sapphire laser light source, an axial resolution of OCT for ophthalmologic applications has been recently advanced to about 1–3 μm [133, 134], enabling unprecedented in vivo imaging of intraretinal subcellular structures. The availability of this technology for clinical research and patient care will depend mainly on the availability of suitable sources for ultra-broad-bandwidth light, but it will no doubt have enormous impact on the future care of our vision.

16.3.3 Developmental Biology

Some of the exciting applications of OCT have occurred in the basic science of developmental biology. Studies have shown the promises of OCT to monitor in real time the developing neural and embryonic morphology [19, 29, 136–143] of *Xenopus laevis, Rana pipiens, Brachydanio rerio*, and chicken and rodent embyros.

Figure 16.6 shows in vivo 3D OCT images scanned from a 5-day-old chicken embryo, the time point at which its heart is nearly proper formed. The images have

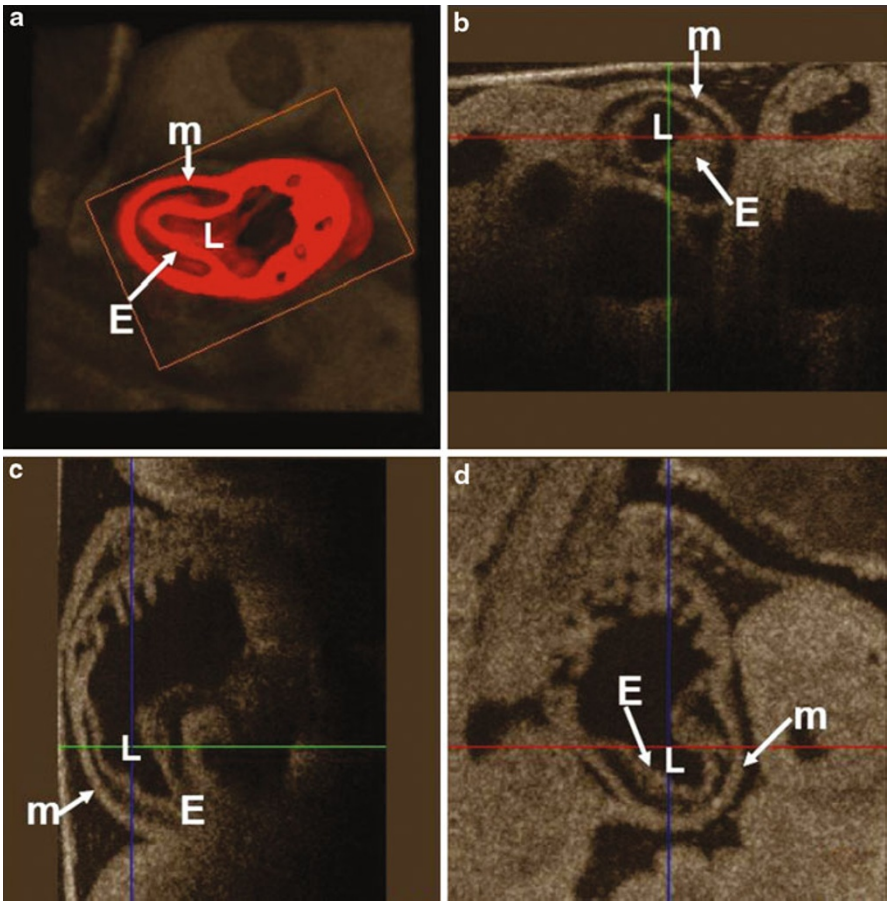

Fig. 16.6 In vivo 3D OCT images scanned from a 5-day-old chicken embryo. The 3D dataset enables the accurate segmentation of the heart, as shown in (**a**): (**b**) the sagittal scan, (**c**) the longitudinal scan, and (**d**) the transverse scan, where *m* denotes the myocardium, *E* the endocardium, and *L* the lumen (Courtesy of Biophotonics and Imaging Laboratory, University of Washington)

resolutions of 8 μm (axial) and 20 μm (transversal) where the gray level corresponds to the logarithm of back-scattered light intensity collected by the optical system, with white representing the highest backscattered signal. These images show high-resolution details of pathologically important internal structures, including myocardium, endocardium, and lumen.

The current imaging speed of the OCT system of more than hundreds of kilo-Hz enables the dynamic heart microstructures to be captured in vivo at the early development stage, useful for further understanding of the dynamic interaction of genetic and environmental factors that determine the generation of the basic elements, such as cells, extracellular matrix, adhesion molecules, and how these

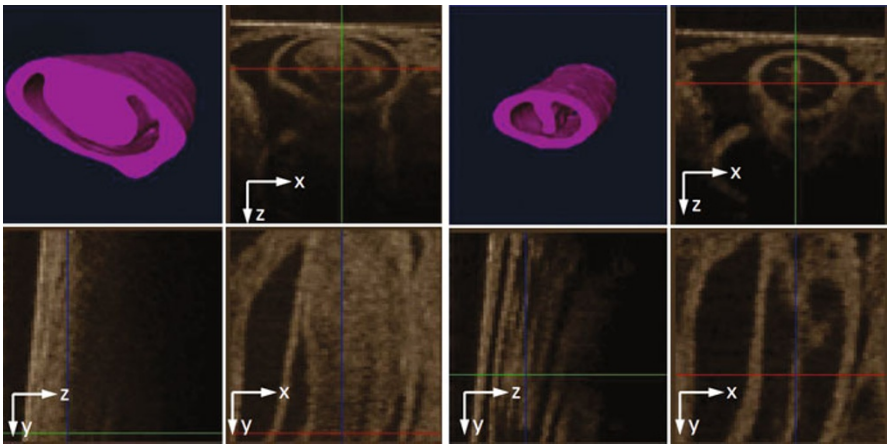

Fig. 16.7 High-speed OCT system enables 3D imaging of chicken embryos at the early development stage. Shown are the 3D images captured at the time instant when the out-flow tract was maximally dilated (*left panel*) and maximally constricted (*right panel*) (Courtesy of Biophotonics and Imaging Laboratory, University of Washington)

basic elements are assembled into a properly functional heart. Figure 16.7 illustrates results obtained from a 92-kHz OCT system that captures the beating heart of a chicken embryo at 3 days old, at the time point when the heart is merely in a form of a tube, the so-called out-flow-tract (OFT). With the help of post-data processing, 4D non-gated cardiac OCT images can be synchronized to obtain useful morphological information of the dynamic heart [140]. Figure 16.7a shows the 3D OCT image captured at the time instant when the chick OFT was maximally dilated, while Fig. 16.7d demarcates the 3D image captured when the OFT was maximally constricted. Although the current OCT system does not permit the imaging of individual cells due to its limited resolution, it performs well in imaging larger tissue and organ morphology, the structures that are too large to image in vivo with confocal microscopy. The above results demonstrate that OCT has applications to developmental biology because it can image biological species noninvasively and in real time. Such noninvasive 3D imaging of the embryonic internal organs could make OCT a powerful monitoring tool for developmental biology.

16.3.4 Dermatology

Dermatology appeared to be another promising application field for OCT due to the obvious ease of access [27]. However, it turned out that skin is a much less favorable subject for OCT imaging than previously thought because of strong scattering of the probe light and poor optical contrast between structural components in clinically important areas. OCT penetration depth covers the stratum corneum, the living epidermis, and the dermis consisting mainly of a network of collagen and elastin fibers and fibroblasts. Nevertheless, it does offer potential for

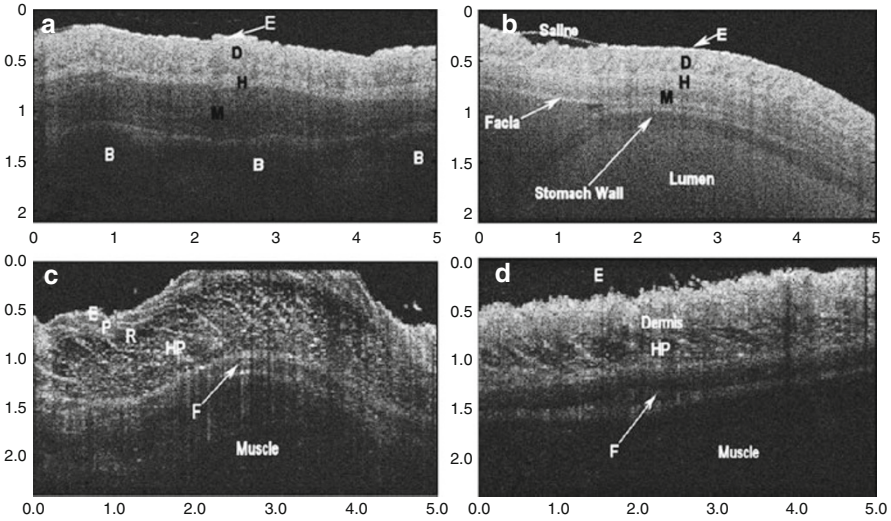

Fig. 16.8 Seeing through the rat skin with high resolution: (**a**) at the chest site and (**b**) at the abdomen site. (**c**, **d**) high-resolution imaging of pathological skin layers and features [29]

early detection of malignant melanoma [144, 145]. However, the successful application to this problem will depend on establishing correlations with the standard histopathology through a vast amount of experimental studies. Whether sufficient optical contrast exists between normal and pathological tissue at a cellular scale is a critical question that needs to be addressed in the future.

Figure 16.8 illustrates the ex vivo OCT images from a 5-day-old rat at (a) the chest and (b) the abdomen. It clearly demonstrates that OCT has the capability of seeing through the skin of the species with high resolution. Different layers and features starting from skin surface are delineated sharply, including epidermis (E), dermis (D), hypodermis (H), muscle (M), fascia (F), bone (B), stomach, hair follicles, and other features.

High-resolution delineation of the skin structures with OCT are shown in Fig. 16.8c, d, where a whole body of an adult Wistar rat was used in the experiments. Skin imaging with OCT has traditional difficulties because of the skin has high scattering properties to the near-infrared light which limit light penetration into deep skin. To reduce the light scattering in the skin, chemical agents were used in the experiments, including glycerol and propylene glycol, agents known to provide a bed for refractive index matching inside the superficial tissue [29, 184]. After topical applications of the chemical agent solutions onto the skin surface, OCT imaging allows us to visualize clearly the different layers and features in the skin, including epidermis (E), epidermal basement (EB), papillary dermis (P), reticular dermis (R), hypodermis (HP), fascia (F), muscle, and hair follicles. Far more detailed structures are delineated in the dermis zone. Note that the experiments were done with topical applications of glycerol solution, Fig. 16.8c, and propylene glycol solution, Fig. 16.8d.

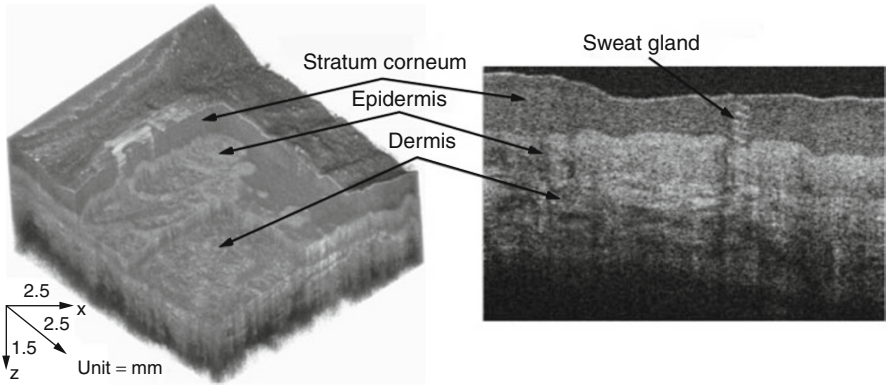

Fig. 16.9 High-resolution visualization of human skin layers and features in vivo (Courtesy of Biophotonics and Imaging Laboratory, University of Washington)

With the advancement of continuous OCT development in terms of imaging speed and spatial resolution, it is now possible to image detailed pathological features and important layers within the human skin in vivo. Figure 16.9 shows such an example captured using a 1,310 nm OCT system with 180 kHz A-scan rate and ~5 μm spatial resolutions from a human palm region of a volunteer. The powerful ability of OCT in delineating the microstructures within skin promises future clinical utility of OCT in the diagnosis, treatment, and management of skin diseases, such as cancer, port-wine stain, and psoriasis.

16.3.5 Gastroenterology

Gastrointestinal disorders, including cancer, represent a major international health problem. Conventional gastrointestinal endoscopic diagnosis is predicated on the gross morphological characteristics of mucosal and submucosal abnormalities [146]. However, endoscopic diagnosis is less successful in clinical situations where the underlying morphological or biochemical premalignant changes do not alter gross architecture. Due to its high resolution and in-depth imaging capability, OCT has potential in the future routine clinical application in gastrointestinal endoscopy [147]. The depth range of OCT imaging, however limited, is sufficient to penetrate the mucosal lining of endoscopically accessible organs of the gastrointestinal tract to provide in-depth images with a resolution superior to currently available clinical imaging techniques [21–24].

OCT images of the normal esophagus, Fig. 16.10a, and esophago-gastric junction, Fig. 16.10b, allow the visualization of morphology of the mucosa and submucosa, and distinguish the transitional features from esophagus to stomach. From Fig. 16.10a, the upper portion of the mucosa, including stratified squamous epithelial (SE) and lamina propria (LP), appears homogeneous in the OCT image.

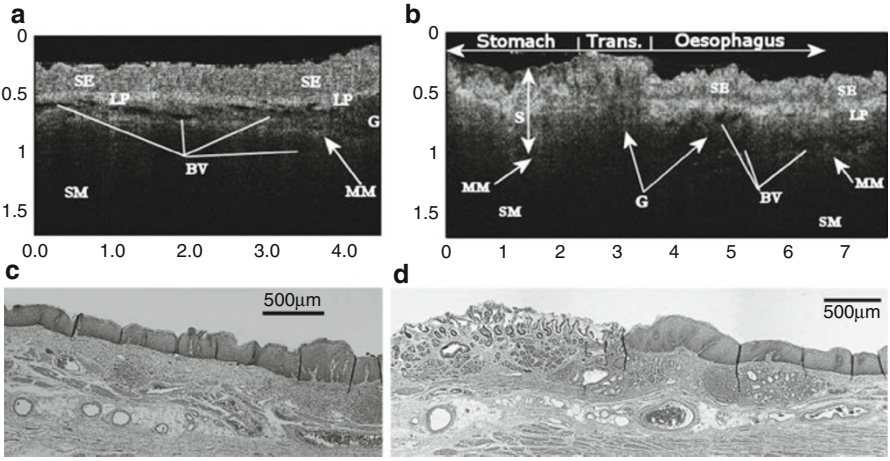

Fig. 16.10 High-resolution OCT images of normal (**a**) esophagus and (**b**) esophago-gastric junction, where *S* denotes the secretory glands, *SE* the stratified squamous epithelium, *LP* the lamina propria, *MM* the muscularis mucosae, *ED* the excretory ducts, *BV* the blood vessels, and *SM* the submucosa; and their corresponding histology (**c**) and (**d**), respectively (Courtesy of Cranfield Biophotonics Group)

The muscularis mucosa (MM) is more highly reflective than the mucosa. Numerous blood vessels can be identified in the lamina propria zone.

The transition from the esophageal to the gastric tissues was clearly visualized by the OCT images as shown in Fig. 16.10b. It demonstrated that the mucosa of the tract undergoes an abrupt transition from a protective stratified squamous epithelium (SE) to a tightly packed glandular secretory mucosa (S). The lamina propria (LP) appears highly reflecting and homogeneous in the esophagus. The muscularis mucosae (MM) is continuous across the junction, though it is less easily seen in the stomach, where it lies immediately beneath the base of the gastric glands. Other architectural features such as the excretory ducts, blood vessels, and esophageal glands were also clearly delineated in the OCT images.

The OCT images of normal colonic tissue allow visualization of the morphology of the mucosa (M), submucosa (SM), and muscle layers (ML). This is presented in Fig. 16.11a. A distinct feature of mucosa for the large intestine is its unbranched simple tubular glands (crypts of Lieberkuhn), which extend through the lamina propria to the muscularis mucosae (MM). Such a feature is clearly delineated in the OCT images, where they lie immediately above the muscularis mucosae, while the latter is seen as a high reflecting layer (see upper portion of Fig. 16.11a). The muscle layer of the colon is seen as a dark layer because the muscle highly attenuates the incoming light. The regular horizontal lining seen in the muscle layer (see bottom of Fig. 16.11a) probably demonstrates the fiber-bundle arrangement of muscularis externa.

The eventual target for endoscopic OCT includes real-time, in situ characterization of gastrointestinal premalignant changes such as dysplasia, as well as the identification

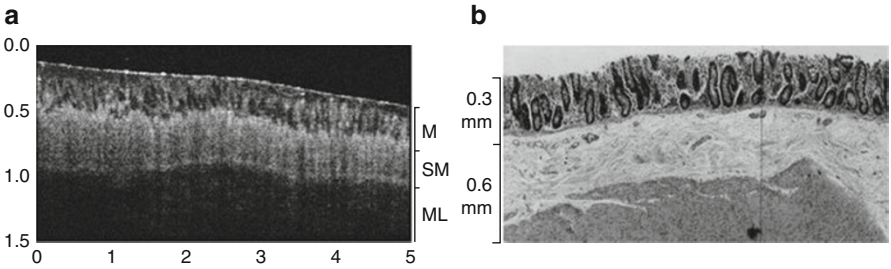

Fig. 16.11 High-resolution OCT image of (**a**) normal human colon and (**b**) its corresponding histology, where the mucosa (*M*), submucosa (*SM*), muscularis propria layer (*ML*), lymph nodule, and cryptscan be visualized (Courtesy of Cranfield Biophotonics Group)

and staging of small, superficial cancers. Endoscopic implementations of OCT in vivo have been recently reported with some success [148, 149]. As OCT technology matures, however, accurate primary diagnosis and staging by OCT could have a significant impact on clinical care because small, early stage malignancies would be amendable to immediate curative therapy at the time of endoscopy. This capability would enable physicians to make diagnostic and therapeutic decisions at the time of examination without referring to the histopathological diagnosis that normally requires a time frame of 1 week.

16.3.6 Other Biomedical Applications

The distinct features of optical coherence tomography, e.g., high resolution, relative high penetration depth, and a potential for functional imaging, make OCT a suitable candidate for optical biopsy. It offers a wide range of promising applications across all biomedical imaging disciplines. Apart from the applications stated above, we mention below briefly a few other examples of high-resolution and functional OCT.

Due to optic-fiber implementation of system, OCT is predestinated as an endoscopic modality for high-resolution intraluminal imaging of organ systems, including intravascular walls. Preliminary studies have shown that OCT can detect intramural collections of lipid within the intimal vessel wall [123, 150]. Compared with high-frequency (30 MHz) ultrasound, OCT (1,300 nm wavelength) yielded superior structural information [151, 152].

Colston et al. presented a fiber-optics-based dental OCT system operating at a central wavelength at 1,300 nm [153]. Penetration depth varied from 3 mm in hard tissues to 1.5 mm in soft tissues. Hard tissue structures identified were enamel, dentin, and dento-enamel junction (see Fig. 16.12, for example). In the early investigations, birefringence induced artifacts in the enamel OCT imaging [153, 154]. These can be eliminated by measuring the polarization state of the returned light using a polarization-sensitive OCT (PSOCT). Birefringence detected by PSOCT, however, has been shown to be useful as a contrast mechanism indicating pre-carious or carious lesions in both enamel and dentin [155, 156].

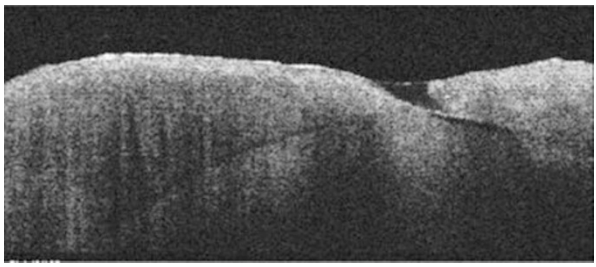

Fig. 16.12 OCT imaging of human tooth near the gingiva (*left*). Image size is 1.8 × 4 mm (Courtesy of Cranfield Biophotonics Group)

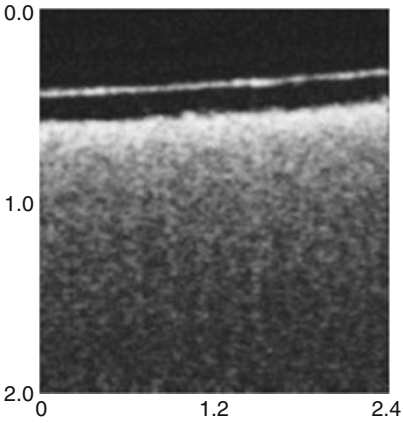

Fig. 16.13 OCT image of ceramics of a dish plate. The *top* is the glaze layer

16.3.7 Industrial Applications

As stated previously, low-coherence interferometry has already been used in optical production technology and metrology [32–34]. With the current OCT technique, Dunker et al. [157] analyzed the applicability of OCT for nondestructive evaluation of highly scattering polymer-matrix composites to estimate residual porosity, fiber architecture, and structure integrity. OCT has also found its application to detect the subsurface extent of the Hertzian crack on the surface of a silicon nitride ball that has good agreement when compared with the predictions from crack propagation theories based on principal stresses and on maximum strain energy release [158]. Nondestructive evaluation of paints and coatings is another promising non-medical OCT application [159]. Operating in a confocal mode, OCT imaging though an 80-μm-thick highly scattering polymeric two-component paint layer (corresponding to an equivalent thickness of ten mean free paths) has been demonstrated by a light source with central wavelength at 800 nm and bandwidth of 20 nm [159].

Figure 16.13 gives an example of OCT light penetration depth through a hard industrial material of a ceramic dish plate where the light source used is 820 nm central wavelength and 25 nm spectral bandwidth [160]. Despite the high scattering nature of ceramic materials, the imaging depth beyond 2.5 mm is possible.

16.4 Effects of Light Scattering on OCT

16.4.1 Introduction

Thus far, OCT has been seen to have the capability to delineate noninvasively subsurface microstructures, which has the potential to improve the diagnostic limits of currently available imaging techniques, allowing a wide range of clinical disorders to be addressed at an early stage. However, the reality is that OCT relies on the penetration and back-scattering of light into tissue to construct cross-sectional, tomographic images. It collects the back-scattered photons that have experienced less scattering, i.e., ballistic or least-scattered photons. However, unlike the transparent ocular organs where OCT found its most successful applications [18], there is no evidence that an OCT imaging depth beyond 2 mm for opaque biological tissues is possible [126]. This is largely due to the multiple scattering inherent in the interactions between the probing light and the targeted tissue, which limits light penetration into the tissue, and therefore prevents the deep microstructures from imaging. Generally, multiple scattering could degrade signal attenuation and localization, leading to an image artifact that reduces the imaging depth, degrades the signal localization and affects the image contrast.

Smithies et al. [161] developed a Monte Carlo (MC) model according to their specific OCT system geometry to investigate how signal attenuation and localization are influenced by multiple scattering effects, where two specific media (Intralipid and blood) are considered, representing moderately and highly anisotropic scattering, respectively. The multiple scattering effects were clearly demonstrated in terms of the spreading of the point spread function (PSF). In the meantime, Yao and Wang [162] developed a MC model to simulate how multiple scattering degrades the OCT signal attenuation into the tissue, by separate considerations of least scattering and multiple-scattered photons.

More recently, Wang [126] systematically investigated the multiple scattering effects on the OCT imaging performances including imaging depth, resolution degradation, and signal localization. Generally from the results, it was found that signal localization and attenuation are dependent on the optical properties of tissue. The high scattering coefficient and the low degree of forward scattering are the primary causes for the degradation of signal localization and attenuation, leading to complication of interpretation of the measured OCT signals. More importantly, it was found that the imaging resolution is a function of the probing depth within the medium, as opposed to the claimed OCT system resolution. This fact has been overlooked recently in the OCT imaging applications. The imaging resolution is greatly reduced with increasing depth; this case is even more severe for the highly scattering medium. Therefore, attention must be paid to this fact when applying the OCT to the human organs because of the high scattering nature of tissue.

Let us revisit the OCT system by looking closely the backscattering light from the high scattering medium that has the possibility to contribute to the interference signal. A simple schematic of OCT system when probing the highly scattering medium is illustrated in Fig. 16.14, where the sample beam progressively loses its

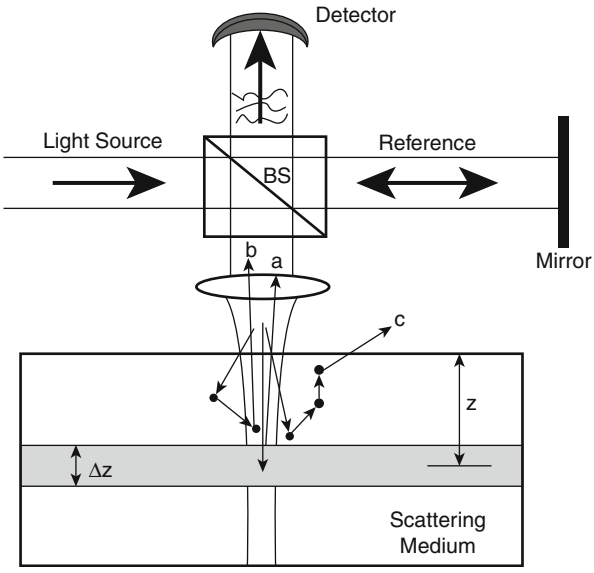

Fig. 16.14 Simple schematic of OCT system showing scattering interactions between a probing beam and biological tissue. Three types of interactions are backscattered from within the tissue: single scatter *a*, small-angle scatter *b*, and wide-angle scatter *c*. A layer with a thickness Δz at the depth of z is the expected layer for OCT localization

spatial coherence as it penetrates a turbid biological tissue. This loss of coherence results from the scattering by a variety of cellular structures with sizes ranging from less than one wavelength (e.g., cellular organelles) to several hundreds of micrometers (e.g., the length of a collagen fiber). As illustrated in Fig. 16.14, the dominant scattering interaction of the probing beam in the turbid medium can be categorized into three types [126, 163]: (1) single backscatter *a*, (2) small angle forward scatter *b*, and (3) extinction by absorption or wide angle scatter *c* (i.e., light scattered out of the view of the interferometric receiver). The detector will only receive the first two categories of scatters because of the heterodyne detection characteristics of the OCT system. Furthermore, the low-coherence light source used, as stated in the Sect. 16.2, provides a time gate to enable the detector to only receive those photons that travel beneath the tissue surface, with their optical path lengths matched to the optical path length in reference arm to within coherence length of the light source. Consequently, the OCT system in reality plays a role to sieve all the backscattering photons emerging at the detector according to their arrival times, or equivalently the optical path lengths that photons have traveled. For simplicity, we only consider the optical path length of the photon traveling beneath the tissue surface, i.e., the tissue surface is assumed to correspond with the zero position of reference mirror. Therefore, to enable the detector to produce the signal, the following criteria must be fulfilled:

$$|L_p - 2nz|, < \frac{L_c}{2}, \tag{16.17}$$

where L_p is the optical path length that the photon has traveled within the tissue, n is the refractive index of the medium, and z is the depth of a layer whose distance from the tissue surface matches the scanning distance of mirror, nz, in the reference arm.

For the signal localization, we normally expect that the detected photons be backscattered from the layer whose thickness is determined by

$$2n\Delta z = L_c. \tag{16.18}$$

However, because of multiple scattering there are possibilities for those photons contributing to the detected signal that are not backscattered from the expected layer, z, but fulfill the criteria of (16.17). As a consequence, this part of the photons degrades the signal attenuation, localization, and resolution because they are not from the desired layer, leading to a signal artifact complicating the interpretation of OCT image. To gain insight into how single and multiple scattering effects would influence the signal attenuation and localization, it is therefore useful to classify the photons according to their localization information. We could classify the detected photons into those photons being backscattered from the desired layer, z, and those backscattered otherwise but fulfilling the criterion of (16.17). Due to the requirement of matching the optical path lengths, the photons in the former must undergo fewer scattering events and very small-angle scattering including the single backscattering events, we therefore term this part of photons as the least scattered photons (LSP). Those photons that satisfy (16.17) but are backscattered from a depth other than the desired layer are treated as the multiple scattered photons (MSP) that have experienced a wider-angle scattering. Clearly, the LSP signal is particularly useful as it provides localized optical information about the targeted layer; whereas the MSP signal consists of multiply scattered photons that are not from the desired layer, leading to the degradation of detected signal.

There is a clear relationship between the scattering interaction types described earlier in this section and the photon classifications that will be used in this study. The MSP comes solely from the interaction type b, while the LSP includes the interaction type a and part of type b because the photons backscattered from the desired layer might be subject to multiple scattering but with very small-angle scattering. A distinct difference between them is that the LSP and MSP have been sorted according to their optical pathlengths, thereby enabling the investigation of their influence on the OCT signal attenuation and localization.

With these conventions in mind, we now turn to look at some ways that multiple scattering affects OCT imaging performance by the use of the Monte Carlo simulation technique. For details, please see reference [126].

16.4.2 The Effects of LSP and MSP on Attenuation

To investigate the influence of the photons coming back from the specific layer of interest, it is best to investigate separately the LSP and MSP signals on the backscattering profiles. Figure 16.15 illustrates such results for $\mu_s = 40\ \text{mm}^{-1}$

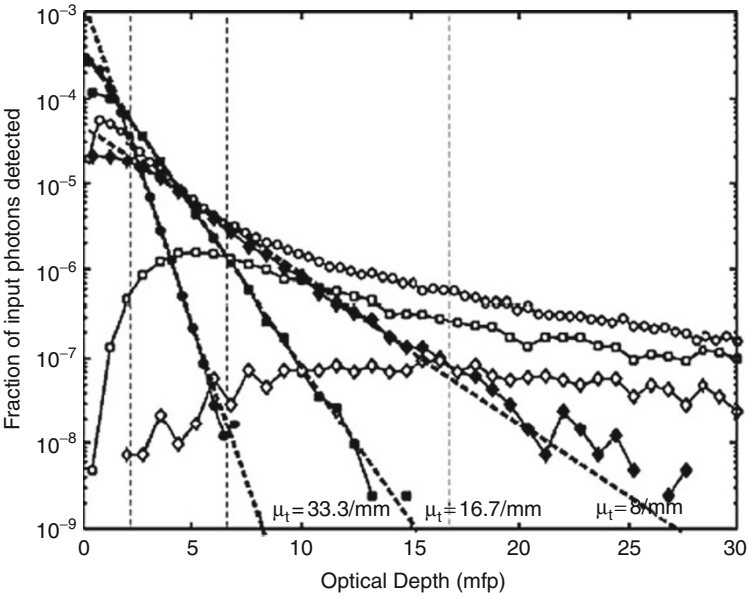

Fig. 16.15 The profiles are shown as the backscattering intensities separately for the LSP and MSP photons for the media with optical properties of $g = 0.7$ (*circle*), 0.9 (*square*), and 0.98 (*diamond*), respectively, while $\mu_s = 40\ \text{mm}^{-1}$ is kept the same for all the media. The *curves with solid symbols* represent the LSP photons, and those *with hollow symbols* the MSP photons. The *vertical dashed lines* from left to right indicate the critical imaging depth for $g = 0.7$, 0.9, and 0.98, respectively. *Thick dashed lines* represent the least square fits of the LSP signals

with $g = 0.7$, 0.9, and 0.98, respectively. It can be seen that the strength of the MSP signal increases with decreasing g in the medium at any optical depth of light penetration. This indicates that the photons that have reached a depth that does not correspond to the desired layer have a greater chance of emerging at the detector for the less anisotropic medium, leading to a greater degree of uncertainty in signal localization. The signal from LSP has an approximately logarithmic linear relationship with the probing depth for all cases but with different slopes. The slopes for the media investigated are calculated as 33.3, 16.7, and 8.0 mm^{-1} for $g = 0.7$, 0.9, and 0.98, respectively. These values deviate significantly from the theoretical value of 40 mm^{-1}, with the worst case for the highest g. This is probably understandable because the higher the value of g, the greater the degree of forward scattering of photons in the medium, leading to a greater chance of the photons reaching the detector while satisfying the criterion of (16.17). Obviously such photons are able to survive more scattering events because of small-angle scattering.

Because the OCT signal is the summation of the MSP and LSP, it appears that the critical depth for optical imaging is the depth where the signal from the LSP equals that from the MSP as the imaging contrast beyond this depth will be less than 1. These depths are illustrated in Fig. 16.15 as vertical dashed lines from left to right

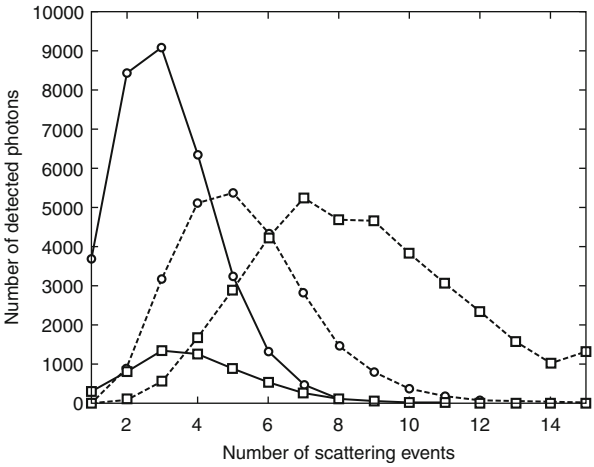

Fig. 16.16 Photons detected plotted as a function of the number of scattering events, backscattered from the specific depths at 50 μm (*circle*) and 100 μm (*square*), respectively. *Solid curves* are from LSP signals, while *dashed curves* are from MSP signals. Note that the number of detected photons backscattered from 100 μm is artificially magnified by five times to facilitate the comparisons

for $g = 0.7$, 0.9, and 0.98, respectively, corresponding to 2 MFP, 6.65 MFP, and 17 MFP, where MFP represents mean free path length measured as optical depth of $\mu_s d$. It should be noted that the critical depth, at which the MSP signal levels with the LSP signal, should actually be greater because the simulations do not take into account the polarization effects. The MSP photons undergo more scattering events than the LSP photons; the average scattering events increase much faster for the MSP photons with increasing depth. This is illustrated in Fig. 16.16, where the detected photons are plotted as a function of the number of scattering events for the LSP and MSP signals backscattered from the depths of 50 and 100 μm, respectively. The optical parameters used for Fig. 16.16 are $\mu_s = 67\ \text{mm}^{-1}$ and $g = 0.7$. Please note that the number of detected photons for the case of 100 μm has been artificially magnified by five times to facilitate the comparisons. All the curves are skewed towards the lesser number of scattering events. The average number of scatterings from the LSP signal has only a slight increase from the depth of 50–100 μm, that is, from 2.5 to 2.8 scattering events, respectively, while for the MSP signal, the average scattering increases much faster from 50 to 100 μm, that is, from 4.6 to 7.4 times. As multiple scattering depolarizes the light, the MSP photons are progressively and rapidly randomized with the increase in probing depth. As a consequence, the actual signal from MSP should be much lower than the calculated signals.

Despite the greater degree of degradation of signal attenuation, the probing critical depth increases dramatically with the increase of the anisotropic factor of the medium as illustrated in Fig. 16.15. This is particularly useful in the optical clearing of blood by the use of biocompatible dextrans, where the dextrans induce blood cell aggregation, an effect that might increase the forward direct scattering of the blood solution, leading to an enhanced optical imaging depth for OCT imaging through the blood [117, 124].

16.4.3 Signal Localization

As a photon penetrates the turbid biological tissue, it progressively loses its spatial coherence due to the tendency of having a greater chance of being scattered by the tissue. In the meantime, the photons multiply backscatter from within the tissue at a greater depth, and those that are merged at the detector will have a greater chance of fulfilling the criterion of (16.17) for the photon categories of either MSP or LSP. It is the MSP that degrades signal localization because it is from a depth other than the expected layer, leading to reduced axial resolution of the OCT image. Signal localization was thus investigated systematically by means of the point-spread function (PSF) at the specific depth, for different optical properties to illustrate how the LSP and MSP contribute to signal localization.

Figure 16.17 gives examples of depth point spread function (zPSF) at different probing depths for the turbid media representing moderate scattering in the left column ($\mu_s = 10\ \text{mm}^{-1}$) and high scattering in the right ($\mu_s = 67\ \text{mm}^{-1}$). The figures were obtained for $g = 0.7$, 0.9, and 0.98 from top to bottom, respectively, to allow us to scrutinize the influence of the anisotropic parameter of the medium on the signal localization. The depths monitored are indicated in each figure. The filled symbol curves are the actual PSFs that are the summation of LSP and MSP signals from a specific depth. However, to investigate the effects of LSP and MSP signals separately on the PSFs, the signals from the LSP alone are plotted in each case, represented by the hollow symbol curves.

First, it is obvious that the worst case is from the medium with the highest scattering coefficient and lowest degree of forward scattering, i.e., $\mu_s = 67\ \text{mm}^{-1}$ and $g = 0.7$ in this case (see the top right figure), where signal localization is merely discerned at a depth of 50 μm. Even at this depth, the contribution from an MSP signal is large enough to degrade the signal localization, where it can be seen that the PSF curve is skewed towards the nominal probing depth, indicating that the photons multiply scattered within the medium before this depth have more chances of surviving to reach the detector. Moreover, the photons backscattered from a very shallow depth at approximately 5 μm still survive the scattering to meet the criterion of equation (16.17) for depth localization at 50 μm. With an increase in probing depth to 150 μm, the PSF is overwhelmed by the MSP signal with only a few photons belonging to the LSP category. At this depth the signal localization is totally lost for OCT imaging. Furthermore, the axial resolution and imaging contrast are greatly reduced. The claim of high-resolution optical imaging of OCT is therefore questionable for highly scattering biological tissues. The axial resolution of OCT imaging is dependent on the optical properties of tissue and is a function of depth.

Figure 16.18 illustrates the measured axial resolution from the simulation results as a function of depth for the cases of $(\mu_s, g) = (67\ \text{mm}^{-1}, 0.7)$, $(67\ \text{mm}^{-1}, 0.9)$, and $(10\ \text{mm}^{-1}, 0.9)$, respectively. The axial resolution of the OCT system is merely kept up to the depth of 50 μm for the case of $(\mu_s, g) = (67\ \text{mm}^{-1}, 0.7)$. After this depth, the actual axial resolution degrades exponentially with the increase of depth, where it becomes approximately 220 μm at the depth of 200 μm as opposed to the system

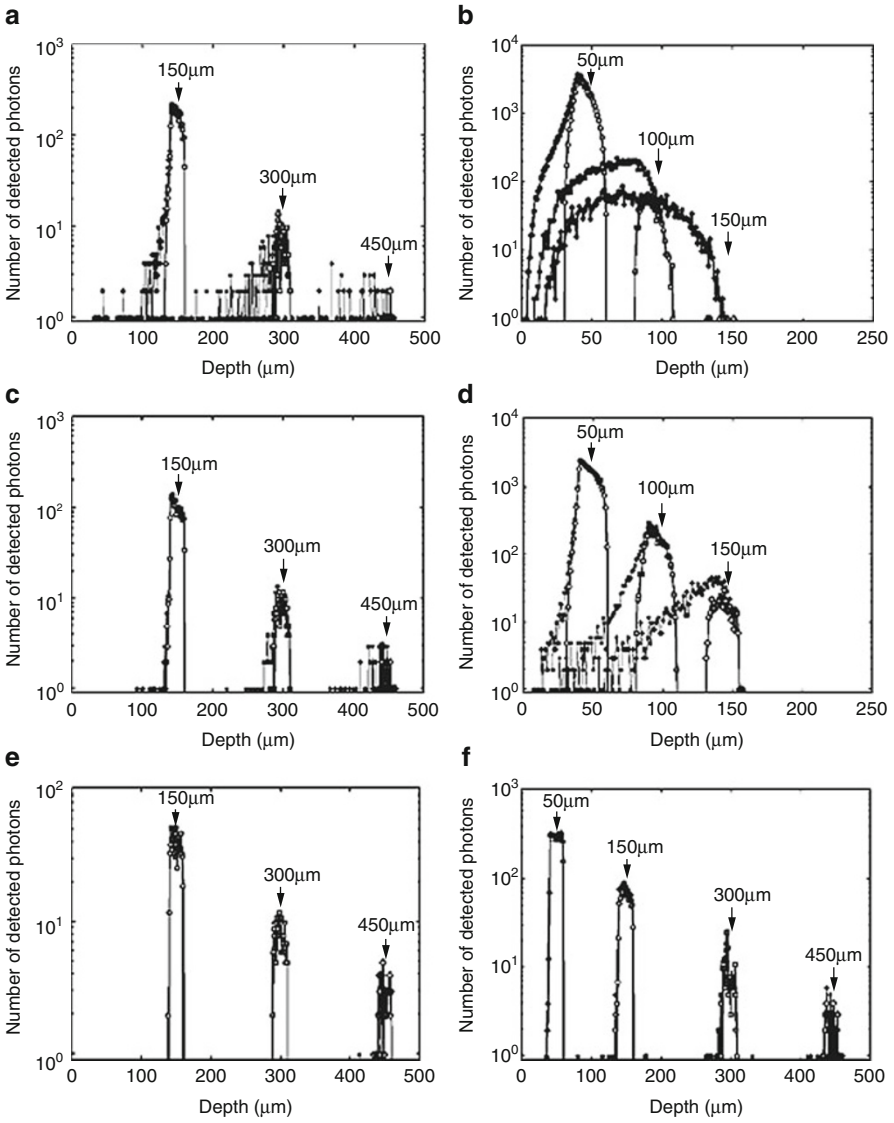

Fig. 16.17 Depth point spread functions (*solid symbol curves*) at different probing depths as indicated, for the turbid media representing moderate scattering ($\mu_s = 10\ \text{mm}^{-1}$) in the *left column* and high scattering ($\mu_s = 67\ \text{mm}^{-1}$) in the *right*. From *top* to *bottom*, $g = 0.7$, 0.9, and 0.98, respectively. The LSP photons are plotted as the curves with *hollow symbols*

resolution of 40 μm. With the increase of g to 0.9, this performance has been improved, with system resolution retained up to a depth of 100 μm. If, in the meantime, the scattering coefficient of the medium is reduced, for example, to $\mu_s = 10\ \text{mm}^{-1}$ in this case, the probing depth at which imaging resolution is

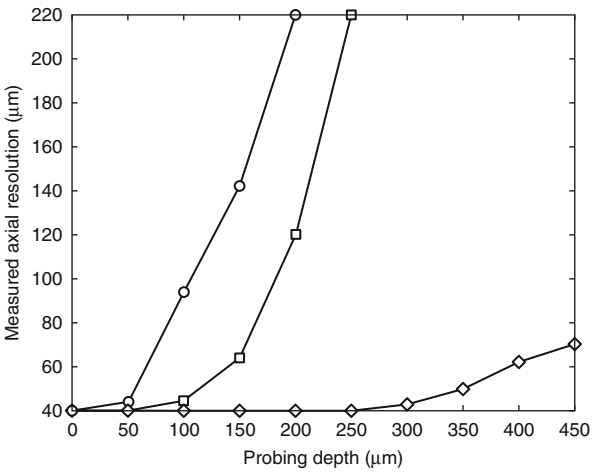

Fig. 16.18 The measured axial resolution from the simulation results plotted as a function of the probing depth for (μ_s, g) = (67 mm^{-1}, 0.7) (*circle*), (67 mm^{-1}, 0.9) (*square*), and (10 mm^{-1}, 0.9) (*diamond*), respectively

retained to the theoretical value would dramatically improve. This result is particularly welcome for the optical clearing of tissues with the purpose of enhancing the imaging depth of OCT, which will be discussed in the next section.

With the reduction of the scattering coefficient (compare the left and right columns in Fig. 16.17), signal localization improves, with the lesser MSP signal contributing to the depth of PSFs. This indicates that the low scattering medium offers the more localized signal at any probing depth, which alternatively implies that the light penetration depth, i.e., optical imaging depth, is enhanced with less deterioration of the imaging resolution as stated above. On the other hand, it can be clearly seen from Fig. 16.17 that, with increasing g, the signal localization at any depth for the scattering medium improves dramatically, where the highly forward scattering medium, i.e., $g = 0.98$, offers the best signal localization for all the cases investigated; see the bottom two figures for μ_s = 10 mm^{-1}and μ_s = 67 mm^{-1}, respectively. In these cases, only a few photons from the MSP category survive the scattering to contribute to final PSF at a depth of up to 600 μm.

However, the results shown in Fig. 16.17 do not give us the information as to how many times a photon has been scattered within the medium for both the LSP and the MSP signal before reaching the detector. Figure 16.19 gives such information of the average scattering event of the photons within the medium as a function of the probing depth for the media with (μ_s, g) = (10 mm^{-1}, 0.7 or 0.9) and (67 mm^{-1}, 0.7 or 0.9), respectively. It is clear that the higher the scattering coefficient, the greater the number of scattering events of the photons at any depth before emerging at the detector in both LSP and MSP. For both the LSP and MSP photons, the average number of scattering events has an approximate linear relationship, with the probing depth for all the cases investigated; but this relationship is stronger for the MSP.

For the high scattering medium, $\mu_s = 67$ mm^{-1}, the average number of scattering events for MSP is close to 15 times at a depth of about 120 μm. Please note that,

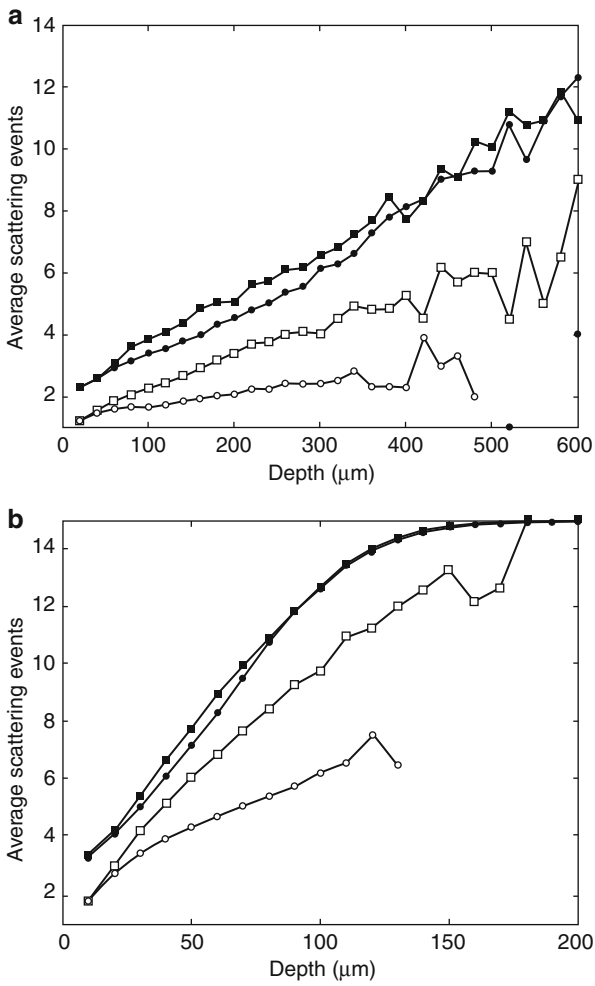

Fig. 16.19 The average number of scattering events for the LSP (*hollow symbols*) and MSP (*solid symbols*), plotted as a function of probing depth for (**a**) $\mu_s = 10\ \text{mm}^{-1}$ with $g = 0.7$ (*circle*) or 0.9 (*square*), and (**b**) $\mu_s = 67\ \text{mm}^{-1}$ with $g = 0.7$ (*circle*) or 0.9 (*square*), respectively

after this depth, the curve looks like running into a flat region for MSP; this is an artifact due to the fact that the maximum scattering number of photons monitored in our MC program is set to 15 times in order to save the memory for computing. In the meantime, with the increase in g, the average number of scattering events increases with increasing probing depth for both the LSP and MSP; however, the pace for LSP is faster than that for MSP. For example, at a depth of 300 μm for $\mu_s = 10\ \text{mm}^{-1}$ medium, the average number of scattering events for the LSP signal increases from 2.4 to 4.2, while for the MSP signal it only increases from 6.1 to 6.5. Bear in mind that the LSP photons have survived the criterion of equation (16.17), which alternatively means that they undergo a much smaller angle scattering than MSP photons.

Generally speaking, the average number of scattering events is much greater for MSP photons than for LSP photons. This is good in that the multiply scattered

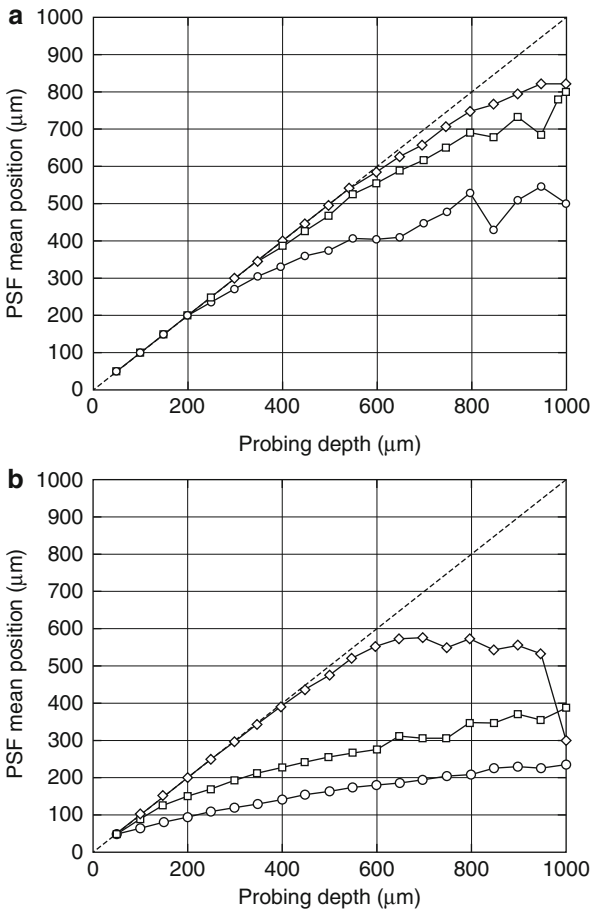

Fig. 16.20 Measured PSF mean positions plotted against the probing depths for the media with $g = 0.7$ (*circles*), 0.9 (*squares*), and 0.98 (*diamonds*) and (**a**) $\mu_s = 10\ \text{mm}^{-1}$ and (**b**) $\mu_s = 67\ \text{mm}^{-1}$, respectively. The *dashed lines* represent the nominal depth positions for PSFs

photons lose their polarization state progressively with an increase in scattering events, and thus actually contribute less to the final signal measured. The increased number of scattering events for increasing g accounts for the fewer slopes for LSP signals observed in Fig. 16.15, and is the primary cause of the degradation of signal attenuation. To investigate how signal localization depends on the optical properties, for example, μ_s and g, Fig. 16.20 gives such information for the determined PSF mean position from the simulations as a function of the probing depth for the media with $g = 0.7$, 0.9, and 0.98 and (a) $\mu_s = 10\ \text{mm}^{-1}$ and (b) $\mu_s = 67\ \text{mm}^{-1}$, respectively. The broken lines in the figure represent the nominal depth positions for PSFs. It can be seen that for a less scattering medium with high g value, for example, $\mu_s = 10\ \text{mm}^{-1}$ and $g = 0.98$ in Fig. 16.20a, the best accuracy of signal localization throughout the depth monitored is given; the opposite is true for the highest scattering medium and lowest g investigated. For $\mu_s = 67\ \text{mm}^{-1}$ and $g = 0.7$, the accuracy of signal localization is only reliable up to a depth of 50 μm.

With increasing probing depth the ability of OCT to provide signal localization is greatly reduced. This is because the MSP photons progressively overwhelm the LSP photons with increasing depth. This effect makes OCT lose its localization capability, while the increase of g value dramatically improves signal localization, where it can be seen that for $\mu_s = 67\ \text{mm}^{-1}$ and $g = 0.98$ the signal localization is maintained up to about 600 μm. After this depth the accuracy starts to level off. Generally, the accuracy of signal localization is improved by either the reduction of the scattering coefficient or the increase of the degree of forward scattering of the medium.

Thus, overall, it can be concluded that the signal localization or imaging depth can be improved by either reduction of the scattering coefficient or increasing the anisotropic value of the medium, or both. It can also be seen that the manipulation of g towards a high value is more efficient than that of the scattering coefficient. This conclusion is particularly useful for the optical clearing of tissues by the use of biocompatible chemical agents for the purpose of enhancing the optical imaging depth for high-resolution optical imaging techniques. A recent study indicated that the mechanisms for improving the light penetration depth for the dextran-mediated blood is due to both the refractive matching and red blood cell (RBC) aggregation and disaggregation induced by the dextrans [78, 117]. The index-matching effect causes the reduction of the scattering coefficient of the medium, while RBC aggregation probably increases the anisotropic factor for the blood, leading to increased light penetration depth.

The above analysis has used the Monte Carlo simulation technique as a tool to illustrate the multiple scattering effects on the OCT imaging performance. It is worth noting that there are analytical models developed for analyzing the multiple scattering effects as well. Schmitt and Knüttel described an OCT model by the use of a mutual coherence function based on the extended Huygens–Fresnel principles of light propagation in homogeneous turbid media [165]. It was later extended by Thrane et al. by incorporating the so-called "shower curtain effect" (see also ▶ Chap. 17). This model considers the OCT signal as the summation of singly back-scattered light (coherent) and multiply scattered light (partially coherent) [166]. Most recently, Feng et al. further simplified Thrane's model through approximating the focusing optics in the sampling arm by an imaginary lens proximal to the tissue surface [167]. The advantage of the latter model is that it avoids the consideration of backscattering light from traveling in the free space between the focusing lens and tissue surface before mixing with the reference beam, i.e., observing the object embedded in scattering medium at the mixing plane through a non-scattering distance. The detailed description of the analytical models for OCT will be covered in ▶ Chap. 17.

16.5 New Technique to Enhance OCT Imaging Capabilities

16.5.1 Introduction

From the last section, we have seen that multiple scattering is a detrimental factor that limits OCT imaging performances, for example, imaging resolution, depth, and localization. To improve the imaging capabilities, the multiple

scattering of tissue must be reduced. Tissue as a scattering medium shows all optical effects that are characteristic of a turbid physical system. It is well known that turbidity of a dispersive physical system can be effectively controlled using immersion effect matching of refractive indices of the scatters and the ground material [168–171]. The living tissue allows one to control its optical (scattering) properties using various physical and chemical actions such as compression, stretching, dehydration, coagulation, UV irradiation, exposure to low temperature, and impregnation by chemical solutions, gels, and oils [171–182]; see also ▶ Chap. 5. Such methods of controlling optical properties of tissue have been explored to enhance the optical imaging capabilities of OCT [25, 124, 183–189]. The possible mechanisms of enhancing OCT imaging depth and contrast have been suggested [124, 167, 171, 183–192].

The depth of penetration for near-infrared light into a biological tissue depends on the scattering characteristics and absorptivity of the tissue. Optically, tissue can be described as a spatial distribution of refractive index on the microscopic scale that could be classified into those of the extracellular and intracellular components [192, 194]. Estimated from the dissolved fractions of proteins and carbohydrates, the intracellular and extracellular fluids have the approximate refractive index between 1.34 and 1.36 [195]. The results of earlier studies suggest that the tissue elements that contribute most to the local refractive index variations are the connective tissue fibers (bundles of elastin and collagen), cytoplasmic organelles (e.g., mitochondria), and cell nuclei [195, 196]. The refractive index of the connective fiber is about 1.47, which corresponds to 55 % hydration of collagen [197]. The nucleus and cytoplasmic organelles in mammalian cells that contain similar concentrations of proteins and nucleic acids, such as mitochondria and ribosome, have refractive indices that span within a relatively narrow range between 1.39 and 1.42 [198, 199]. However, other cytoplasmic inclusions, particularly pigment granules, can have much higher refractive indices [195]. Therefore, the local refractive index within the tissue can vary from anywhere within the background refractive index, i.e., 1.34, and 1.50, depending on what type of soft tissue is concerned. It is this variation of refractive index distribution within the tissue that causes a strong light scattering. Unfortunately, as stated in the last section, the light scattering limits light penetration depth and degrades the imaging contrast [126]. For non-interacting Mie scatterers, the reduced scattering coefficient of spheres is determined by the ratio of refractive indices of scattering center and ground matter [200, 201]. If the mismatch between scattering centers and the ground substance decreases, it would result in less scattering at the interface between the ground substance and cellular components, leading to the decrease of reduced scattering coefficient of tissue [167, 171, 187].

To describe theoretically the optical scattering in tissues, attempts have been made using the particle model with some success [192, 194]. Based on the model, the biological tissue is treated as that consisting of the discrete scattering centers with different sizes, randomly distributed in the background media. According to the Rayleigh-Gans approximation, the reduced scattering, μ_s', of turbid media is

related to the reduced cross section, σ'_s, and the total number of scattering particles per unit volume, i.e., number density, ρ:

$$\mu'_S = \sum_{i=1}^{n} \rho_i \sigma'_{Si} = \sum_{i=1}^{n} \frac{3\varphi_i}{4\pi a_i^3} \sigma'_{Si}, \tag{16.19}$$

and

$$\sigma'_{Si} = \frac{9}{256\pi} \left| \frac{m_i^2 - 1}{m_i^2 + 2} \right| \left(\frac{\lambda}{n_0} \right)^2 \int_0^{\pi} (\sin u_i - u_i \cos u_i)^2 \frac{(1 + \cos^2\theta) \sin\theta (1 - \cos\theta)}{\sin^6(\theta/2)} \, d\theta \tag{16.20}$$

where $u_i = 2(2\pi a_i n_0/\lambda) \sin(\theta/2)$, $m_i = n_{Si}/n_0$ with n_{Si} and n_0 being the refractive indices of the i-th scattering centers and background medium, φ_i the volume fraction of the i-th particles and a_i the radius of the i-th scatterer. It can be seen that the reduced scattering coefficient of scattering medium is dependent on both the refractive index ratio, m_i, and the size of the scattering centers.

The most popular method in enhancing OCT imaging performances is to use the biochemical and hyperosmotic chemical agents to interrogate the tissue. Below we give some examples to intuitively illustrate to what degree the multiple scattering can be reduced and how the imaging depth and contrast of OCT imaging can be improved by the use of impregnation of tissue with the biochemical agents. The agents used in these examples are glycerol and dimethyl sulfoxide (DMSO).

16.5.2 Enhancement of Light Transmittance

The light transmittance and scattering after the application of chemical agents can be assessed quantitatively by the use of the near-infrared spectroscopic method. With the use of Varian Cary 500 spectrophotometer with an internal integrating sphere (Varian UK Ltd), Fig. 16.21a, b illustrates the shift of transmittance and diffuse reflectance spectra, respectively, over the range of 800–2,200 nm as a function of time when the native porcine stomach pyloric mucosa specimen was applied with 80 % glycerol. The curves shown in the figure were obtained at the time intervals of 0, 5, 10, 20, and 30 min, respectively, from bottom to top for transmittance (Fig. 16.21a) and from top to bottom for reflectance (Fig. 16.21b). It can be seen from Fig. 16.21 that, over the whole wavelength range investigated, the transmittance was increased with time. Diffuse reflectance was decreased over the range of 800–1,370 nm. The greatest increase in transmittance was at 1,278 nm, and the greatest decrease in reflectance was at 1,066 nm.

Figure 16.22a, b show the similar results from the samples with the application of 50 % DMSO, respectively, at the time intervals of 0, 5, 10, 20, and 30 min. Transmittance was enhanced and diffuse reflectance was reduced with the time course.

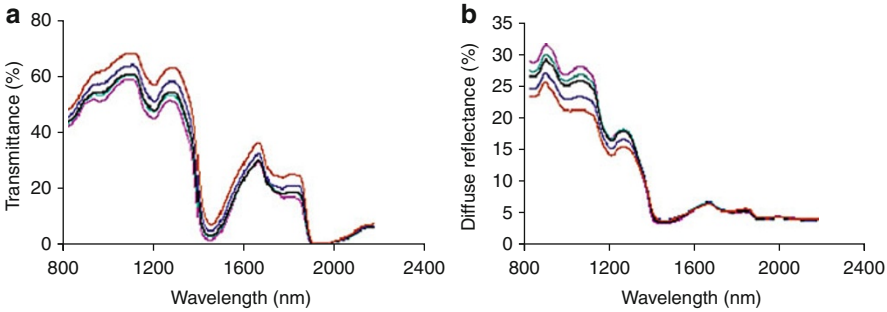

Fig. 16.21 Optical changes for porcine stomach pyloric mucosa before and after application of 80 % glycerol over the range from 800 to 2,200 nm measured by spectrophotometer. (**a**) Transmittance after application of the agent at the time intervals of 0, 5, 10, 20, and 30 min (from *bottom to top*), respectively. (**b**) Diffuse reflectance at the time intervals the same as in (**a**) (from *top to bottom*) [189]

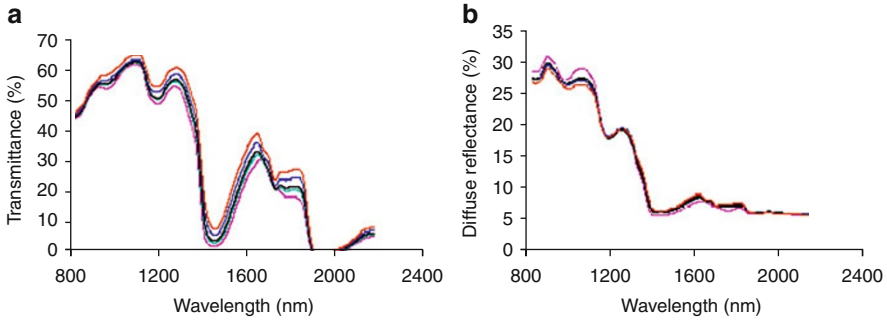

Fig. 16.22 Optical changes for porcine stomach pyloric mucosa before and after application of 50 % DMSO over the range from 800 to 2,200 nm measured by spectrophotometer. (**a**) Transmittance after application of the agent at the time intervals of 0, 5, 10, 20, and 30 min (from *bottom to top*), respectively. (**b**) Diffuse reflectance at the time intervals the same as in (**a**) (from *top to bottom*) [189]

From Figs. 16.21 and 16.22, it is clear that both glycerol and DMSO have the ability to clear the tissue, thereby enhancing the light transmittance through the tissue.

It is found that there is a strong correlation between optical clearing and water desorption [189–191]. The water activities for 80 % glycerol and 50 % DMSO measured with a water activity meter (Aqua Lab Model Series 3 TE, Labcell Ltd) yield 0.486 and 0.936, respectively. Figure 16.23 shows the water content measurements at 30 min after the treatment, where 80 % glycerol caused 15 % water loss, whereas 50 % glycerol and 50 % DMSO caused 9 % and 7 %. The patterns of optical clearing are similar to those of water desorption.

Because most of OCT system uses the light source with a central wavelength at 1,300 nm, Fig. 16.24 shows experimental results of the transmittance enhancement at about 1,300 nm after application of different chemical agent solutions, where it is

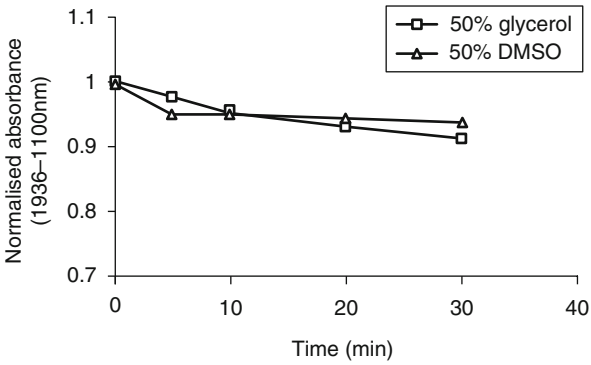

Fig. 16.23 Correlation between the NIR absorbance (measured at 1,936–1,100 nm) and time of application of 50 % glycerol and 50 % DMSO, respectively [189]

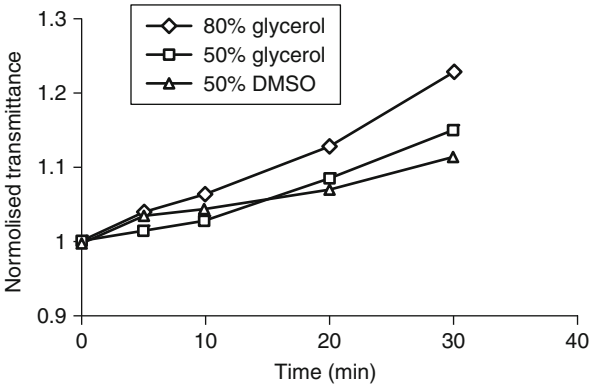

Fig. 16.24 Changes in transmittance at 1,278 nm against time for porcine stomach pyloric mucosa treated with 80 %, 50 % glycerol or 50 % DMSO [189]

seen that transmittance was increased by approximately 23 % at 30 min after the application of 80 %, while 15 % and 11 % were received after the treatment with 50 % glycerol and 50 % DMSO, respectively.

The optical clearing induced by the agents studied is a time-dependent process [188, 189, 192]. This implies that the clearing effect occurs as a consequence of the diffusion of water out of the tissue, leading to dehydration [189, 190], and the diffusion of chemical agents into the tissue [189, 192], respectively. For tissue dehydration, the water will migrate from within tissue, where there is higher water potential and a lower osmotic potential, to the outside, where there is lower water potential and higher osmotic potential, because the applied agents have the higher osmotic potential than that of tissue fluids. The migration of water will be terminated if the osmotic pressure is balanced inside and outside of the tissue if the agent is impermeable to the tissue.

However, the glycerol and DMSO are both permeable to tissue, indicating that the agents will diffuse into the tissue at the same time when the water leaves the

tissue. The mass transport of the chemical agents within tissue is a complicated phenomenon that involves the bulk tissue and its constituent cells and fiber structures. Because tissue occupies the intracellular (and/or fibrillar) and extracellular (and/or extrafibrillar) spaces, we assume that the agent will first transport into the extracellular (and/or extrafibrillar–interstitial) space, and then into the intracellular (and/or fibrillar) space, leading to an activity for water in and out of the surrounding interstitial space (and/or cells). The general rule of water migration will apply, that is, the water will transport from an area with the higher water potential and lower osmotic pressure to an area with the lower water potential and higher osmotic pressure. When the agent transports from the inserted (topically or by injection) area into surrounding space, it induces a higher osmotic potential around and thus causes the water to migrate out from the surrounding interstitial space and to leave the intrafibrillar (and/or intracellular) space, causing the fibers and/or cells to shrink. As a rule, this is a second stage of the process. In the meantime, the glycerol and DMSO are membrane permeable, suggesting that the agent will diffuse into the intracellular space after it arrives at the extracellular space. The transmembrane permeability for glycerol and DMSO is much lower than that of water (water is on the order of 10^{-2} cm/min, whereas glycerol and DMSO are on the order of 10^{-5} cm/min [202, 203]), which accounts for an initial decrease in cell volume as water leaves much faster than the agent migrates into it. Therefore, much of the intracellular water leaves the cell while the clearing agent continues to migrate into the cell, leading to a gradual increase in volume that stabilizes with the time course. Because both the anhydrous glycerol and DMSO have the refractive indices of 1.47 [204], after the agent migrates into the extracellular and intracellular space, a refractive index matching environment is created by simply matching the chemical agents with the main scattering components within the tissue, leading to the enhanced light penetration together with the dehydration effect. It should be noted that this is different from the refractive index matching created by the dehydration where the matching is produced by the more closely packed scattering constituents.

On the other hand, the mass transport process is dependent on the permeability of water and the agents to the membrane, and the tissue as a whole. Among the glycerol and DMSO, the former has lower permeability than the latter. As a consequence, DMSO penetrates the membrane and tissue rapidly [205], and even across the stratum corneum of skin [204], which glycerol is not able to do. The study on the hamster skin by Vargas et al. [186] also showed that DMSO has a greater effect in enhancing the light transmittance than that of glycerol. However, the stomach tissue in the present study has different characteristics in allowing the agents diffusing into the tissue because it does not have a barrier of the stratum corneum for the skin case. In addition, the mucosa layer of stomach is composed of loosely packed cells, and glands and ducts with narrow lumens are rich, which would facilitate the agents diffusing into the tissue. Thus, the mass transport process would happen much quicker than that of the skin, with the DMSO faster than the glycerol. As a consequence, with the progress of agent transport, a spatial gradient is created because water efflux will occur at the surface first and then deeper as the diffusion front moves [206]. The move of diffusion front for DMSO is much more

rapid than that of the glycerol, indicating that the water efflux at the surface is occurring for a much longer time with glycerol than with DMSO.

Accordingly, the changes in optical properties are observed almost linearly with time with the application of 50 % glycerol (see Figs. 16.23 and 16.24), probably because the solution diffuses into tissue at almost the same rate as the water efflux at the surface. It is also understandable that 80 % glycerol has a greater slope for both the transmittance and reflectance because it has the stronger ability in dehydration. For the samples treated with 50 % DMSO, in the first 5 min, DMSO permeates faster and replaces water faster (Figs. 16.23, 16.24), and its optical clearing effect is greater than 50 % glycerol. After 30 min treatment, dehydration caused by 50 % glycerol is slightly higher than that by 50 % DMSO. Consequently, the optical clearing effect induced by 50 % glycerol is slightly greater than that by 50 % DMSO within the time period investigated, although they both have the same refractive indices. The better effect caused by DMSO at the beginning stage results from the different mass transport process of DMSO and glycerol, as stated above.

16.5.3 Enhancement of OCT Imaging Capabilities

In the last section, we clearly see that the chemical administration of tissue would increase light transmittance through the tissue, the effect of which would no doubt increase the imaging depth for OCT. Figure 16.25 shows dynamic OCT structural images of porcine stomach with the topical application of 50 % glycerol solution, which was recorded at the time intervals of 0, 10, 20, 30, 40, and 50 min, respectively.

The OCT system used was working at wavelength of 1,300 nm with axial and transverse resolutions at 15 and 20 μm, respectively. A metal needle was inserted into the tissue approximately 1 mm beneath the surface. The signals reflecting back from the needle surface were used to suggest improvement of back reflectance signal caused by the chemical clearing. The OCT image of the porcine stomach without the administration of glycerol has a visualization depth of approximately 1.0 mm, as shown in Fig. 16.25a. It can be seen that a significant improvement of the imaging depth is clearly demonstrated after the topical application of glycerol. The penetration depth has increased to about 2.0 mm after 50 min application of glycerol, as shown in Fig. 16.25f. Tissue shrinkage occurs after the administration of the agents to tissue, see Fig. 16.25b–f. The needle embedded in the tissue becomes brighter with the increase of the time duration, see Fig. 16.25b–f. It should be pointed out that the imaging contrast of Fig. 16.25c, d is also greatly improved. Such features as lamina propria (LP) and muscularis mucusae (MM) are clearly visualized in Fig. 16.25c, d. The neck, base, and MM layers of the tissue could be differentiated after 20–30 min application of glycerol. The reflection from the needle surface is also sharp within this period of time. But it is interesting to find out that, with the increase of time, the imaging contrast improvement disappears gradually with the further increase of time course, as shown in Fig. 16.25e, f.

Figure 16.26 is the dynamic OCT structure images of porcine stomach with the topical application of 50 % DMSO solution, which was again recorded at the time

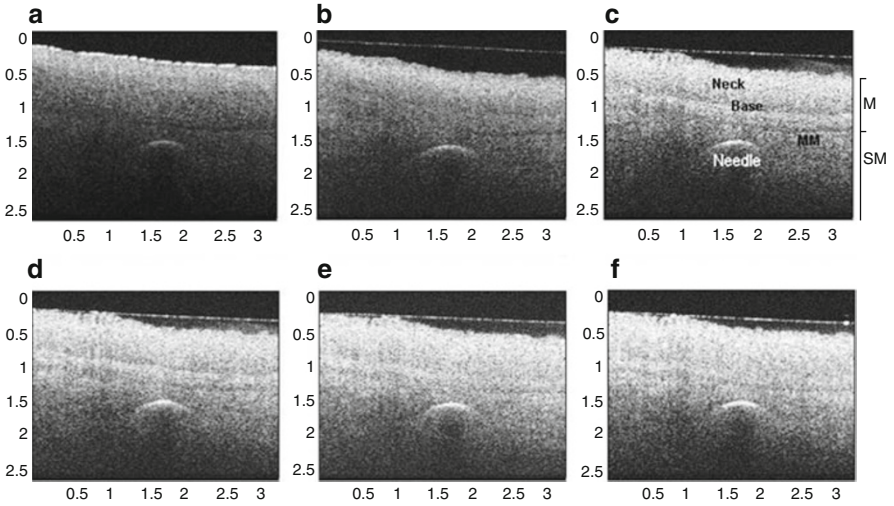

Fig. 16.25 Dynamic OCT images obtained at the time (**a**) 0, (**b**) 10, (**c**) 20, (**d**) 30, (**e**) 40, and (**f**) 50 min after the topical application of 50 % glycerol solution onto the porcine stomach tissue. All the units presented are in millimeters, and the vertical axis presents the imaging depth [188]

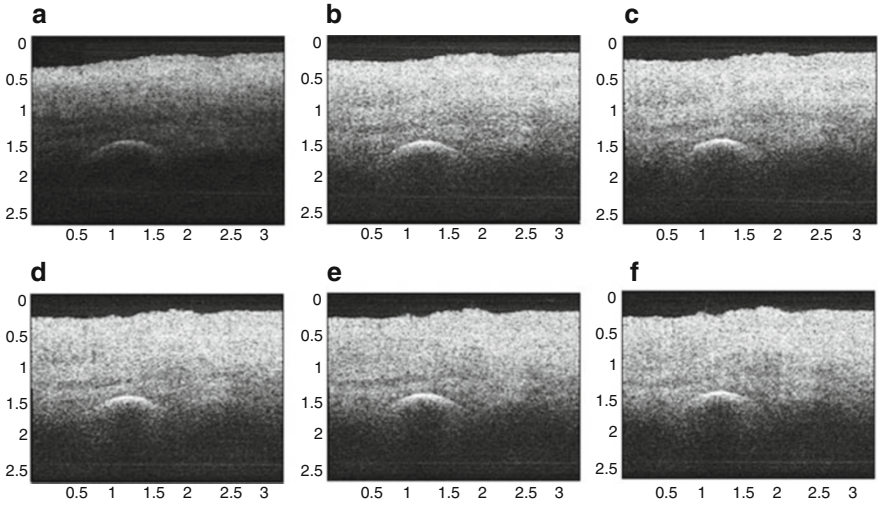

Fig. 16.26 Dynamic OCT images obtained at the time (**a**) 0, (**b**) 10, (**c**) 20, (**d**) 30, (**e**) 40, and (**f**) 50 min after the topical application of 50 % DMSO solution onto the porcine stomach tissue. All the units presented are in millimeters, and the vertical axis presents the imaging depth [188]

intervals of 0, 10, 20, 30, 40, and 50 min, respectively. Like the case with glycerol, it is also demonstrated that a significant improvement of the imaging depth is achieved in Fig. 16.26b–f when compared with Fig. 16.26a after the application of DMSO. The penetration depth has increased to about 2.0 mm after 50 min

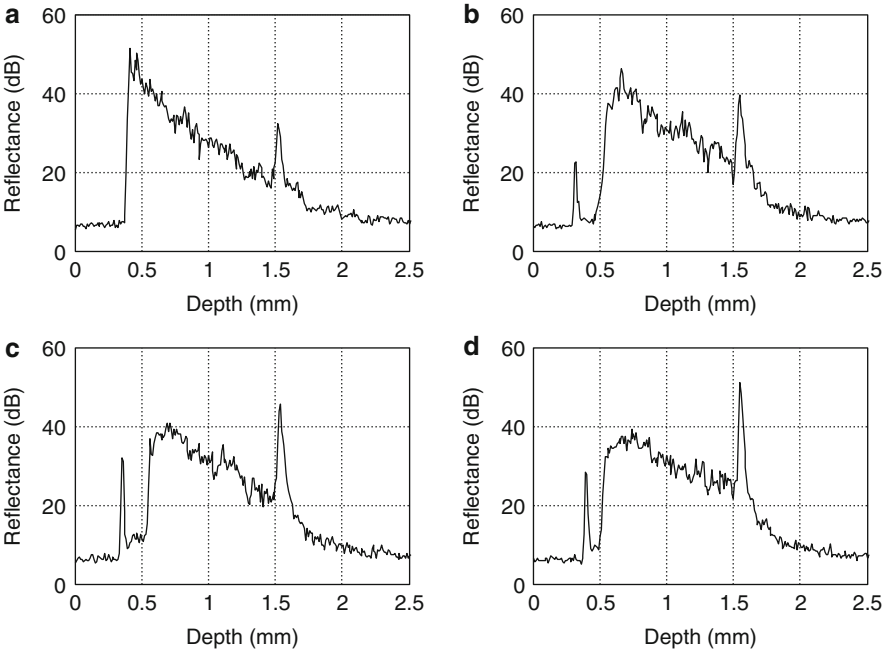

Fig. 16.27 The measured OCT in-depth back-reflectance profiles at the following times: (**a**) 0, (**b**) 10, (**c**) 30, and (**d**) 50 min after topical application of glycerol solution [188]

application of DMSO, as shown in Fig. 16.26f. However, image contrast enhancement was hardly observed during any period of time in the experiments. Tissue shrinkage due to the dehydration of the tissue is not clear, as seen from Fig. 16.26b–f. The reflection signal from the needle surface is approximately the same level from Fig. 16.26b–f.

To further illustrate the different dynamics induced by the two agents, back-reflectance signals along with depth from the stomach tissue with glycerol and DMSO administrations are quantitatively plotted in Figs. 16.27 and 16.28, respectively. The signals were obtained at the different time intervals of 0, 10, 30, and 50 min, respectively, at the same spatial point, but averaged over 10 repeated scans to minimize the random noise. It can be seen from Fig. 16.27a that, after application of glycerol, the strength of the reflectance signal is reduced gradually, starting from the superficial layers, while the signals coming from the needle surface are gradually raised from about 32, 40, and 45 dB to 50 dB, as shown in Fig. 16.27a–d. This suggests that the scattering property of tissue is reduced that is a function of the time duration. However, for the DMSO case, as shown in Fig. 16.28, the reflectance signal from the needle surface was increased from about 28 to 50 dB immediately after the application of agent; see Fig. 16.28a, b for comparison. After about 1 min, the signals from the tissue surface, deeper layer of tissue, and the needle surface remain almost the same level; see Fig. 16.28b–d.

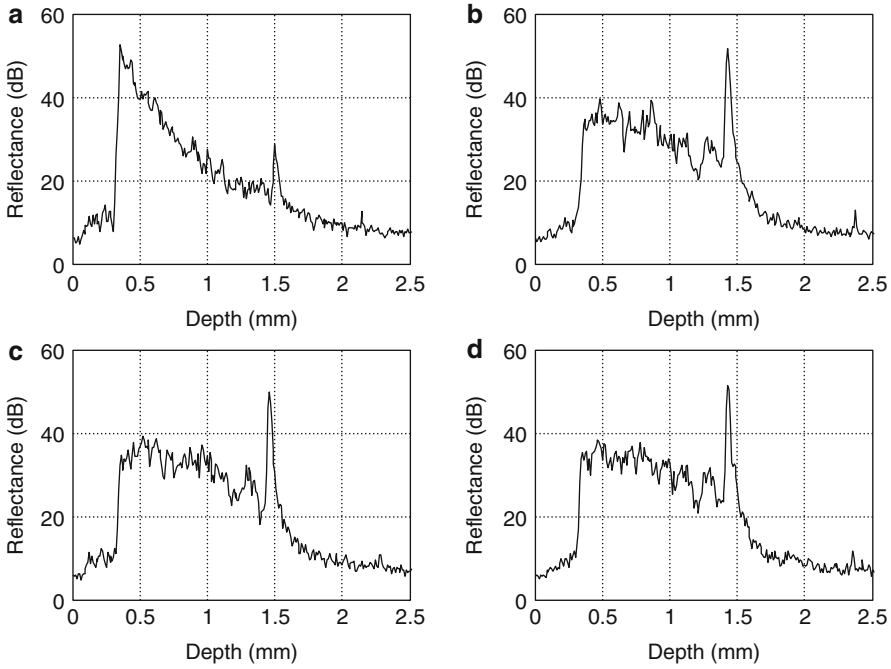

Fig. 16.28 The measured OCT in-depth back-reflectance profiles at the following times: (**a**) 0, (**b**) 10, (**c**) 30, and (**d**) 50 min after topical application of DMSO solution [188]

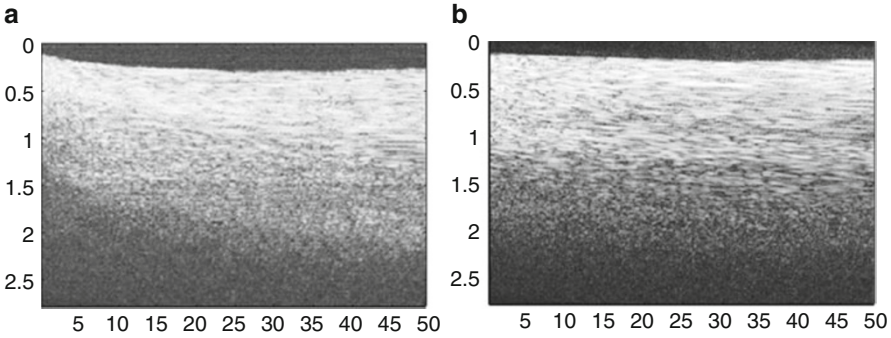

Fig. 16.29 Comparison of the time course of repeated A-scans of the porcine stomach tissue with the application of (**a**) glycerol and (**b**) DMSO, respectively. The horizontal and vertical axes present the time (min) and the imaging depth (mm), respectively [188]

Figure 16.29 illustrates the M-mode OCT images obtained from the repeated A-scans of the porcine stomach with the application of (a) glycerol and (b) DMSO. Because the system used required re-localization of the tissue surface manually after topical application of agents, the registration of OCT signal starts

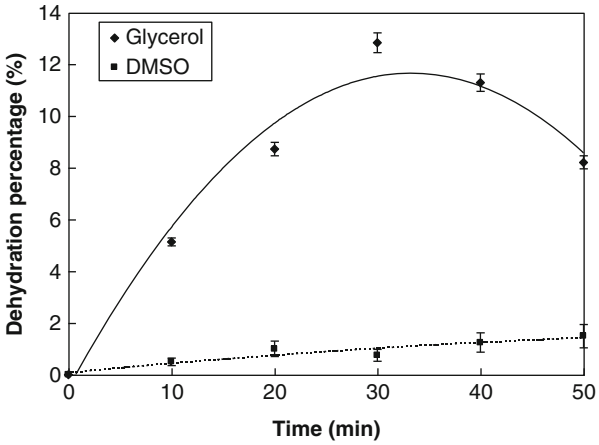

Fig. 16.30 The dynamic dehydration effect of glycerol and DMSO. Data represent average ± SD from three independent experiments [188]

at the time of about 0.5 min after the agent application. From the image obtained with glycerol application, it is clearly seen that the penetration depth increases gradually with the increase of time duration. However, from Fig. 16.29b, a significant depth improvement appears at the time immediately after the application of DMSO. This indicates that DMSO could fulfill tissue clearing within a very short time period. There is a slope of the surface of the tissue. The downward trend of the tissue surface is attributed to the tissue dehydration induced by the chemical agents.

Figure 16.30 shows the dynamics of dehydration effects after the application of the glycerol and DMSO solutions, respectively. It is shown that the application of glycerol causes a greater water loss of stomach tissue than that of DMSO does. During the time period between 0 and 30 min, dehydration induced by glycerol application increases with the time duration; and this reaches a maximum of approximately 12 % at about 32 min. After this time, the curve goes down to 8 %, with the further increase of time to 50 min. It seems that the re-hydration occurs. Water re-enters the tissue, making it swollen. The application of DMSO only causes a small percentage (about 1 %) of dehydration of tissue, and the re-hydration effect was not observed during the time period investigated. These results were consistent with the continuous A-scan experiments as shown in Fig. 16.29.

After glycerol was administrated on the surface of the tissue, it will come to the first diffusion stage mentioned in the last subsection. Note that the tissues used here were stomach tissues. The glycerol would diffuse into the intercellular space of the stomach tissue relatively fast because the epithelial layers of the internal organs are composed of loosely packed cells, and glands and ducts with narrow lumens are rich in the mucosa of the gastrointestinal tract. However, it should be understood that this diffusion rate would still slower than that at which water migrates out from the tissue because of the high osmolarity of the solution and the large molecule of

this agent. This causes tissue dehydration, as observed in Fig. 16.25a–d. After glycerol is diffused into the tissue, it will play its role in not only drawing intercellular fluids out of tissue but also drawing the interstitial water further from cells and fibers. This decreases microscopically the local volume fraction of the scattering centers and the subcellular structure within the cells, thereby increasing the back reflective light signal. On the other hand, this diffusion increases the refractive index of the ground substances. Consequently, such dehydration effect would therefore increase the local reflectance signals leading to the increase of both imaging contrast and depth because OCT actually probes the refractive index difference between macroscopic structures limited by the OCT system resolution, at least in the current study. The concurrent enhancement of imaging depth and contrast are evident from Fig. 16.25c, d.

Glycerol has been found to enter and exit cells by passive diffusion [202]. Therefore, with the elapsing of time, glycerol will further diffuse into the cells, i.e., the second diffusion stage mentioned above. This causes a full refractive index matching with the subcellular structure. After glycerol enters into cells, it could draw the water back into cells due to its water affinity property, leading to tissue re-hydration, as observed in Fig. 16.29a and 16.30 respectively. During this period, the volume of scattering centers in cells could be enlarged by the re-hydration, and the increase of the local reflectance signals does not occur. However, light scattering still remains small because of the refractive index matching environment created between the chemical agents and the scattering centers within tissue. This explains the OCT images of Fig. 16.25e, f, respectively, where there is the improvement of imaging depth, but the imaging contrast is gradually reduced.

For DMSO, the first-stage diffusion is much faster because of its strong penetration ability (refer to the discussions in the last Sect. 16.5.3). Employing (^{35}S) DMSO, Kolb et al. [207] evaluated the absorption and distribution of DMSO in lower animals and humans. It was reported [207] that 10 min after the cutaneous application in rat, radioactivity was measured in the blood. In humans, radioactivity appeared in the blood 5 min after cutaneous application. One hour after application of DMSO to the skin, radioactivity could be detected in the bones. DMSO has also been found to be one of the most effective agents across cell membranes [208, 209]. These experiments indicate that the duration of the aforementioned second diffusion stage of DMSO also happens within a very short time frame. The fast diffusion rate of DMSO could decrease the osmolarity of the solution rapidly, although the original one is high. Therefore, the application of DMSO will cause lighter dehydration of the tissue than glycerol does. This is confirmed by the experimental results, as shown in Fig. 16.29b and 16.30. This also indicates that a little volume decrease of the scattering centers would occur, and the back reflective light signal would not increase once the agent diffuses into tissue. Consequently, no image contrast enhancement was observed with the OCT measurements, as shown in Fig. 16.26. In other words, the application of DMSO causes a rapid full refractive index matching with the subcellular scattering centers of turbid tissue, leading to the imaging depth but not contrast improvement.

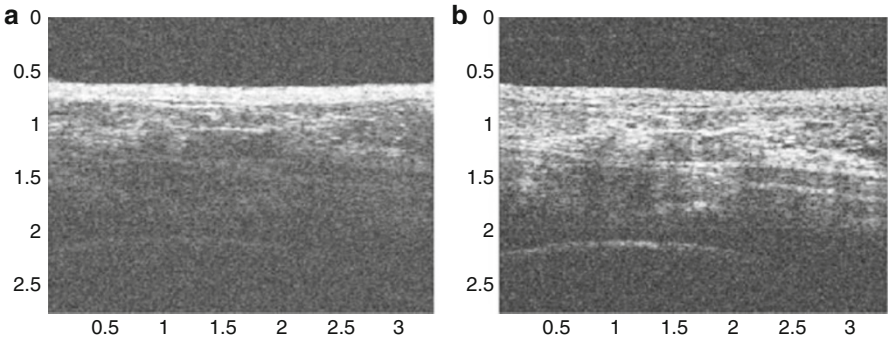

Fig. 16.31 OCT images of chicken skin tissue (**a**) without and (**b**) with 20 min application of glycerol. Both the imaging depth and contrast were enhanced in (**b**) compared with (**a**)

Figure 16.31 shows an even more convincing case for the action of glycerol to the tissue, where the OCT imaging depth and contrast are dramatically improved when comparing the images before and after the application of glycerol agent.

The experimental results by comparison of the tissue clearing dynamics of glycerol and DMSO not only allow us to understand its mechanism, but also are important in the selection of chemicals for the different applications. The above results indicate that DMSO may be more suitable for such applications where high light energy penetration and fast process are desired, for example, photodynamic therapy. Glycerol may be more suitable for the OCT imaging applications where the improvement of both the penetration depth and imaging contrast are required.

It should be pointed out that the above experiments were performed in vitro on biological tissues. The dynamic optical clearing effect induced by the chemical agent would differ from that of the in vivo case. Because of the cell self-regulation and blood circulation, the living tissues would have a less dehydration after the application of hyperosmotic chemical agent. However, a study conducted by Wang et al. [187] showed that the application of the propylene glycol agent solution to the human tissue in vivo has the effect of enhancement of both the imaging depth and contrast. See Fig. 16.32 for an example. Whether this is due to the simultaneous actions of dehydration and chemical diffusion, as suggested in the current study, remains unclear.

Thus far, we have used the examples to illustrate that the impregnation of tissue with a biocompatible chemical can enhance OCT imaging capabilities through the optical clearing and chemical mass transport upon diffusion mechanisms. However, such imaging capability enhancement is agent selectable, particularly for the imaging contrast enhancement. The mechanisms for light penetration enhancement have been well established, i.e., in the framework of the refractive index matching approach, which can improve the OCT imaging depth and resolution. The explanations for imaging contrast enhancement, thereby the improvement of OCT

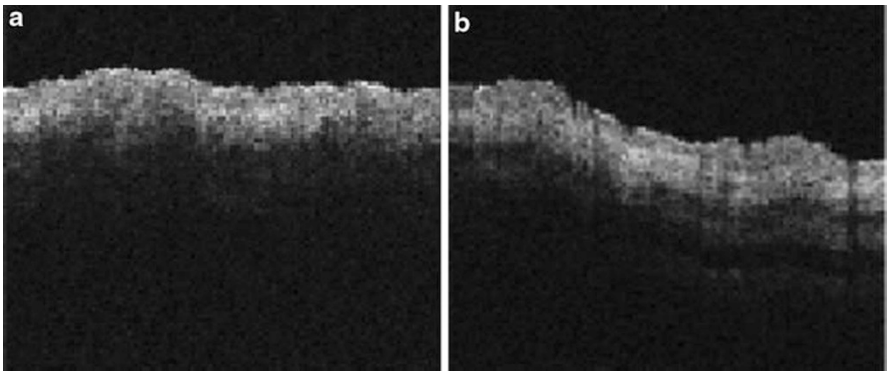

Fig. 16.32 OCT images captured from human forearm in vivo (**a**) without and (**b**) with 50 % topical application of propylene glycol solution. Image sizes: 1.8 × 1.6 mm [187]

localization capability, are based on the dehydration induced by the chemicals and chemical mass transport characteristics. The exact mechanism behind the contrast enhancement remains to be explored.

16.5.4 Imaging through Blood

As follows from above discussion, OCT is a powerful technique for the study of the structure and dynamics of highly scattering tissues and blood, including imaging of the vascular system for the diagnosis of atherosclerotic lesions. In vitro studies performed on human aorta have shown that OCT is able to identify structural features such as lipid collections, thin intimal caps, and fissures characteristic of plaque vulnerability [123, 151, 152, 210]. In in vivo OCT imaging of the rabbit aorta through a catheter, a vascular structure was defined, but saline infusion was required during imaging since blood led to significant attenuation of the optical signal [152]. Eliminating the need for saline or minimization of its concentration would represent a substantial advance for intravascular OCT imaging.

Refractive index mismatch between erythrocyte cytoplasm and blood plasma causes strong scattering of blood that prevents getting high-quality images of intravascular structures through whole blood. The refractive index of erythrocyte cytoplasm is mostly defined by hemoglobin concentration (blood hematocrit) [211]. The scattering properties of blood are also dependent on erythrocyte volume and shape, which are defined by blood plasma osmolarity [211, 212] and aggregation or disaggregation ability [124, 164, 213, 214]. Recently, the feasibility of index matching as a method to overcome the limited penetration through blood for getting of OCT tissue images has been demonstrated [124, 164, 185]. Glucose, low and high molecular dextrans, X-ray contrasting, glycerol, and other biocompatible agents were used to increase the refractive index of blood plasma closer to that of the erythrocyte cytoplasm to improve penetration depth of OCT images.

The 1,300 nm OCT system was used for taking images of the reflector through circulated blood in vitro [185]. The total intensity of the signal off the reflector was used to represent penetration. As immersion substances, dextran (group refractive index – 1.52) and IV contrast (group refractive index – 1.46) were taken. Both dextran and IV contrast were demonstrated to increase penetration through blood: 69 ± 12 % for dextran and 45 ± 4 % for IV contrast.

Studies of blood scattering reduction by the immersion technique using various hyperosmotic solutions, which are biocompatible with blood, like glucose, glycerol, propylene glycol, trazograph (X-ray contrasting substance for intravenous injection), and dextran were also described [124, 164]. The 820 and 1,310 nm OCT systems were applied for taking images of the reflector through a 1-mm layer of uncirculating fresh whole blood. It was shown that for uncirculating blood, the sedimentation plays an important role in blood clearing using the immersion technique, and OCT allows for precise monitoring of blood sedimentation and aggregation.

The mean square of the photodetector heterodyne signal current $<i^2(z)>$ received by an OCT system from the probing depth z is a product of two factors: the mean square heterodyne signal in the absence of scattering $<i^2>_0$ and the heterodyne efficiency factor $\Psi(z)$, describing the signal degradation due to the scattering [166, 215–217], i.e.,

$$<i^2(z)> = <i^2>_0 \Psi(z), \tag{16.21}$$

where the factor $<i^2>_0$ is defined as

$$<i^2>_0 = \beta^2 P_R P_S \sigma_b / \pi (w_H)^2 \tag{16.22}$$

with β being the power-to-current conversion factor, P_R and P_S the power of the reference and input sample arm beams, σ_b the effective backscattering cross-section, and w_H the $1/e$ irradiance radius at the probing depth in the absence of scattering, respectively. More precisely, w_H is defined in Refs. [166, 215].

The heterodyne efficiency factor $\Psi(z)$ contains the scattering effects. It has been shown [166, 215] that for only the single scattering contribution

$$\Psi(z) \approx \exp\{-2\mu_s z\}. \tag{16.23}$$

The factor 2 in the exponent of (16.23) accounts for the round-trip attenuation to and from depth z in the sample arm. In the absence of absorption, the scattering coefficient μ_s can be determined from the slope of the OCT signal. For media with absorption and described by the single scattering approximation, the light travels in a ballistic way and Beer's law can be applied to calculate the total OCT attenuation coefficient: $\mu_t = \mu_s + \mu_a$. Consequently, μ_s can be obtained by subtracting the absorption coefficient from the total attenuation coefficient obtained from the slope of the OCT signal.

Thus, the measured signal in the OCT system is defined as [166, 215–217]

$$\left(\left\langle i^2(z)\right\rangle\right)^{1/2} \approx \left(\left\langle i^2\right\rangle_0\right)^{1/2} \left(\exp\left(-2\mu_t z\right)\right)^{1/2}. \tag{16.24}$$

The result of the OCT study is the measurement of optical backscattering or reflectance, $R(z) \propto \left(\left\langle i^2(z)\right\rangle\right)^{1/2}$, from the RBCs versus axial ranging distance, or depth, z. The reflectance depends on the optical properties of blood, i.e., the total attenuation coefficient μ_t. For optical depths less than 4, reflected power can be approximately proportional to $-\mu_t z$ in exponential scale according to the single scattering model [124, 164], i.e.,

$$R(z) = I_0 \alpha(z) \exp(-\mu_t z). \tag{16.25}$$

Here, I_0 is the optical power launched into the blood sample and $\alpha(z)$ is the reflectivity of the blood sample at the depth of z.

Optical clearing (enhancement of apparent transmittance) ΔT by an agent application can be estimated using the following expression:

$$\Delta T = \left[\left(R_{\text{agent}} - R_{\text{saline}}\right)/R_{\text{saline}}\right] \times 100\%, \tag{16.26}$$

where R_{agent} is the reflectance from the backward surface of the vessel within a blood sample with an agent, and R_{saline} is that with a control blood sample (whole blood with saline).

Measurement of OCT reflectance for two depths, z_1 and z_2, allows one to evaluate approximately the attenuation coefficient and its temporal behavior due to reduction of the blood scattering coefficient at agent immersion if reflectivity $\alpha(z)$ is considered as weakly dependent on depth for a homogeneous blood layer

$$R(z_1, t)/R(z_2, t) \approx \exp\{-\mu_t(t)[z_1 - z_2]\} \tag{16.27}$$

or

$$\mu_t(t) = \frac{1}{\Delta z} \ln\left[\frac{R(z_1, t)}{R(z_2, t)}\right], \tag{16.28}$$

where $\Delta z = |z_1 - z_2|$.

The OCT system used is described in Sect. 16.2, and it yields 12 μm axial resolution in free space. This determines the imaging axial resolution, which is comparable with the dimensions of RBCs or small aggregates.

A few different glass vessels of 0.2–2 mm of thickness were used as blood sample holders. For some holders to enhance reflection from the bottom interface, a metal reflector was applied. The sample holder was mounted on a translation stage at the sample arm and was placed perpendicular to the probing beam. The amplitude of reflected light as a function of depth at one spatial point within the sample

Table 16.2 Influence of dextrans (2.43 gdL^{-1}) on light attenuation property of the sample containing 65 % blood and 35 % saline [164]. Data was corrected accounting for algorithm expressed by equation (16.28)

Agent	μ_t (cm^{-1})	ΔT (%)
Saline	74.2	–
Dextran10	76.4	11.9
Dextran70	59.4	100.1
Dextran500	62.4	86.7

was obtained. The result is the measurement of optical backscattering or reflectance, $R(z)$, from the RBCs versus axial ranging distance, or depth, z, described by (16.25). Optical clearing (enhancement of transmittance) ΔT by an agent application was estimated using (16.26). Averaging for a few tenths of z-scans was employed.

Venous blood was drawn from healthy volunteers and stabilized by K2E EDTA K2. For example, blood samples containing dextrans were prepared immediately after blood taking by gently mixing blood and dextran-saline solution with low rate manual rotating for 1 min before each OCT measurement. Four groups of the blood samples with various hematocrit values were investigated in this study [164]. The dextrans used in the experiments were D×10, D×70, and D×500 with the molecular weights (MW) at 10,500, 65,500, and 473,000, respectively.

Table 16.2 gives the results from 65 % blood (from a 24-year-old male volunteer) with 35 % dextran saline solution. The concentration of dextrans used was 2.43 gdL^{-1}. The measurement started immediately after the addition of dextran. It can be seen from Table 16.2 that D×500 and D×70 are effective agents to decrease the light attenuation of blood compared with the saline control (blood with saline), with the total attenuation coefficient decreased from 74.2 cm^{-1} for the saline control to 62.4 and 59.4 cm^{-1}, respectively. The optical clearing capability ΔT was approximately 90 % and 100 % for D×500 and D×70, respectively.

It is interesting that D×500, providing a higher refraction, had less effect than that of D×70 at the same concentration. Moreover, the increase in concentration (refraction power) cannot always achieve higher optical clearance, thus, 0.5 gdL^{-1} D×500 had a stronger effect than 5 gdL^{-1} D×500 in 20 % blood with 80 % saline samples. Better transmittance does not always correlate with lesser scattering coefficient (see Dextran 10).

The changes in scattering property brought above by the addition of dextran solution may first be explained by the refractive index matching hypothesis [184, 185]. It can be seen that scattering can be reduced when the refractive index of plasma is increased.

The refractive index of dextran saline solution was increased with concentration in all molecular weight groups. The measured indices of blood samples with dextrans were in good agreement with the theoretical values calculated according to the equation $n = c_b n_b + (1 - c_b) n_s$, where c_b is the volume fraction (20 %) of whole blood in the diluted sample and n_s is the index of saline with or without dextrans. As expected, the refractive index of blood with dextran increases as the concentration of the added dextran increases due to an increase of the index of the ground matter of the sample.

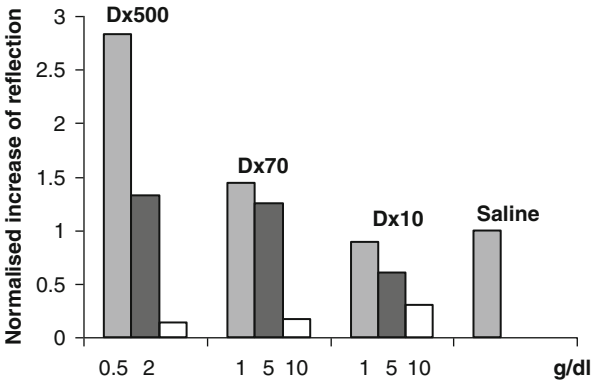

Fig. 16.33 A summary of effects of dextrans compared with that of the saline control on light transmission after 10 min sedimentation. Lower concentration Dx500 and Dx70 had significant effects in enhancing light transmission. Efficiency of higher concentration dextrans was much lower than that of the saline control [164]

Blood optical property can be altered by dextrans-induced refractive index matching between RBCs and plasma. However, refractive index matching is not the only factor affecting blood optical properties. Obviously, this discrepancy resulted from the assumption of only refractive index influence. Thus, other factors should be taken into account, particularly, the cellular aggregation effect induced by dextrans [164].

As the aggregation process is time dependent, the blood sample was allowed 10 min sedimentation in this study after the measurement at the beginning stage of the addition of dextrans. Figure 16.33 shows the summary of the effect of dextrans compared with the saline control on light transmission for the sample with 20 % blood and 80 % saline after 10 min sedimentation. It can be seen from Fig. 16.33 that the influence of dextran on the light transmission was different compared with that at the beginning of mixing dextrans in blood. The lower concentration (0.5 gdL^{-1}) D×500 still had the strongest effect on reducing the scattering of light in blood, with a 2.8-fold stronger effect than that of the saline control. However, enhancement by the highest concentration of D×500 (5 gdL^{-1}) and D×70 (10 gdL^{-1}) was dramatically lower than that of the saline control. At the beginning, they both had a very high blood optical clearing capability with 67.5 % and 76.8 % ΔT, respectively. In addition, the effect was decreased with the increase of dextran in blood within all three groups, contrary to the expectation of the refractive index matching hypothesis.

The decreased aggregation capability of dextran with concentration explained well that light transmission decreased less with the increase of dextran for both types (mid-molecular and large-molecular). Over a range of concentrations, D×500 and D×70 induced RBC aggregation. However, dextrans have been known to exert a biphasic effect on RBC aggregation; they induce aggregation at low concentration and disaggregation at high concentration [214]. For example, with D×70, the maximal aggregation size is obtained at approximately 3 %, above which the size decreases. In our OCT measurements, 2 gdL^{-1} D×500 and 5 gdL^{-1} D×70 in 20 % blood with 80 % saline appeared to be the critical concentration to affect RBC aggregation. Their aggregation parameters became smaller than those of

0.5 gdL^{-1} D×500 and 1 gdL^{-1} D×70. When the concentration increased to 5 gdL^{-1} for D×500 and 10 gdL^{-1} for D×70, they played a role of disaggregation. That is the reason why the cells are much less packed than with the saline control, accounting for the reduced light transmission. Although refractive index matching suggested a higher light transmission, it can be seen that the aggregation-disaggregation effects are now dominant.

The behavior of RBCs in flow is dependent on the processes of aggregation-disaggregation, orientation, and deformation. Increased RBC aggregability has been observed in various pathological states, such as diabetes and myocardial infarction, or following trauma. The aggregation and disaggregation properties of human blood can be used for the characterization of the hemorheological status of patients suffering different diseases [213]. Our work suggests that OCT may be a useful noninvasive technique to investigate rheology for diagnosis, together with its additional advantage of monitoring blood sedimentation [124].

It is well established that RBCs are very sensitive to changes in blood plasma osmolarity [211]. As osmolarity increases due to cell dehydration, the RBC volume decreases, hemoglobin concentration within the cell increases, and index of refraction increases. For example, glucose injection in blood causes the linear increase of plasma osmolarity with glucose concentration, up to 6,000 mOsm/L at glucose concentration in blood plasma of 1.0 g/mL. Using data of Ref. [211], the following empirical relation was suggested to describe RBC volume change with osmolarity [218, 219]:

$$V_{RBC}(osm) = V_{RBC}(300)\left(0.463 + 1.19\exp\left\{-\frac{osm}{376.2}\right\}\right), \tag{16.29}$$

where $V_{\mathrm{RBC}}(osm)$ is the RBC volume in μm^3 at given osmolarity expressed in mOsm/L and $V_{\mathrm{RBC}}(300)$ is the RBC volume at isotonic osmolarity $osm = 300$ mOsm/L. At glucose injection, the local blood hematocrit (Hct) decreases. If Hct before injection of glucose was 45 % at $osm = 300$ mOsm/L; then at $C_{gl} = 0.05$ g/mL, $osm = 580$ mOsm/L and Hct = 32 %; at $C_{gl} = 0.1$ g/mL, $osm = 850$ mOsm/L and Hct = 26 %; and at $C_{gl} = 0.2$ g/ml, $osm = 1{,}400$ mOsm/l and Hct = 22 %. At further increase of glucose concentration (0.3–1.0 g/mL), hematocrit stays constant, Hct ≅ 21 %, in spite of linear increase of blood plasma osmolarity (2,000–6,000 mOsm/L).

Results of modeling of the scattering properties control for a whole blood at its immersion (local intravessel injection in the vicinity of the endoscopic OCT probe) by a glucose solution at different concentrations accounting for RBC polidispersity (150 volume fractions of volume (size) distribution) [220, 221], packing function in the form $F(\mathrm{Hct}) = (1 - \mathrm{Hct})$ [222, 223], osmolarity, and hematocrit effects are presented in Refs. [219, 224]. The scattering coefficient and scattering anisotropy factor were calculated. The scattering coefficient behavior with concentration and the wavelength is defined by: (1) the change in blood plasma osmolarity (increase of scattering for all wavelengths far from Soret band caused by RBC shrinkage and increase of refractive index for low concentration of glucose; (2) reduction of blood hematocrit (plays some role in the scattering decrease for glucose concentration less

than 0.3 g/mL); (3) refractive index matching – the main effect (a significant reduction of scattering for glucose concentration from 0.5 to 0.7 g/mL in dependence of the wavelength); and (4) dispersion of hemoglobin absorbing bands (within a strong Soret band (415 nm) it does not allow a significant reduction of scattering and modifies slightly the position of the dip and the depth of scattering damping for other lower-absorbing hemoglobin bands, 542 and 575 nm). For applications, especially when OCT endoscopy is used, concurrent reduction of scattering and increase of g-factor at immersion agent administration is important. The transport scattering coefficient, $\mu'_s = (1 - g)\mu_s$, decreases and transport free path length for a photon, $l_{tr} \cong 1/\mu'_s$ increases dramatically, thus a larger amount of photons, which carry information about the hidden object (for example, thin-wall plaques in the coronary arteries) can be detected. For the wavelength 900 nm, the scattering coefficient of blood is changed from 1,200 cm^{-1} to approximately 50 cm^{-1} and g-factor from 0.991 to 0.994 at glucose immersion, thus the transport free path length increases more than 35 times [219, 224]. Correspondingly, the depolarization depth of blood [225, 226], which is proportional to l_{tr}, should be much larger at optical clearing. The described method for immersed blood modeling is applicable for any other biocompatible immersion agent administration, such as dextrans, glycerol, and trazograph (see Table 16.2 and Refs. [164, 227]).

There also exists another possibility of blood immersion, using the local blood hemolysis that can be also provided in the vicinity of the fiber-optic endoscopic probe [228]. Free hemoglobin is the immersion agent in that case. The local increase of hemoglobin concentration in plasma can lead to local change of plasma osmolarity [218]:

$$osm' = osm + \frac{C_{bpHe}}{M_{Hb}}, \tag{16.30}$$

where osm is the plasma osmolarity under physiological condition (280–300 mOsm/L), C_{bpHb} is the concentration of plasma hemoglobin, g/L, and M_{Hb} is the molar mass of hemoglobin ($M_{Hb} = 66{,}500$ g/M). The expected change of RBC volume calculated using empirical (16.29) is not more than 0.1 % at hemolysis less than 20 %. For simplicity, the polydispersity of RBC can be taken into account on the basis of the six-fraction blood model [228]. Modeling of optical properties of whole blood at normal conditions and at local hemolysis with the packing function $F(\mathrm{Hct}) = (1 - \mathrm{Hct})(1.4 - \mathrm{Hct})$ [222] showed that, in contrast to the small changes of absorption coefficient, more significant changes of the scattering properties of blood have been observed at increase of free hemoglobin concentration in plasma [228]. A spectrally smooth decrease of scattering coefficient for all wavelengths with free hemoglobin release at hemolysis was found. At a hemolysis rate of 20 %, the decrease of the scattering coefficient for two typical wavelengths, 633 and 820 nm, was calculated as 40 %, while the anisotropy factor, at 633 nm, increases from 0.9940 to 0.9952, and at 820 nm from 0.9919 to 0.9929.

The described method can be realized not only at blood hemolysis but also at local free hemoglobin injection. Hemoglobin administration also may serve as

a clearing agent for tissue clearing, when clearing is needed in the spectral range far from the strong absorption bands of hemoglobin.

This concept was experimentally proved by using a quantitative phase microscopy for investigating RBC morphology and dynamics with subnanometer pathlength sensitivity at the millisecond time scales [229]. The ability to quantify noninvasively the hemoglobin flow out of the cell during hemolysis due to cell refractive index mismatching/matching with surroundings was demonstrated. RBC volume and dynamic morphology were investigated.

A number of experimental studies have demonstrated that glucose and dextrans improve OCT blood penetration [124, 164, 185, 218, 219, 224, 227, 228]. The safety and usefulness of the non-occlusion method for OCT image acquisition with low-molecular-weight dextran L (LMD-L) (Dextran 40) via a guiding catheter were recently demonstrated in clinical studies [230, 231]. The intracoronary frequency-domain optical coherence tomography (FD-OCT) system used in this investigation normally required injection of contrast media for image acquisition, which may lead to the impairment of renal function. To compare the image quality and quantitative measurements between contrast media and LMD-L for FD-OCT image acquisition in coronary stented lesions, 22 patients with 25 coronary stented lesions were enrolled. Using the continuous-flushing method via a guiding catheter, contrast media and LMD-L were infused at a rate of 4 mL/s by an autoinjector. It was shown that, with regard to image quality, the prevalence of clear image segments was comparable between contrast media (97.9 %) and LMD-L (96.5 %), $p = 0.90$, with excellent correlations between both flushing solutions at application to minimal and mean lumen, as well as mean stent areas. The total volumes of contrast media and of LMD-L needed for OCT image acquisition were similar. Thus, LMD-L may have the potential to reduce the total amount of more toxic contrast media without loss of OCT image quality and in the near future could be widely adopted in clinical practice, especially in patients with renal insufficiency. As follows from the above discussion (see Fig. 16.33 and Table 16.2), the high-molecular-weight dextrans are more efficient and we have the prospect of total replacement of contrasting agents.

16.6 Monitoring of Drug Delivery

To describe the relationship between the depth of penetration and the signal strength at a particular depth, a method based on OCT signal slope (*OCTSS*) or OCT amplitude (*OCTA*) analysis can be used [232–236]. In a single scattering approximation [see (16.28)], the *OCTSS* plotted on a logarithmic scale is proportional to the total attenuation coefficient of the tissue, μ_t:

$$OCTSS \equiv \ln\left[\frac{I(z)}{I_0}\right] = -\mu_t z \tag{16.31}$$

The *OCTSS* method allows one to evaluate the average permeability rate of the tissue layer for a chemical agent or molecules of a drug. The permeability rate can

be simply calculated by dividing the thickness of the region used to measure the *OCTSS* by the time of molecular permeation in this region

$$\bar{P} = z_{\text{region}}/t_{\text{region}}. \tag{16.32}$$

Prior to the addition of molecules, the baseline signal would remain relatively constant. Only after application will the changes in the *OCTSS* be observed. The time interval can be calculated as the time when saturation was achieved (after diffusion) minus the time at which the molecules first reached the region of interest (t_{region}). Alternatively, the *OCTA* method of measurement can be used to calculate the permeability rate at specific depths within the tissue from

$$P(z) = z_i/t_{zi}, \tag{16.32}$$

where z_i is the distance from the surface of the tissue where the measurements are performed and t_{zi} is the time of the agent diffusion to that depth.

Many studies have been performed on the effect of OCAs on different biological samples. Optical clearing can be estimated by the change in the optical signal obtained from the tissue, after the addition of the clearing agent, as a percentage change. Formally, percentage change at a certain depth of a tissue can be defined as

$$\%\, clearing = \frac{I_2 - I_1}{I_1} \times 100\%, \tag{16.33}$$

where, I_1 is the optical intensity prior to addition of the clearing agent and I_2 is the optical intensity after the clearing agent has diffused through that particular depth. For example, Ghosn et al. showed that 40 % glucose can induce around 10 % clearing effect in the upper layer of rabbit sclera, which increases to 22 % in the layers below [234]. Larina et al. showed how glycerol can be used as a clearing agent that can help better visualize deeper layers in mice embryo [237]. Sudheendran et al. monitored the changes in tissue as different concentrations of glucose solution diffused through pig skin [238].

It has been demonstrated that the concentration change of OCA in different tissues changes its optical properties [239–253]. Most recently, a method that allows for the quantification of the permeation rates of different compounds in tissues using *OCTSS* has been developed [232–235, 246–251]. Permeation of various molecules and drugs has been quantified in the sclera and the cornea of the eye, monkey skin in vivo, and various vascular tissues. Table 16.3 shows an example for the permeation rates of various molecules and drugs in the rabbit sclera and cornea measured using the *OCTSS* method [234].

In this study [234], an aqueous solution of 40 % glucose is added to rabbit sclera in vitro, where depth-resolved permeability coefficients and optical clearing are measured with OCT. The permeability rate in the upper 80- to 100-μm region is found to be different from that in the deeper 100-μm region: (6.01 ± 0.37) × 10^{-6} cm/s and (2.84 ± 0.68) × 10^{-5} cm/s, respectively. A difference in percent

Table 16.3 Permeation rates of various drugs in rabbit cornea and sclera

	Permeability (rate ± standard deviation, cm/s)	
Drug	Cornea	Sclera
Mannitol	$(1.46 \pm 0.08) \times 10^{-5}$ $(n = 4)$	$(6.18 \pm 1.08) \times 10^{-6}$ $(n = 5)$
Ciprofloxacin	$(1.85 \pm 0.27) \times 10^{-5}$ $(n = 4)$	$(1.41 \pm 0.38) \times 10^{-5}$ $(n = 3)$
Dexamethasone	$(2.42 \pm 1.03) \times 10^{-5}$ $(n = 7)$	–
Metronidazole	$(1.59 \pm 0.43) \times 10^{-5}$ $(n = 5)$	$(1.31 \pm 0.29) \times 10^{-5}$ $(n = 4)$

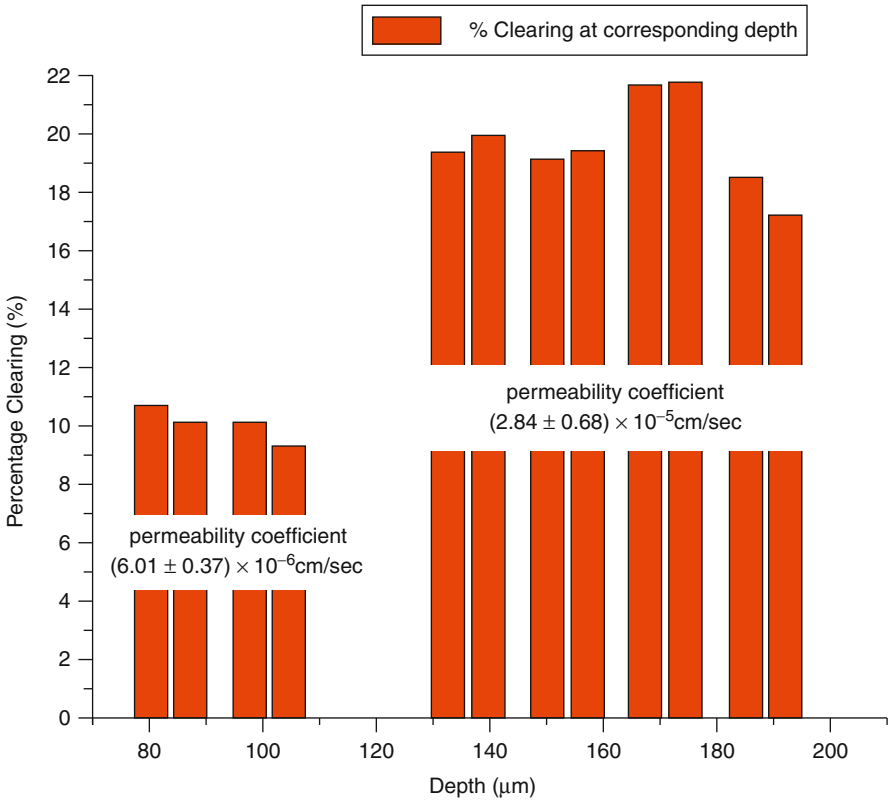

Fig. 16.34 Optical clearing at different depths in rabbit sclera during the 40 % glucose diffusion experiment [234]

clearing is also noted. Optical clearing of the upper region is about 10 % and increased to 17–22 % in the one beneath. These results demonstrate the capability of OCT-based methods to not only measure the diffusion rate and optical clearing of a tissue, but also its ability of functional differentiation between layers of epithelial cells and stroma (see Fig. 16.34).

Recently, OCT has been employed to quantify the permeability rates of glucose and different lipoproteins (very low density lipoprotein (VLDL), low density

Table 16.4 Permeation rates of lipoproteins and glucose in human carotid endarterectomy tissues at 20 °C and 37 °C

	Permeability (rate ± standard deviation, cm/s) × 10^5			
Lipoprotein	Normal, 20 °C	Normal, 37 °C	Diseased, 20 °C	Diseased, 37 °C
VLDL	1.13 ± 0.26	1.20 ± 0.25	1.50 ± 0.21	1.75 ± 0.34
LDL	3.16 ± 0.37	4.77 ± 0.48	1.97 ± 0.34	2.01 ± 0.23
HDL	1.57 ± 0.26	2.42 ± 0.24	2.01 ± 0.32	2.43 ± 0.31
20 % Glucose	3.51 ± 0.27	3.70 ± 0.44	6.31 ± 0.61	5.70 ± 0.48

lipoprotein (LDL), and high density lipoprotein (HDL)) in vascular tissues (porcine aorta and human carotid endarterectomy tissue) [252, 253]. It is also known that structural organization of cells and fibrils composing a tissue could significantly impact the molecular permeability rate and, thus, allow early detection of tissue abnormalities by quantifying permeability rate in normal versus pathological tissues. For example, the permeability rate of 20 % glucose solution in normal vascular tissues was calculated to be $(6.80 \pm 0.18) \times 10^{-6}$ cm/s, while it significantly increased during formation of early arteriosclerotic disease: $(2.69 \pm 0.42) \times 10^{-5}$ cm/s [250].

The influx of lipoproteins is a significant factor in studying the physiological mechanisms that contribute towards the formation of atherosclerosis in vascular tissues. OCT can also be used to measure the perfusion through yet another biological system, the intimal layer of the carotid arterial wall. This layer is obtained from human carotid endarterectomy (CEA) specimens, which contain *normal* healthy segments and *diseased* atherosclerotic segments that included lipidic, calcific, hemorrhagic, and/or fibrotic components. The permeation rates of glucose and different lipoproteins were studied at room temperature (20 °C) as well as physiological temperature (37 °C). The results of these permeation studies are summarized in Table 16.4 [236, 252, 253].

As discussed above and as described in general in Ref. [224], OCT in conjunction with uploading tissue by an OCA holds promise as a research tool for analysis of identifying the boundaries between normal and diseased tissue in vitro and in vivo. Depth- and time-resolved profiles for OCT signal at optical clearing allow one to differentiate human cancer and normal breast tissues [254, 255]. The permeability coefficients [(16.32)] and the percentages of OCT signal enhancement [(16.33)] for normal and cancerous breast tissues have been investigated in vitro for 60 % glycerol [254], 20 % glucose, 40 % glucose, and 20 % mannitol [255]. The OCT slope signals of breast tissues decreased as OCA diffusing into tissues. For example, the permeability coefficient of glycerol in cancer tissues was 3.54-fold larger than that in normal tissues. The permeability coefficient of 60 % glycerol was $(3.14 \pm 0.07) \times 10^{-5}$ cm/s in breast cancer tissues and $(0.89 \pm 0.02) \times 10^{-5}$ cm/s in normal breast tissues [254]. Obtained results indicate that the OCA permeability coefficient in breast cancer tissue is prominently larger than that in normal breast tissue, while the percentage of optical clearing is lower. The results suggest that OCT has the ability to distinguish cancer tissue from different aspects [255] that are related to tissue morphology and OCA impact on tissue.

Pilot results on in vitro quantification of glucose diffusion permeability in normal esophageal epithelium and esophageal squamous cell carcinoma (ESCC) human tissues by using OCT technique were also reported [256]. The permeability coefficient of 40 % glucose was found to be $(1.74 \pm 0.04) \times 10^{-5}$ cm/s in normal esophagus and $(2.45 \pm 0.06) \times 10^{-5}$ cm/s in ESCC tissues. Therefore, a 1.41-fold greater permeability coefficient than that for normal tissues was found for ESCC, however, similar to breast tissue, the OCT light penetration depth for the diseased tissue is significantly smaller than that of normal esophagus tissues in the same time interval.

It was also found that the glucose permeability is nonlinear through the esophagus tissue and increases with depth for both normal and ESCC tissues [257]. The OCT images were acquired continuously for 120 min, and the depth-resolved and average permeability coefficients for the 40 % glucose solution have been extracted from experimental data using the OCT amplitude (*OCTA*) method [232–236]. The depth-resolved permeability coefficient for 40 % glucose solution increases from $(3.30 \pm 0.09) \times 10^{-6}$ and $(1.57 \pm 0.05) \times 10^{-5}$ cm/s at the mucous membrane of normal esophagus and ESCC tissues to $(1.82 \pm 0.04) \times 10^{-5}$ and $(3.53 \pm 0.09) \times 10^{-5}$ cm/s at the submucous layer ~742 μm apart from the epithelial surface of normal esophagus and ESCC tissues, respectively. This result fits well with data from Fig. 16.34, where difference between diffusivity of epithelial cells and stroma is underlined. It is also important to note that the cancer epithelial cell layer becomes 5.5 times more permeative than the normal tissue layer, but the permeability of the stromal layer increases only 2.2 times. The results presented could support the use of OCT in conjunction with OCA application in functional esophageal tissues imaging.

Another important application of OCT is for diagnostics of disease-caused structural changes in dental tissues [258–260]. Monitoring of the molecular diffusion processes was studied in hard tissues such as human tooth [261, 262] and nail [263]. Diffusion of water and dental liquor is necessary for teeth functioning and affects tooth hardness [264]. The permeability of dental tissues to exogenous chemical agents and drugs is important for dental disease treatment and tooth cosmetics [265]. The study of water and glycerol application to dentin samples was implemented in two geometries [261, 262]: (1) the sample placed in a cuvette and OCT-scanning performed through the liquid layer, covering the sample (front application); (2) the sample glued to a window in the cuvette side face (back application). The sample was coated with hermetic varnish except a window for OCA diffusion and light penetration in the case of one side OCA application and two windows on the opposite sides of the sample in the case of backward OCA application. In both cases, OCT-scanning was performed repeatedly over a few hours. The difference found between A-scans for front and backward OCA application is due to competition between the mean attenuation and the back reflectance coefficients. Both parameters decrease at application of diffusing immersion agent, but reduction of the attenuation coefficient leads to OCT signal increase from the sample depth, as the back reflectance decrease causes the corresponding decrease of OCT signal. A remarkable finding is that, in both

Table 16.5 Tooth tissue structural and diffusion parameters obtained from microscopy and OCT

Agent	Sample thickness, mm	Mean tubule diameter, μm	Saturation time, min	Permeability rate, cm/s
Water	0.9	0.60 ± 0.10	78	$(3.04 \pm 0.13) \times 10^{-6}$
Water	1.3	2.30 ± 0.15	9	$(4.02 \pm 0.24) \times 10^{-5}$
Water	1.2	1.60 ± 0.13	154	$(2.09 \pm 0.65) \times 10^{-6}$
44 % glycerol	0.8	2.4 ± 0.55	54	$(4.91 \pm 0.67) \times 10^{-6}$

cases, the mean slope of the OCT signal decreases with time and the ultimate damping time constants agree well. Backward OCA application is free of artifacts introduced by the liquid layer over the sample and hence was used in further experiments with other agents.

Similar measurements were carried out for other samples for water and 44 % glycerol aqueous solution (summarized in Table 16.5). The results demonstrate some correlation of the diffusion rate and time of OCT signal saturation with tissue structure, i.e., the tubules' diameter and their number density. The glucose diffusion and glucose impact on the dentin permeability that is important for *diabetes mellitus* patients were also studied. It has been found that the permeability coefficient for 35 % aqueous solution of glucose is about two orders of magnitude smaller than that for water (naturally, due to the greater molecule size and, possibly, due to molecular binding). The diffusion process of water in tooth samples was investigated before and after the long-term (5 days) incubation of a sample with 35 % glucose. The permeability coefficients of intact and incubated samples were found to be $(2.59 \pm 1.63) \times 10^{-4}$ cm/s and $(3.86 \pm 0.39) \times 10^{-4}$ cm/s, respectively. Thus, the long-term glucose impact on the tooth dentin results in irreversible changes of the tissue properties that may result from the glycation-induced change of the intertubular dentin density and, hence, the increased tubule looseness.

An in vivo study of molecular diffusion in a volunteer's partly removed nail was also performed [263]. OCT measurement allowed for identification of each tissue layer (nail and underlying tissue) and evaluation of its optical thickness and attenuation (scattering) coefficient. The effect of glycerol diffusion and mechanical compression (see Sect. 16.8) was clearly seen for all layers.

Overall, these results demonstrate the capability of OCT technology to quantify time- and depth-dependent diffusion processes in many soft and hard tissues. Moreover, the difference in diffusion rates between normal and diseased tissues measured with OCT could assist in tissue classification/pathology efforts.

16.7 Glucose Sensing

Significant efforts were undertaken in the field of glucose sensing in tissues with OCT and encouraging results were obtained in several studies [240, 242, 245, 266–275]. Glucose concentration monitoring is based on the similar phenomena as tissue optical

clearing and drug delivery and uses matching of refractive indices of the interstitial fluid, where glucose migrates from blood vessels, and tissue scattering constituents. By registering changes in scattering that are seen as the OCT signal slope changes, it is possible to evaluate changes in glucose concentration. Fortunately, as was proved in pioneering papers by Esenaliev et al. [245] and Larin et al. [240, 242], a high sensitivity of OCT slope measurement allows for in vivo monitoring of glucose at physiological levels in tissues of animals and humans.

Glucose clamping experiments were performed in the animal studies [240]. The clamping technique allowed slow, controlled intravenous administration of glucose at desired rates to simulate normal physiological changes in blood glucose concentration. A dextrose solution (50 % w/w) was administrated for approximately 1 h using a digital pump at a rate of 1.2 mL per min. This resulted in an increase of blood glucose concentration from a baseline level of 100 mg/dL (~5.5 mM) to 400 mg/dL (~22.2 mM). The *OCTSS* was measured at the depth from 300 to 400 μm and changed approximately 53 % in the range from 100 to 400 mg/dL. The lag time between an increase of blood glucose concentration and a decrease of the OCT signal slope was approximately 14 min and can be explained by glucose diffusion from bloodstream to skin.

An 80 % decrease of the slope of the OCT signal at the depth of 380–480 μm as the blood glucose increased from 144 mg/dL to 600 mg/dL (3.2 %/mM) was observed in an experiment with rabbit lip [240]. Good linear correlation between the OCT signal slope and blood glucose concentration with a correlation coefficient of 0.93 and a p-value less than 0.01 was demonstrated.

For healthy human volunteer [242], the slopes changed significantly: ~17 %, with changes in glucose concentration from 90 to 140 mg/dL. These results also demonstrated good correlation between changes in slopes of noninvasively measured OCT signals and actual blood glucose concentration. On average, the slope changed 1.9 % per 10 mg/dL change of the blood glucose concentration.

16.8 Compression Clearing and Contrasting

A mechanical stress on a soft tissue in the form of compressing or stretching causes a significant increase in its optical transmission due to less overall light scattering [175, 224, 236, 276–287]. For living tissues, the major mechanisms behind this phenomenon are: (1) increased optical tissue homogeneity due to removal of blood and extracellular fluid from the compressed site; (2) closer packing of tissue components, leading to constructive interference (cooperative) effects; and (3) less tissue thickness.

The estimation of biomechanical properties of tissue is critical to many areas of the health sciences, including monitoring of the tension in wound closures, skin flaps, and tissue expanders. Optical and especially OCT techniques are helpful in such studies.

Askar'yan [277] was the first to study the propagation of a laser beam through the soft tissue phantoms and human palm at mechanical compression. The reduction of extinction coefficient after tissue compression and prolongation

of optical clearing effect after removing pressure for some time interval were successfully demonstrated.

As a tissue that is well-supplied with blood, the skin's spectral properties can be effectively controlled by applying an external localized pressure in in vivo experiments when UV-induced erythema (skin redness) is developed [287]. For that particular case, extra blood in the skin dermis resulting from a physiological reaction to UV light is pushed out by compression, thus providing better light transmittance within the bands of hemoglobin even the induced erythema without compression is rather strong.

The squeezing-induced effects in tissues containing little or no blood, such as eye sclera, are characterized by a marked inertia (a few minutes) [224, 284]. This happens because of the relatively slow diffusion of water from the compressed site. Due to water displacement from the interspace between collagen fibrils, concentration of the proteins and mucopolysaccharides increases in this space. Since these proteins and sugars have a refractive index closer to that of the collagen fibrils, a more index-matched environment can be created.

On the other hand, compression reduces specimen thickness d, which might increase the effective scatterer concentration inside the tissue. Therefore, compression may also give rise to an increase in tissue scattering coefficient μ_s. Sometimes the increase in scatterer concentration is likely to be more dominant than the reduction in index mismatch [175]. In addition, reduction of tissue thickness causes an increase in local chromophore concentration, and thus the absorption coefficient μ_a increases. However, the total effect on optical properties changes, which is proportional to the product of $(\mu_s + \mu_a)d$, and is characterized by less light attenuation due to the smaller thickness of compressed soft tissue (up to 72 %) [175, 285, 286]; cooperative effects also may have a great influence in reduction of the overall scattering [224].

Steady-state diffuse reflectometry with a variable source-detector separation r_{sd} allows one to characterize properties of light propagation in a tissue at mechanical tension, including its anisotropy following the stretching direction [283]. At external forced tension, more significant damping of scattering along the direction of mechanical stress is expected. In vivo human experiments showed that the specular reflection from skin changes with stretch [280]. For small values of skin stretch, the specular reflectivity measured for He:Ne laser ($\lambda = 633$ nm) beam with the 45° angle of incidence increases linearly with strain, showing considerable anisotropic properties.

All above-mentioned early studies of tissue compression have stimulated application of this technology to OCT, where the penetration depth and image contrast issues are critical. The authors of Ref. [279] used a hemispherically tipped glass rod (borosilicate, $n_{\text{glass}} = 1.474$) 20 mm long with a 3-mm tip diameter, as a probe for localized skin compression and concurrent OCT imaging at mean wavelength 1,310 nm (swept source OCT system). The glass rod did not add any perceivable distortions to the OCT signal. It was demonstrated that for similar effective tissue strain, air dehydration and mechanical compression produce similar changes in refractive index and water volume fraction. These data directly prove the concept

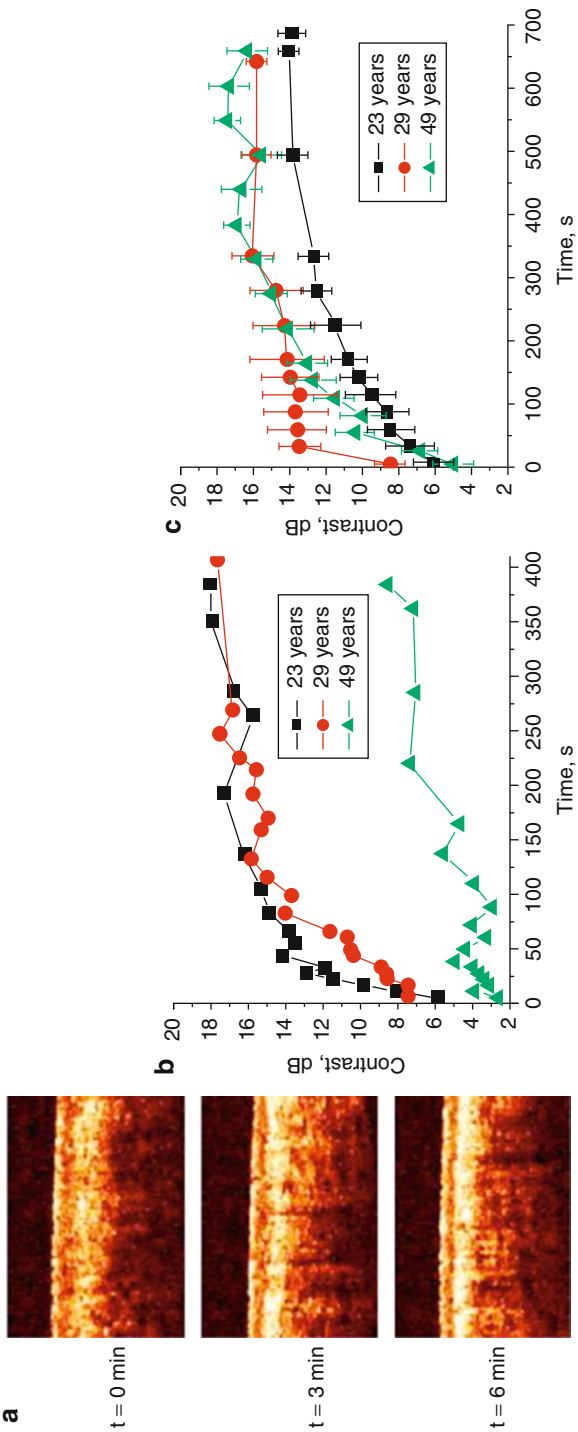

Fig. 16.35 (**a**) OCT images of thin skin of 29-year-old male volunteer immediately after compression started ($t = 0$), at 3 min, and at 6 min for high-pressure regime (0.35 N/mm^2); (**b**, **c**) temporal characteristics of contrast of epidermis–dermis junction for three volunteers of different age for low-pressure (0.07 N/mm^2) (**b**) and high-pressure (0.35 N/mm^2) (**c**) compression [282]

that mechanical compression may cause local water removal within compressed tissue sites. This water may then be transported from the compressed site laterally along interstitial pressure gradients, increasing local protein concentration. Mechanical compression results in higher OCT signal intensity, i.e., higher contrast and thus better imaging capability. The localized mechanical compression of skin decreases tissue thickness and water content and increases refractive index and OCT signal intensity. Mechanical loading may also decrease absorption and scattering in the compressed region, particularly at 1,310 nm, near the 1,450 nm absorption peak of water (low concentration of water due to its displacement).

The effect of mechanical compression on the contrast between epithelial and stromal layers of human rectum ex vivo in OCT images was studied in Ref. [276]. Due to different mechanical properties and water content of these layers, the changes of scattering properties induced by compression are different, which leads to better contrasting of these layers in OCT images. The same group has reported studies on continuous mechanical compression of human thin skin in vivo [282]. The OCT images (mean wavelength 910 nm, axial and transverse spatial resolution of 15 and 25 μm in air, respectively) were obtained for three male volunteers of different ages at low and high mechanical pressures. The OCT probe was placed in a special holder allowing for control of the force of pressure on the skin and keeping it constant. The probe was pressed onto human skin with force varying from 0.4 N (pressure 0.07 N/mm^2) to 2 N (0.35 N/mm^2) and was held in such a position for 10–15 min while the OCT images of the skin were acquired continuously at a rate of one image every 5 s. The OCT signal (A-scan) was averaged over the transverse direction in the region uniform in the transverse (in respect to probe beam) direction of 200 μm-width (Fig. 16.35a); from this averaged A-scan OCT signals (in dB) for particular layers were extracted; the difference of these signals for neighboring layers was attributed as image contrast corresponding to the ratio of the OCT signals indicated in dB (Fig. 16.35b, c). The temporal dependencies of OCT image contrast for the epidermis–dermis junction measured at low and high pressures are presented in Fig. 16.35b, c.

For the 23-year-old volunteer, the image contrast increased monotonously with time for both the low- and high-pressure regimes. The maximal contrast was reached much faster for the high pressure than for the lower, less than 1 min was enough to reach the similar contrast for which at the low pressure more than 3 min was needed. The skin of the older volunteer (49 years old) demonstrates an increase in junction contrast, especially at the high-pressure regime that reaches a similar maximum as for younger skin at the sixth min. Evidently, these changes could be associated with the different dynamics of water inflow, in particular connected with the different balance of free and bounded water for the young and aged skin.

16.9 Summary

In summary, we have discussed in this chapter the basic principles of an optical coherence tomography system and have shown briefly its applications, both medical and non-medical. The emphasis was placed on the low-coherence

interferometry that consists of the building block for optical coherence tomography. OCT based on the time modulation of the interference signal, i.e., modulation of the time delay in order to increase the signal-to-noise ratio of the system, was discussed, while other variations of OCT systems were left for readers to refer to the existing literatures. Several features of OCT suggest that it will be an important technique for both biomedical imaging and industrial applications. These features include: (1) high axial resolution of 1–15 μm, one to two orders of magnitude higher than conventional ultrasound; (2) noninvasive and non-contact, which imply that the imaging can be performed without the contact with the sample and without the need to excise the specimen; (3) high speed, enabling real-time imaging; (4) flexibility, in that it can be integrated into almost all medical imaging modalities; (5) cost-effectiveness and portability, because the system can be implemented by optic-fibers commercially available in the telecommunication industrials.

For further reading on OCT advanced systems and broader biomedical applications, we recommend the following comprehensive OCT monographs: [82, 135, 288].

Human tissue is highly scattering in nature to the near infrared light that is usually used to illuminate the OCT systems. In the second part of this chapter, it was shown that multiple scattering of tissue is a detrimental factor that limits OCT imaging performance, for example, the imaging resolution, depth, localization, and contrast. In order to improve the imaging capabilities for OCT systems, the multiple scattering of tissue must be reduced.

The last part of this chapter introduced a novel technique, i.e., using a biocompatible and hyperosmotic chemical agent to impregnate the tissue, to enhance the OCT imaging performances through the tissue. The mechanisms for such improvements, for example, imaging depth and contrast, were discussed, with primary through the experimental examples. It is assumed that when chemical agents are applied onto the targeted sample, there are two approaches concurrently applied to the tissue. The imaging depth, or light penetration depth, is enhanced by the refractive index matching of the major scattering centers within the tissue with the ground material induced by the chemical agents, usually through the diffusions of the interstitial liquids of tissue and the chemical agents. The imaging contrast enhancement is caused by the tissue dehydration due to the high osmotic characteristics of the chemical agents, which is also dependent on the mass transport of chemical agents within tissue.

Additional information on tissue optical clearing mechanisms, biomedical applications, benefits, and limitations, including toxcicity issues, can be found in monographs, special issues of journals, and overview publications [168, 224, 236, 266, 289–298]. Tissue optical clearing is an exciting field of research, specifically in further development of OCT technologies. In particular, it allows one to image of superficial skin vessels using a compact low-power OCT Doppler system [299, 300]. The development of OCT technology in conjunction with optical clearing stimulates designing of novel biocompatible OCAs and compositions with enhancers [301, 302].

Acknowledgments Some of the results presented in this chapter were made possible with financial support received from the Engineering and Physical Science Research Council, UK, for the projects GR/N13715, GR/R06816, and GR/R52978; the North Staffordshire Medical Institute, UK; Keele University Incentive Scheme; Cranfield University Start-up fund; and the Royal Society for a joint project between Cranfield University and Saratov State University; as well as grants CRDF REC-006, 1177.2012.2 "Support for the Leading Scientific Schools" from the President of the RF, 11-02-00560-a RFBR, 224014 PHOTONICS4LIFE of FP7-ICT-2007-2, 1.4.09 of RF Ministry of Education and Science; RF Governmental contracts 02.740.11.0770, 02.740.11.0879, and 11.519.11.2035; FiDiPro, TEKES Program (40111/11), Finland; SCOPES Project IZ74ZO_137423/1 of Swiss National Science Foundation. National Institutes of Health, USA, for the projects R01HL093140, R01HL093140S, R01EB009682 and R01DC010201, and the American Heart Association (0855733G).

References

1. A. Yodh, B. Chance, Spectroscopy and imaging with diffusing light. Phys. Today **48**, 34–40 (1995)
2. D. Delpy, Optical spectroscopy for diagnosis. Phys. World **7**, 34–39 (1994)
3. B.R. Masters, P.T.C. So (eds.), *Handbook of Biomedical Nonlinear Optical Microscopy* (Oxford University Press, New York, 2008)
4. M. Rajadhyaksha, M. Grossman, D. Esterowitz, R. Webb, R. Anderson, In-vivo confocal scanning laser microscopy of human skin – melanin provides strong contrast. J. Invest. Dermatol. **104**, 946–952 (1995)
5. A.F. Fercher, Optical coherence tomography. J. Biomed. Opt. **1**, 157–173 (1996)
6. J.M. Schmitt, Optical coherence tomography (OCT): a review. IEEE J. Sel. Top. Quantum Electron. **5**, 1205–1215 (1999)
7. D. Huang, E.A. Swanson, C.P. Lin, J.S. Schuman, W.G. Stinson, W. Chang, M.R. Hee, T. Flotte, K. Gregory, C.A. Puliafito, J.G. Fujimoto, Optical coherence tomography. Science **254**, 1178–1181 (1991)
8. A.F. Fercher, C.K. Hitzenberger, W. Drexler, G. Kamp, H. Sattmann, In vivo optical coherence tomography. Am. J. Ophthalmol. **116**, 113–114 (1993)
9. J.M. Schmitt, A. Knüttel, M. Yadlowsky, R.F. Bonner, Optical coherence tomography of a dense tissue: statistics of attenuation and backscattering. Phys. Med. Biol. **42**, 1427–1439 (1994)
10. J.G. Fujimoto, M.E. Brezinski, G.J. Tearney, S.A. Boppart, B.E. Bouma, M.R. Hee, J.F. Southern, E.A. Swanson, Optical biopsy and imaging using optical coherence tomography. Nat. Med. **1**, 970–972 (1995)
11. G.J. Tearney, M.E. Brezinski, B.E. Bouma, S.A. Boppart, C. Pitris, J.F. Southern, J.G. Fujimoto, In vivo endoscopic optical biopsy with optical coherence tomography. Science **276**, 2037–2039 (1997)
12. R.C. Youngquist, S. Carr, D.E.N. Davies, Optical coherence domain reflectometry: a new optical evaluation technique. Opt. Lett. **12**, 158–160 (1987)
13. K. Takada, I. Yokohama, K. Chida, J. Noda, New measurement system for fault location in optical waveguide devices based on an interferometric technique. Appl. Opt. **26**, 1603–1606 (1987)
14. A.F. Fercher, K. Mengedoht, W. Werner, Eye-length measurement by interferometry with partially coherent light. Opt. Lett. **13**, 1867–1869 (1988)
15. C.K. Hitzenberger, W. Drexler, A.F. Fercher, Measurement of corneal thickness by laser Doppler interferometry. Invest. Ophthalmol. Vis. Sci. **33**, 98–103 (1992)
16. J.A. Izatt, M.R. Hee, E.A. Swanson, C.P. Lin, D. Huang, J.S. Schuman, C.A. Puliafito, J.G. Fujimoto, Micrometer-scale resolution imaging of the anterior eye with optical coherence tomography. Arch. Ophthalmol. **112**, 1584–1589 (1994)

17. W. Clivaz, F. Marquis-Weible, R.P. Salathe, R.P. Novak, H.H. Gilgen, High-resolution reflectometry in biological tissue. Opt. Lett. **17**, 4–6 (1992)
18. M.R. Hee, J.A. Izatt, E.A. Swanson, D. Huang, C.P. Lin, J.S. Schuman, C.A. Puliafito, J.G. Fujimoto, Optical coherence tomography of the human retina. Arch. Ophthalmol. **113**, 326–332 (1995)
19. S.A. Boppart, M.E. Brezinski, B.E. Bouma, G.J. Tearney, J.G. Fujimoto, Investigation of developing embryonic morphology using optical coherence tomography. Dev. Biol. **177**, 54–63 (1996)
20. C.A. Puliafito, M.R. Hee, C.P. Lin, J.G. Fujimoto, Imaging of macular disease with optical coherence tomography. Ophthalmology **102**, 217–229 (1995)
21. C. Pitris, C. Jesser, S.A. Boppart, D. Stamper, M.E. Brezinski, J.G. Fujimoto, Feasibility of optical coherence tomography for high resolution imaging of human gastrointestinal tract malignancies. J. Gastroenterol. **35**, 87–92 (2000)
22. S. Brand, J.M. Poneros, B.E. Bouma, G.J. Tearney, C.C. Compton, N.S. Nishioka, Optical coherence tomography in the gastrointestinal tract. Endoscopy **32**, 796–803 (2000)
23. B.E. Bouma, G.J. Tearney, C.C. Compton, N.S. Nishioka, High-resolution imaging of the human esophagus and stomach in vivo using optical coherence tomography. Gastrointest. Endosc. **51**, 467–574 (2000)
24. S. Jackle, N. Gladkova, F. Feldchtein, A. Terentieva, B. Brand, G. Gelikonov, V. Gelikonov, A. Sergeev, A. Fritscher-Ravens, J. Freund, U. Seitz, S. Schroder, N. Soehendra, In vivo endoscopic optical coherence tomography of the human gastrointestinal tract – toward optical biopsy. Endoscopy **32**, 743–749 (2000)
25. R.K. Wang, J.B. Elder, Propylene glycol as a contrasting agent for optical coherence tomography to image gastro-intestinal tissues. Lasers Surg. Med. **30**, 201–208 (2002)
26. B.W. Colston, M.J. Everett, L.B. Da Silva, L.L. Otis, P. Stroeve, H. Nathel, Imaging of hard- and soft-tissue structure in the oral cavity by optical coherence tomography. Appl. Opt. **37**, 3582–3585 (1998)
27. J.M. Schmitt, M.J. Yadlowsky, R. Bonner, Subsurface imaging of living skin with optical coherence tomography. Dermatology **191**, 93–98 (1995)
28. N.D. Gladkova, G.A. Petrova, N.K. Nikulin, S.G. Radenska-Lopovok, L.B. Snopova, Y.P. Chumakov, V.A. Nasonova, V.M. Geilkonov, G.V. Geilkonov, R.V. Kuranov, A.M. Sergeev, F.I. Feldchtein, In vivo optical coherence tomography imaging of human skin: norm and pathology. Skin Res. Technol. **6**, 6–16 (2000)
29. R.K. Wang, J.B. Elder, High resolution optical tomographic imaging of soft biological tissues. Laser Phys. **12**, 611–616 (2002)
30. J.G. Fujimoto, B.E. Bouma, G.J. Tearney, S.A. Boppart, C. Pitris, J.F. Southern, M.E. Brezinski, New technology for high speed and high resolution optical coherence tomography. Ann. N. Y. Acad. Sci. **838**, 95–107 (1998)
31. C. Passmann, H. Ermert, A 100 MHz ultrasound imaging system for dermatologic and ophthalmologic diagnostics. IEEE Trans. Ultrason. Ferroelect. Freq. Control **43**, 545–552 (1996)
32. P.A. Flournoy, White light interferometric thickness gauge. Appl. Opt. **11**, 1907–1915 (1972)
33. T. Li, A. Wang, K. Murphy, R. Claus, White light scanning fibre Michelson interferometer for absolute position measurement. Opt. Lett. **20**, 785–787 (1995)
34. Y.J. Rao, Y.N. Ning, D.A. Jackson, Synthesised source for white light sensing system. Opt. Lett. **18**, 462–464 (1993)
35. J.W. Goodman, *Statistical Optics* (Wiley, New York, 1985), pp. 164–169
36. R.K. Wang, Resolution improved optical coherence-gated tomography for imaging through biological tissues. J. Mod. Opt. **46**, 1905–1913 (1999)
37. A. Podolenau, D.A. Jackson, Noise analysis of a combined optical coherence tomograph and a confocal scanning ophthalmoscope. Appl. Opt. **38**, 2116–2127 (1999)
38. P.R. Gray, R.G. Meyer, *Analysis and Design of Integrated Circuits*, 2nd edn. (Wiley, New York, 1984)

39. V.M. Gelikonov, G.V. Gelikonov, N.D. Gladkova et al., Coherent optical tomography of microscopic inhomogeneities in biological tissues. JETP Lett. **61**, 149–153 (1995)
40. G.J. Tearney, B.E. Bouma, S.A. Boppart, B. Golubovic, E.A. Swanson, J.G. Fujimoto, Rapid acquisition of in vivo biological images by use of optical coherence tomography. Opt. Lett. **21**, 1408–1410 (1996)
41. T. Ko, D. Adler, J. Fujimoto, D. Mamedov, V. Prokhorov, V. Shidlovski, S. Yakubovich, Ultrahigh resolution optical coherence tomography imaging with a broadband superluminescent diode light source. Opt. Express **12**, 2112–2119 (2004)
42. B.E. Bouma, G.J. Tearney, S.A. Boppart, M.R. Hee, M.E. Brezinski, J.G. Fujimoto, High-resolution optical coherence tomographic imaging using a mode-locked Ti: Al_2O_3 laser source. Opt. Lett. **20**, 1486–1488 (1995)
43. W. Drexler, U. Morgner, F.X. Kärtner, C. Pitris, S.A. Boppart, X.D. Li, E.P. Ippen, J.G. Fujimoto, In vivo ultrahigh-resolution optical coherence tomography. Opt. Lett. **24**, 1221–1223 (1999)
44. R. Leitgeb, W. Drexler, A. Unterhuber, B. Hermann, T. Bajraszewski, T. Le, A. Stingl, A. Fercher, Ultrahigh resolution Fourier domain optical coherence tomography. Opt. Express **12**, 2156–2165 (2004)
45. B. Považay, K. Bizheva, A. Unterhuber, B. Hermann, H. Sattmann, A.F. Fercher, W. Drexler, A. Apolonski, W.J. Wadsworth, J.C. Knight, P.S. Russell, M. Vetterlein, E. Scherzer, Submicrometer axial resolution optical coherence tomography. Opt. Lett. **27**, 1800–1802 (2002)
46. S. Kray, F. Spoler, M. Forst, H. Kurz, High-resolution simultaneous dual-band spectral domain optical coherence tomography. Opt. Lett. **34**, 1970–1972 (2009)
47. F. Spoler, S. Kray, P. Grychtol, B. Hermes, J. Bornemann, M. Forst, H. Kurz, Simultaneous dual-band ultra-high resolution optical coherence tomography. Opt. Express **15**, 10832–10841 (2007)
48. P. Cimalla, J. Walther, M. Mehner, M. Cuevas, E. Koch, Simultaneous dual-band optical coherence tomography in the spectral domain for high resolution in vivo imaging. Opt. Express **17**, 19486–19500 (2009)
49. Z.W. Zhi, J. Qin, L. An, R.K. Wang, Supercontinuum light source enables in vivo optical microangiography of capillary vessels within tissue beds. Opt. Lett. **36**, 3169–3171 (2011)
50. K. Takada, H. Yamada, M. Horiguchi, Optical low coherence reflectometer using [3 × 3] fiber coupler. IEEE Photonics Technol. Lett. **6**, 1014–1016 (1994)
51. R. Paschotta, J. Nilsson, A.C. Tropper, D.C. Hanna, Efficient superfluorescent light sources with broad bandwidth. IEEE J. Sel. Top. Quantum Electron. **3**, 1097–1099 (1997)
52. B.E. Bouma, L.E. Nelso, G.J. Tearney, D.J. Jones, M.E. Brezinski, J.G. Fujimoto, Optical coherence tomographic imaging of human tissue at 1.55 μm and 1.81 μm using Er- and Tm-doped fiber sources. J. Biomed. Opt. **3**, 76–79 (1998)
53. D.J. Derickson, P.A. Beck, T.L. Bagwell, D.M. Braun, J.E. Fouquet, F.G. Kellert, M.J. Ludowise, W.H. Perez, T.R. Ranganath, G.R. Trott, S.R. Sloan, High-power, low-internal-reflection, edge emitting light-emitting diodes. Hewlett-Packard J. **46**, 43–49 (1995)
54. H.H. Liu, P.H. Cheng, J.P. Wang, Spatially coherent white-light interferometer based on a point fluorescent source. Opt. Lett. **18**, 678–680 (1993)
55. C.F. Lin, B.L. Lee, Extremely broadband AlGaAs/GaAs superluminescent diodes. Appl. Phys. Lett. **71**, 1598–1600 (1997)
56. P.J. Poole, M. Davies, M. Dion, Y. Feng, S. Charbonneau, R.D. Goldberg, I.V. Mitchell, The fabrication of a broad-spectrum light-emitting diode using high-energy ion implantation. IEEE Photonics Technol. Lett. **8**, 1145–1147 (1996)
57. T.R. Cole, G.S. Kino, *Confocal Scanning Optical Microscopy and Related Imaging Systems* (Academic, San Diego, 1990)
58. J.M. Schmitt, A. Knüttel, M. Yadlowsky, M.A. Eckhaus, Optical coherence tomography of a dense tissue: statistics of attenuation and backscattering. Phys. Med. Biol. **39**, 1705–1720 (1994)

59. C.B. Su, Achieving variation of the optical path length by a few millimeters at millisecond rates for imaging of turbid media and optical interferometry: a new technique. Opt. Lett. **22**, 665–667 (1997)
60. G.J. Tearney, B.E. Bouma, J.G. Fujimoto, High speed phase and group-delay scanning with a grating-based phase control delay line. Opt. Lett. **22**, 1811–1813 (1997)
61. A.M. Rollins, M.D. Kulkarni, S. Yazdanfar, R. Ung-Arunyawee, J.A. Izatt, In vivo video rate optical coherence tomography. Opt. Express **3**, 219–229 (1998)
62. W. Drexler, O. Findl, R. Menapace, A. Kruger, A. Wedrich, G. Rainer, A. Baumgartner, C.K. Hitzenberger, A.F. Fercher, Dual beam optical coherence tomography: signal identification for ophthalmologic diagnosis. J. Biomed. Opt. **3**, 55–65 (1998)
63. J.A. Izatt, M.R. Hee, G.M. Owen, E.A. Swanson, J.G. Fujimoto, Optical coherence microscopy in scattering media. Opt. Lett. **19**, 590–592 (1994)
64. A.G. Podoleanu, Unbalanced versus balanced operation in an optical coherence tomography system. Appl. Opt. **39**, 173–182 (2000)
65. A.F. Fercher, C.K. Hitzenberger, G. Kamp, S.Y. El Zaiat, Measurement of intraocular distances by backscattering spectral interferometry. Opt. Commun. **117**, 43–8 (1995)
66. G. Häusler, M.W. Lindner, Coherence radar and spectral radar – new tools for dermatological diagnosis. J. Biomed. Opt. **3**, 21–31 (1998)
67. Y. Yasuno, Y. Sutoh, M. Nakama, S. Makita, M. Itoh, T. Yatagai, M. Mori, Spectral interferometric optical coherence tomography with nonlinear beta-barium borate time gating. Opt. Lett. **27**, 403–405 (2002)
68. E. Beaurepaire, A.C. Boccara, M. Lebec, L. Blanchot, H. Saint-Jalmes, Full-field optical coherence microscopy. Opt. Lett. **23**, 244–2466 (1998)
69. L. Vabre, A. Dubois, A.C. Boccara, Thermal-light full-field optical coherence tomography. Opt. Lett. **27**, 530–532 (2002)
70. C.E. Saxer, J.F. de Boer, B. Hyle Park, Y. Zhao, Z. Chen, J.S. Nelson, High-speed fiber-based polarization-sensitive optical coherence tomography of in vivo human skin. Opt. Lett. **25**, 1257–355 (2000)
71. J.E. Roth, J.A. Kozak, S. Yazdanfar, A.M. Rollins, J.A. Izatt, Simplified method for polarization-sensitive optical coherence tomography. Opt. Lett. **26**, 1069–1071 (2001)
72. S. Jiao, L.V. Wang, Two-dimensional depth-resolved Mueller matrix of biological tissue measured with double-beam polarization-sensitive optical coherence tomography. Opt. Lett. **27**, 101–103 (2002)
73. Z. Chen, T.E. Milner, D. Dave, J.S. Nelson, Optical Doppler tomographic imaging of fluid flow velocity in highly scattering media. Opt. Lett. **22**, 64–66 (1997)
74. J.A. Izatt, M.D. Kulkarni, S. Yazdanfar, J.K. Barton, A.J. Welch, In vivo bidirectional color Doppler flow imaging of picoliter blood volumes using optical coherence tomograghy. Opt. Lett. **22**, 1439–1441 (1997)
75. Y. Zhao, Z. Chen, C. Saxer, X. Shaohua, J.F. de Boer, J.S. Nelson, Phase-resolved optical coherence tomography and optical Doppler tomography for imaging blood flow in human skin with fast scanning speed and high velocity sensitivity. Opt. Lett. **25**, 114–116 (2000)
76. Y. Zhao, Z. Chen, Z. Ding, H. Ren, J.S. Nelson, Real-time phase-resolved functional optical coherence tomography by use of optical Hilbert transformation. Opt. Lett. **27**, 98–100 (2002)
77. S.G. Proskurin, Y. He, R.K. Wang, Determination of flow-velocity vector based on Doppler shift and spectrum broadening with optical coherence tomography. Opt. Lett. **28**, 1224–1226 (2003)
78. S.G. Proskurin, I.A. Sokolova, R.K. Wang, Imaging of non-parabolic velocity profiles in converging flow with optical coherence tomography. Phys. Med. Biol. **48**, 2907–2918 (2003)
79. U. Morgner, W. Drexler, F.X. Kartner, X.D. Li, C. Pitris, E.P. Ippen, J.G. Fujimoto, Spectroscopic optical coherence tomography. Opt. Lett. **25**, 111–113 (2000)
80. A.F. Fercher, W. Drexler, C.K. Hitzenberger, T. Lasser, Optical coherence tomography – principles and applications. Rep. Prog. Phys. **66**, 239–303 (2003)

81. P.H. Tomlins, R.K. Wang, Theory, development and applications of optical coherence tomography. J. Phys. D: Appl. Phys. **38**, 17 (2005)
82. W. Drexler, J.G. Fujimoto (eds.), *Optical Coherence Tomography: Technology and Applications* (Springer, Berlin, 2008)
83. C.K. Hitzenberger, P. Trost, P.W. Lo, Q.Y. Zhou, Three-dimensional imaging of the human retina by high-speed optical coherence tomography. Opt. Express **11**, 9 (2003)
84. A.F. Fercher, C.K. Hitzenberger, G. Kamp, S.Y. Elzaiat, Measurement of intraocular distances by backscattering spectral interferometry. Opt. Commun. **117**, 6 (1995)
85. S.R. Chinn, E.A. Swanson, J.G. Fujimoto, Optical coherence tomography using a frequency-tunable optical source. Opt. Lett. **22**, 3 (1997)
86. U. Haberland, P. Jansen, V. Blazek, H.J. Schmitt, Optical coherence tomography of scattering media using frequency-modulated continuous-wave techniques with tunable near-infrared laser. Proc. SPIE **2981**, 9 (1997)
87. J.F. de Boer, B. Cense, B.H. Park, M.C. Pierce, G.J. Tearney, B.E. Bouma, Improved signal-to-noise ratio in spectral-domain compared with time-domain optical coherence tomography. Opt. Lett. **28**, 3 (2003)
88. M. Choma, M. Sarunic, C. Yang, J. Izatt, Sensitivity advantage of swept source and Fourier domain optical coherence tomography. Opt. Express **11**, 6 (2003)
89. R. Leitgeb, C. Hitzenberger, A. Fercher, Performance of Fourier domain vs. time domain optical coherence tomography. Opt. Express **11**, 6 (2003)
90. M. Wojtkowski, R. Leitgeb, A. Kowalczyk, T. Bajraszewski, A.F. Fercher, In vivo human retinal imaging by Fourier domain optical coherence tomography. J. Biomed. Opt. **7**, 7 (2002)
91. B. Cense, N. Nassif, T. Chen, M. Pierce, S.-H. Yun, B. Park, B. Bouma, G. Tearney, J. de Boer, Ultrahigh-resolution high-speed retinal imaging using spectral-domain optical coherence tomography. Opt. Express **12**, 13 (2004)
92. D.M. de Bruin, D. Burnes, J. Loewenstein, Y. Chen, S. Chang, T. Chen, D. Esmaili, J.F. de Boer, In vivo three-dimensional imaging of neovascular age related macular degeneration using optical frequency domain imaging at 1050 nm. Invest. Ophthalmol. Vis. Sci. **49**(10), 4545–4552 (2008)
93. E.C. Lee, J.F. de Boer, M. Mujat, H. Lim, S.H. Yun, In vivo optical frequency domain imaging of human retina and choroid. Opt. Express **14**, 9 (2006)
94. H. Lim, M. Mujat, C. Kerbage, E.C. Lee, Y. Chen, T.C. Chen, J.F. de Boer, High-speed imaging of human retina in vivo with swept-source optical coherence tomography. Opt. Express **14**, 7 (2006)
95. M. Wojtkowski, V. Srinivasan, T. Ko, J. Fujimoto, A. Kowalczyk, J. Duker, Ultrahigh-resolution, high-speed, Fourier domain optical coherence tomography and methods for dispersion compensation. Opt. Express **12**, 19 (2004)
96. R. Leitgeb, W. Drexler, A. Unterhuber, B. Hermann, T. Bajraszewski, T. Le, A. Stingl, A. Fercher, Ultrahigh resolution Fourier domain optical coherence tomography. Opt. Express **12**, 10 (2004)
97. V.J. Srinivasan, R. Huber, I. Gorczynska, J.G. Fujimoto, J.Y. Jiang, P. Reisen, A.E. Cable, High-speed, high-resolution optical coherence tomography retinal imaging with a frequency-swept laser at 850 nm. Opt. Lett. **32**, 3 (2007)
98. A.H. Bachmann, M.L. Villiger, C. Blatter, T. Lasser, R.A. Leitgeb, Resonant Doppler flow imaging and optical vivisection of retinal blood vessels. Opt. Express **15**, 15 (2007)
99. L. An, R.K. Wang, In vivo volumetric imaging of vascular perfusion within human retina and choroids with optical micro-angiography. Opt. Express **16**, 15 (2008)
100. B.J. Vakoc, R.M. Lanning, J.A. Tyrrell, T.P. Padera, L.A. Bartlett, T. Stylianopoulos, L.L. Munn, G.J. Tearney, D. Fukumura, R.K. Jain, B.E. Bouma, Three-dimensional microscopy of the tumor microenvironment in vivo using optical frequency domain imaging. Nat. Med. **15**, 8 (2009)

101. B.R. White, M.C. Pierce, N. Nassif, B. Cense, B.H. Park, G.J. Tearney, B.E. Bouma, T.C. Chen, J.F. de Boer, In vivo dynamic human retinal blood flow imaging using ultra-high-speed spectral domain optical coherence tomography. Opt. Express **11**, 8 (2003)
102. J. Fingler, R.J. Zawadzki, J.S. Werner, D. Schwartz, S.E. Fraser, Volumetric microvascular imaging of human retina using optical coherence tomography with a novel motion contrast technique. Opt. Express **17**, 11 (2009)
103. L. An, H.M. Subhush, D.J. Wilson, R.K. Wang, High-resolution wide-field imaging of retinal and choroidal blood perfusion with optical microangiography. J. Biomed. Opt. **15**, 066022 (2010)
104. L. Yu, Z. Chen, Doppler variance imaging for three-dimensional retina and choroid angiography. J. Biomed. Opt. **15**, 016029 (2010)
105. M. Szkulmowski, A. Szkulmowska, T. Bajraszewski, A. Kowalczyk, M. Wojtkowski, Flow velocity estimation using joint spectral and time domain optical coherence tomography. Opt. Express **16**, 18 (2008)
106. R.K. Wang, L. An, S. Saunders, D.J. Wilson, Optical microangiography provides depth-resolved images of directional ocular blood perfusion in posterior eye segment. J. Biomed. Opt. **15**, 020502 (2010)
107. S. Makita, F. Jaillon, M. Yamanari, M. Miura, Y. Yasuno, Comprehensive in vivo micro-vascular imaging of human eye by dual-beam-scan Doppler optical coherence angiography. Opt. Express **19**, 13 (2011)
108. S. Makita, Y. Hong, M. Yamanari, T. Yatagai, Y. Yasuno, Optical coherence angiography. Opt. Express **14**, 20 (2006)
109. S. Zotter, M. Pircher, T. Torzicky, M. Bonesi, E. Götzinger, R.A. Leitgeb, C.K. Hitzenberger, Visualization of microvasculature by dual-beam phase-resolved Doppler optical coherence tomography. Opt. Express **19**, 11 (2011)
110. Y.K. Tao, K.M. Kennedy, J.A. Izatt, Velocity-resolved 3D retinal microvessel imaging using single-pass flow imaging spectral domain optical coherence tomography. Opt. Express **17**, 12 (2009)
111. B. Potsaid, B. Baumann, D. Huang, S. Barry, A.E. Cable, J.S. Schuman, J.S. Duker, J.G. Fujimoto, Ultrahigh speed 1050 nm swept source/Fourier domain OCT retinal and anterior segment imaging at 100,000 to 400,000 axial scans per second. Opt. Express **18**, 20 (2010)
112. C.M. Eigenwillig, T. Klein, W. Wieser, B.R. Biedermann, R. Huber, Wavelength swept amplified spontaneous emission source for high speed retinal optical coherence tomography at 1060 nm. J. Biophotonics **4**(7–8), 552–558 (2010)
113. M. Gora, K. Karnowski, M. Szkulmowski, B.J. Kaluzny, R. Huber, A. Kowalczyk, M. Wojtkowski, Ultrahigh-speed swept source OCT imaging of the anterior segment of human eye at 200 kHz with adjustable imaging range. Opt. Express **17**, 15 (2009)
114. V.J. Srinivasan, D.C. Adler, Y. Chen, I. Gorczynska, R. Huber, J. Duker, J.S. Schuman, J.G. Fujimoto, Ultrahigh-speed optical coherence tomography for three-dimensional and *en face* imaging of the retina and optic nerve head. Invest. Ophthalmol. Vis. Sci. **49**(11), 5103–5110 (2008)
115. B. Potsaid, I. Gorczynska, V.J. Srinivasan, Y.L. Chen, J. Jiang, A. Cable, J.G. Fujimoto, Ultrahigh speed spectral/Fourier domain OCT ophthalmic imaging at 70,000 to 312,500 axial scans per second. Opt. Express **16**, 21 (2008)
116. D.Y. Kim, J. Fingler, J.S. Werner, D.M. Schwartz, S.E. Fraser, R.J. Zawadzki, In vivo volumetric imaging of human retinal circulation with phase-variance optical coherence tomography. Biomed. Opt. Express **2**, 10 (2011)
117. R.K. Wang, L. An, P. Francis, D.J. Wilson, Depth-resolved imaging of capillary networks in retina and choroid using ultrahigh sensitive optical microangiography. Opt. Lett. **35**, 3 (2010)
118. W. Wieser, B.R. Biedermann, T. Klein, C.M. Eigenwillig, R. Huber, Multi-megahertz OCT: high quality 3D imaging at 20 million A-scans and 4.5 GVoxels per second. Opt. Express **18**, 20 (2010)

119. T. Klein, W. Wieser, C.M. Eigenwillig, B.R. Biedermann, R. Huber, Megahertz OCT for ultrawide-field retinal imaging with a 1050 nm Fourier domain mode-locked laser. Opt. Express **19**, 19 (2011)
120. M.R. Hee, J.A. Izatt, E.A. Swanson, D. Huang, J.S. Schuman, C.P. Lin, C.A. Puliafito, J.G. Fujimoto, Optical coherence tomography of the human retina. Arch. Opthalmol. **113**, 325–332 (1995)
121. C.A. Puliafito, M.R. Hee, C.P. Lin, E. Reichel, J.S. Schuman, J.S. Duker, J.A. Izatt, E.A. Swanson, J.G. Fujimoto, Imaging of macular diseases with optical coherence tomography. Ophthalmology **120**, 217–229 (1995)
122. C.A. Puliafito, M.R. Hee, J.S. Schumann, J.G. Fujimoto, *Optical Coherence Tomography of Ocular Diseases* (Slack, Thorofare, 1995)
123. M.E. Brezinski, G.J. Tearney, B.E. Bouma, J.A. Izatt, M.R. Hee, E.A. Swanson, J.F. Southern, J.G. Fujimoto, Optical coherence tomography for optical biopsy: properties and demonstration of vascular pathology. Circulation **93**, 1206–1213 (1996)
124. V.V. Tuchin, X. Xu, R.K. Wang, Dynamic optical coherence tomography in optical clearing, sedimentation and aggregation study of immersed blood. Appl. Opt. **41**, 258–271 (2002)
125. P. Parsa, S. Jacques, N. Nishioka, Optical properties of rat liver between 350 and 2200 nm. Appl. Opt. **28**, 2325–2330 (1989)
126. R.K. Wang, Signal degradation by multiple scattering in optical coherence tomography of dense tissue: a Monte Carlo study towards optical clearing of biotissues. Phys. Med. Biol. **47**, 2281–2299 (2002)
127. D. Huang, J. Wang, C.P. Lin, C.A. Puliafito, J.G. Fujimoto, Micron-resolution ranging of cornea anterior chamber by optical reflectometry. Lasers Surg. Med. **11**, 419–425 (1991)
128. A.F. Fercher, C.K. Hitzenberger, G. Kemp, S.Y. Elzaiat, Measurement of intraocular distances by backscattering spectral interferometry. Opt. Commun. **117**, 43–48 (1995)
129. K. Rohrschneider, R.O. Burk, F.E. Kruse, H.E. Volcker, Reproducibility of the optic nerve head topography with a new laser tomographic scanning device. Ophthalmol. **101**, 1044–1049 (1994)
130. M.R. Hee, C.A. Puliafitom, C. Wong, E. Reichel, J.S. Duker, J.S. Schuman, E.A. Swanson, J.G. Fujimoto, Optical coherence tomography of central serous chorioretinopathy. Am. J. Ophthalmol. **120**, 65–74 (1995)
131. M.R. Hee, C.A. Puliafito, C. Wong, E. Reichel, J.S. Duker, J.S. Schuman, E.A. Swanson, J.G. Fujimoto, Optical coherence tomography of macular holes. Ophthalmol. **102**, 748–756 (1995)
132. J.S. Schuman, M.R. Hee, C.A. Puliafito, C. Wong, T. Pedutkloizman, C.P. Lin, E. Hertzmark, J.A. Izatt, E.A. Swanson, J.G. Fujimoto, Quantification of nerve fibre layer thickness in normal and glaucomatous eyes using optical coherence tomography. Arch. Ophthalmol. **113**, 586–596 (1995)
133. W. Drexler, U. Morgner, R.K. Ghanta, F.X. Kartner, J.S. Schuman, J.G. Fujimoto, Ultrahigh-resolution ophthalmic optical coherence tomography. Nat. Med. **7**, 502–507 (2001)
134. I. Hartl, T. Ko, R.K. Ghanta, W. Drexler, A. Clermont, S.E. Bursell, J.G. Fujimoto, In vivo ultrahigh resolution optical coherence tomography for the quantification of retinal structure in normal and transgenic mice. Invest. Ophthalmol. Vis. Sci. **42**(Suppl. 4), 4252 (2001)
135. B.E. Bouma, G.J. Tearney (eds.), *Handbook of Optical Coherence Tomography* (Marcel-Dekker, New York, 2002)
136. S.A. Boppart, B.E. Bouma, M.E. Brezinski, G.J. Tearney, J.G. Fujimoto, Imaging developing neural morphology using optical coherence tomography. J. Neurosci. Methods **70**, 65–72 (1996)
137. S.A. Boppart, G.J. Tearney, B.E. Bouma, J.F. Southern, M.E. Brezinski, J.G. Fujimoto, Noninvasive assessment of the developing *Xenopus* cardiovascular system using optical coherence tomography. Proc. Natl. Acad. Sci. U.S.A. **94**, 4256–4261 (1997)
138. S. Rugonyi, C. Shaut, A.P. Liu, K. Thornburg, R.K. Wang, Changes in wall motion and blood flow in the outflow tract of chick embryonic hearts observed with optical coherence tomography after outflow tract banding and vitelline-vein ligation. Phys. Med. Biol. **53**, 5077–5091 (2008)

139. A. Liu, R.K. Wang, K.L. Thornburg, S. Rugonyi, Dynamic variation of hemodynamic shear stress on the walls of developing chick hearts: computational models of the heart outflow tract. Eng. Comput. **25**, 73–86 (2009)
140. A. Liu, R.K. Wang, K.L. Thornburg, S. Rugonyi, Efficient post-acquisition synchronization of 4D non-gated cardiac images obtained from optical coherence tomography: application to 4D reconstruction of the chick embryonic heart. J. Biomed. Opt. **14**(4), 044020 (2009)
141. Z. Ma, A. Liu, X. Yin, A. Troyer, K. Thornburg, R.K. Wang, S. Rugonyi, Measurement of absolute blood flow velocity across outflow tract of HH18 chicken embryo based on 4D reconstruction using spectral domain optical coherence tomography. Biomed. Opt. Express **1**(3), 798–811 (2010)
142. I.V. Larina, K. Furushima, M.E. Dickinson, R.R. Behringer, K.V. Larin, Live imaging of rat embryos with Doppler swept-source optical coherence tomography. J. Biomed. Opt. **14**, 050506-1–050506-3 (2009)
143. K.V. Larin, I.V. Larina, M. Liebling, M.E. Dickinson, Live imaging of early developmental processes in mammalian embryos with optical coherence tomography. J. Innov. Opt. Health Sci. **2**, 253–259 (2009)
144. N.D. Gladkova, G.A. Petrova, N.K. Nikulin, S.G. Radenska-Lopovok, L.B. Snopova, Y.P. Chumakov, V.A. Nasonova, V.M. Gelikonov, G.V. Gelikonov, R.V. Kuranov, A.M. Sergeev, F.I. Feldchtein, In vivo optical coherence tomography imaging of human skin: norm and pathology. Skin Res. Technol. **6**, 6–16 (2000)
145. J. Welzel, Optical coherence tomography in dermatology: a review. Skin Res. Technol. **7**, 1–9 (2001)
146. C.B. Williams, J.E. Whiteway, J.R. Jass, Practical aspects of endoscopic management of malignant polyps. Endoscopy **19**(Suppl. 1), 31–37 (1987)
147. K. Kobayashi, H.S. Wang, M.V. Sivak, J.A. Izatt, Micron-resolution sub-surface imaging of the gastrointestinal tract wall with optical coherence tomography. Gastrointest. Endosc. **43**, 29–29 (1996)
148. J.A. Izatt, Micron scale in vivo imaging of gastrointestinal cancer using optical coherence tomography. Radiology **217**(Suppl. S), 385 (2000)
149. A. Das, M.V. Sivak, A. Chak, R.C.K. Wong, V. Westphal, A.M. Rollins, J. Willis, G. Isenberg, J.A. Izatt, High-resolution endoscopic imaging of the GI tract: a comparative study of optical coherence tomography versus high-frequency catheter probe EUS. Gastrointest. Endosc. **54**, 219–224 (2001)
150. J.G. Fujimoto, M.E. Brezinski, G.J. Tearney, S.A. Boppart, B.E. Bouma, M.R. Hee, J.F. Southern, E.A. Swanson, Optical biopsy and imaging using optical coherence tomography. Nature Med. **1**, 970–972 (1995)
151. M.E. Brezinski, G.J. Tearney, N.J. Weissman, S.A. Boppart, B.E. Bouma, M.R. Hee, A.E. Weyman, E.A. Swanson, J.F. Southern, J.G. Fujimoto, Assessing atherosclerotic plaque morphology: comparison of optical coherence tomography and high frequency intravascular ultrasound. Heart **77**, 397–403 (1997)
152. J.G. Fujimoto, S.A. Boppart, G.J. Tearney, B.E. Bouma, C. Pitris, M.E. Brezinski, High resolution in vivo intra-arterial imaging with optical coherence tomography. Heart **82**, 128–133 (1999)
153. B.W. Colston, U.S. Sathyam, L.B. DaSilva, M.J. Everett, P. Stroeve, L.L. Otis, Dental OCT. Opt. Express **3**, 230–238 (1998)
154. Y. Yang, L. Wu, Y. Feng, R.K. Wang, Observations of birefringence in tissues from optic-fibre based optical coherence tomography. Meas. Sci. Technol. **14**, 41–46 (2003)
155. A. Baumgartner, C.K. Hitzenberger, H. Sattmann, W. Drexler, A.F. Fercher, Signal and resolution enhancements in dual beam optical coherence tomography of the human eye. J. Biomed. Opt. **3**, 45–54 (1998)
156. G. Yao, L.V. Wang, Two-dimensional depth-resolved Mueller matrix characterization of biological tissue by optical coherence tomography. Opt. Lett. **24**, 537–539 (1999)

157. J.P. Dunkers, R.S. Parnas, C.G. Zimba, R.C. Peterson, K.M. Flynn, J.G. Fujimoto, B.E. Bouma, Optical coherence tomography of glass reinforced polymer composites. Composites **30A**, 139–145 (1999)
158. M. Bashkansky, D. Lewis III, V. Pujari, J. Reintjes, H.Y. Yu, Subsurface detection and characterization of Hertzian cracks in Si_3N_4 balls using optical coherence tomography. NDT E-Int. **34**, 547–555 (2001)
159. F. Xu, H.E. Pudavar, P.N. Prasad, Confocal enhanced optical coherence tomography for nondestructive evaluation of paints and coatings. Opt. Lett. **24**, 1808–1810 (1999)
160. R.K. Wang, J.B. Elder, Optical coherence tomography: a new approach to medical imaging with resolution at cellular level. Proc. MBNT 1–4, ISSBN: 0951584235 (1999)
161. D.J. Smithies, T. Lindmo, Z. Chen, J.S. Nelson, T. Miller, Signal attenuation and localisation in optical coherence tomography by Monte Carlo simulation. Phys. Med. Biol. **43**, 3025–3044 (1998)
162. G. Yao, L.V. Wang, Monte Carlo simulation of an optical coherence tomography signal in homogeneous turbid media. Phys. Med. Biol. **44**, 2307–2320 (1999)
163. J.M. Schmitt, A. Knüttle, M.J. Yadlowsky, M.A. Eckhaus, Optical coherence tomography of a dense tissue: statistics of attenuation and backscattering. Phys. Med. Biol. **39**, 1705–1720 (1994)
164. X. Xu, R.K. Wang, J.B. Elder, V.V. Tuchin, Effect on dextran-induced changes in refractive index and aggregation on optical properties of whole blood. Phys. Med. Biol. **48**, 1205–1221 (2003)
165. J.M. Schmitt, A. Knüttel, Model of optical coherence tomography of heterogeneous tissue. J. Opt. Soc. Am. A **14**, 1231–1242 (1997)
166. L. Thrane, H.T. Yura, P.E. Andersen, Analysis of optical coherence tomography systems based on the extended Huygens-Fresenel principle. J. Opt. Soc. Am. A **17**, 484–490 (2000)
167. Y. Feng, R.K. Wang, J.B. Elder, A theoretical model of optical coherence tomography for system optimization and characterization. J. Opt. Soc. Am. A **20**, 1792–1803 (2003)
168. V.V. Tuchin, *Tissue Optics: Light Scattering Methods and Instruments for Medical Diagnosis*, vol. PM 166, 2nd edn. (SPIE Press, Bellingham, 2007)
169. V.V. Tuchin, Light scattering study of tissue. Phys. Usp. **40**, 495–515 (1997)
170. V.V. Tuchin, I.L. Maksimova, D.A. Zimnyakov, I.L. Kon, A.H. Mavlutov, A.A. Mishin, Light propagation in tissues with controlled optical properties. J. Biomed. Opt. **2**, 401–417 (1997)
171. V.V. Tuchin, Coherent optical techniques for the analysis of tissue structure and dynamics. J. Biomed. Opt. **4**, 106–124 (1999)
172. V.V. Tuchin (ed.), *Handbook of Optical Biomedical Diagnostics*, vol. PM107 (SPIE Press, Bellingham, 2002)
173. B. Beauvoit, T. Kitai, B. Chance, Contribution of the mitochondrial compartment to the optical properties of rat liver: a theoretical and practical approach. Biophys. J. **67**, 2501–2510 (1994)
174. J.T. Bruulsema, J.E. Hayward, T.J. Farrell, M.S. Patterson, L. Heinemann, M. Berger, T. Koschinsky, J. Sandahl-Christiansen, H. Orskov, M. Essenpreis, G. Schmelzeisen-Redeker, D. Böcker, Correlation between blood glucose concentration in diabetics and noninvasively measured tissue optical scattering coefficient. Opt. Lett. **22**(3), 190–192 (1997)
175. E.K. Chan, B. Sorg, D. Protsenko, M. O'Neil, M. Motamedi, A.J. Welch, Effects of compression on soft tissue optical properties. IEEE J. Sel. Top. Quantum Electron. **2**, 943–950 (1996)
176. B. Chance, H. Liu, T. Kitai, Y. Zhang, Effects of solutes on optical properties of biological materials: models, cells, and tissues. Anal. Biochem. **227**, 351–362 (1995)
177. I.F. Cilesiz, A.J. Welch, Light dosimetry: effects of dehydration and thermal damage on the optical properties of the human aorta. Appl. Opt. **32**, 477–487 (1993)
178. M. Kohl, M. Esseupreis, M. Cope, The influence of glucose concentration upon the transport of light in tissue-simulating phantoms. Phys. Med. Biol. **40**, 1267–1287 (1995)

179. H. Liu, B. Beauvoit, M. Kimura, B. Chance, Dependence of tissue optical properties on solute-induced changes in refractive index and osmolarity. J. Biomed. Opt. **1**, 200–211 (1996)
180. J.S. Maier, S.A. Walker, S. Fantini, M.A. Franceschini, E. Gratton, Possible correlation between blood glucose concentration and the reduced scattering coefficient of tissues in the near infrared. Opt. Lett. **19**, 2062–2064 (1994)
181. X. Xu, R.K. Wang, A. El Haj, Investigation of changes in optical attenuation of bone and neuronal cells in organ culture or 3 dimensional constructs in vitro with optical coherence tomography: relevance to cytochrome-oxidase monitoring. Eur. Biophys. J. **32**, 355–362 (2003)
182. V.V. Tuchin, A.N. Bashkatov, E.A. Genina, Y.P. Sinichkin, N.A. Lakodina, In vivo investigation of the immersion-liquid-induced human skin clearing dynamics. Tech. Phys. Lett. **27**, 489–490 (2001)
183. G. Vargas, E.K. Chan, J.K. Barton, H.G. Rylander III, A.J. Welch, Use of an agent to reduce scattering in skin. Lasers Surg. Med. **24**, 133–141 (1999)
184. R.K. Wang, X. Xu, V.V. Tuchin, J.B. Elder, Concurrent enhancement of imaging depth and contrast for optical coherence tomography by hyperosmotic agents. J. Opt. Soc. Am. **B18**, 948–953 (2001)
185. M. Brezinski, K. Saunders, C. Jesser, X. Li, J. Fujimoto, Index matching to improve OCT imaging through blood. Circulation **103**, 1999–2003 (2001)
186. G. Vargas, K.F. Chan, S.L. Thomsen, A.J. Welch, Use of osmotically active agents to alter optical properties of tissue: effects on the detected fluorescence signal measured through skin. Lasers Surg. Med. **29**, 213–220 (2001)
187. R.K. Wang, V.V. Tuchin, Enhance light penetration in tissue for high resolution optical imaging techniques by use of biocompatible chemical agents. J. X-Ray Sci. Technol. **10**, 167–176 (2002)
188. Y. He, R.K. Wang, Dynamic optical clearing effect of tissue impregnated by hyperosmotic agents: studied with optical coherence tomography. J. Biomed. Opt. **9**, 200–206 (2004)
189. R.K. Wang, X. Xu, Y. He, J.B. Elder, Investigation of optical clearing of gastric tissue immersed with the hyperosmotic agents. IEEE J. Sel. Top. Quantum Electron. **9**, 234–242 (2003)
190. X. Xu, R.K. Wang, The role of water desorption on optical clearing of biotissue: studied with near infrared reflectance spectroscopy. Med. Phys. **30**, 1246–1253 (2003)
191. X. Xu, R.K. Wang, J.B. Elder, Optical clearing effect on gastric tissues immersed with biocompatible chemical agents studied by near infrared reflectance spectroscopy. J. Phys. D: Appl. Phys. **36**, 1707–1713 (2003)
192. A.N. Bashkatov, E.A. Genina, Y.P. Sinichkin, V.I. Kochubey, N.A. Lakodina, V.V. Tuchin, Determination of diffusion coefficients of glucose in the human eye sclera. Biophysics **48**(3), 309–313 (2003)
193. J.M. Schmitt, G. Kumar, Optical scattering properties of soft tissue: a discrete particle model. Appl. Opt. **37**, 2788–2797 (1998)
194. R.K. Wang, Modeling optical properties of soft tissue by fractal distribution of scatters. J. Mod. Opt. **47**, 103–120 (2000)
195. A. Dunn, R. Richards-Kortum, Three-dimensional computation of light scattering from cells. IEEE J. Sel. Top. Quantum Electron. **2**, 898–905 (1996)
196. S.L. Jacques, Origins of tissue optical properties in the UVA, visible, and NIR regions, in *Selected Papers on Tissue Optics: Applications in Medical Diagnostics and Therapy*, ed. by V.V. Tuchin. SPIE Milestone Series, vol. MS 102 (SPIE Press, Bellingham, 1994), pp. 364–371
197. V. Twersky, Transparency of pair-correlated, random distributions of small scatters, with applications to the cornea. J. Opt. Soc. Am. **65**, 524–530 (1975)
198. R. Barer, K.F. Ross, S. Tkaczyk, Refractometry of living cells. Nature **171**, 720–724 (1953)
199. P. Brunsting, P. Mullaney, Differential light scattering from spherical mammalian cells. Biophys. J. **14**, 439–453 (1974)

200. C.F. Bohren, D.R. Huffman, *Absorption and Scattering of Light by Small Particles* (Wiley, New York, 1983)
201. R. Graaff, J.G. Aarnoudse, J.R. Zijp, P.M.A. Sloot, F.F. de Mul, J. Greve, M.H. Koelink, Reduced light scattering properties for mixtures of the optical properties: a simple approximation derived from Mie calculation. Appl. Opt. **31**, 1370–1376 (1992)
202. J. Firm, P. Mazur, Interactions of cooling rate, warming rate, glycerol concentration and dilution procedure on the viability of frozen-thawed human granulocytes. Cryobiology **20**, 657–676 (1983)
203. N. Songsasen, B.C. Bucknell, C. Plante, S.P. Leibo, In vitro and in vivo survival of cryopreserved sheep embryos. Cryobiology **32**, 78–91 (1995)
204. D. Martin, H. Hauthal, *Dimethyl Sulphoxide* (Wiley, New York, 1975)
205. W.M. Bourne, D.R. Shearer, L.R. Nelson, Human corneal endothelial tolerance to glycerol, dimethysulphoxide, 1,2-propanediol, and 2,3-butanediol. Cryobiology **31**, 1–9 (1994)
206. J.O.M. Karlsson, M. Toner, Long term storage of tissue by cryopreservation: critical issues. Biomaterials **17**, 243–256 (1996)
207. K.H. Kolb, G. Janicke, M. Kramer, P.E. Schulze, G. Raspe, Absorption, distribution and elimination of labeled dimethyl sulfoxide in man and animals. Ann. N. Y. Acad. Sci. **141**, 85–95 (1967)
208. R. Herschler, S.W. Jacob, The case of dimethyl sulfoxide, in *Controversies in Therapeutics*, ed. by L. Lasagna (W.B. Saunders, Philadelphia, 1980)
209. A. Walter, J. Gutknecht, Permeability of small nonelectrolytes through lipid bilayer membranes. J. Membr. Biol. **90**, 207–217 (1986)
210. P. Patwari, N.J. Weissman, S.A. Boppart, C.A. Jesser, D. Stamper, J.G. Fujimoto, M.E. Brezinski, Assessment of coronary plaque with optical coherence tomography and high frequency ultrasound. Am. J. Cardiol. **85**, 641–644 (2000)
211. A. Roggan, M. Friebel, K. Dorschel, A. Hahn, G. Mueller, Optical properties of circulating human blood in the wavelength range 400-2500 nm. J. Biomed. Opt. **4**, 36–46 (1999)
212. S.Y. Shchyogolev, Inverse problems of spectroturbidimetry of biological disperse systems: an overview. J. Biomed. Opt. **4**, 490–503 (1999)
213. A.V. Priezzhev, O.M. Ryaboshapka, N.N. Firsov, I.V. Sirko, Aggregation and disaggregation of erythrocytes in whole blood: study by backscattering technique. J. Biomed. Opt. **4**, 76–84 (1999)
214. S.M. Bertoluzzo, A. Bollini, M. Rsia, A. Raynal, Kinetic model for erythrocyte aggregation. Blood Cells Mol. Dis. **25**(22), 339–349 (1999)
215. D. Levitz, L. Thrane, M.H. Frosz, P.E. Andersen, C.B. Andersen, S. Andersson-Engels, J. Valanciunaite, J. Swartling, P.R. Hansen, Determination of optical scattering properties of highly-scattering media in optical coherence tomography images. Opt. Express **12**, 249–259 (2004)
216. Y. Yang, T. Wang, N.C. Biswal, X. Wang, M. Sanders, M. Brewer, Q. Zhu, Optical scattering coefficient estimated by optical coherence tomography correlates with collagen content in ovarian tissue. J. Biomed. Opt. **16**(9), 090504-1–090504-3 (2011)
217. V.M. Kodach, D.J. Faber, J. van Marle, T.G. van Leeuwen, J. Kalkman, Determination of the scattering anisotropy with optical coherence tomography. Opt. Express **19**(7), 6131–6140 (2011)
218. D.M. Zhestkov, A.N. Bashkatov, E.A. Genina, V.V. Tuchin, Influence of clearing solutions osmolarity on the optical properties of RBC. Proc. SPIE **5474**, 321–330 (2004)
219. A.N. Bashkatov, D.M. Zhestkov, E.A. Genina, V.V. Tuchin, Immersion optical clearing of human blood in the visible and near infrared spectral range. Opt. Spectrosc. **98**(4), 638–646 (2005)
220. A.G. Borovoi, E.I. Naats, U.G. Oppel, Scattering of light by a red blood cell. J. Biomed. Opt. **3**(3), 364–372 (1998)
221. M. Hammer, D. Schweitzer, B. Michel, E. Thamm, A. Kolb, Single scattering by red blood cells. Appl. Opt. **37**(31), 7410–7418 (1998)

222. J.M. Steinke, A.P. Shephard, Diffusion model of the optical absorbance of whole blood. J. Opt. Soc. Am. A **5**, 813–822 (1988)
223. A. Ishimaru, *Wave Propagation and Scattering in Random Media* (IEEE Press, New York, 1997)
224. V.V. Tuchin, *Optical Clearing of Tissues and Blood*, vol. PM 154 (SPIE Press, Bellingham, 2006)
225. A.H. Hielsher, J.R. Mourant, I.J. Bigio, Influence of particle size and concentration on the diffuse backscattering of polarized light from tissue phantoms and biological cell suspensions. Appl. Opt. **36**, 125–135 (1997)
226. V. Shankaran, J.T. Walsh Jr., D.J. Maitland, Comparative study of polarized light propagation in biological tissues. J. Biomed. Opt. **7**(3), 300–306 (2002)
227. V.V. Tuchin, X. Xu, R.K. Wang, Sedimentation of immersed blood studied by OCT. Proc. SPIE **4241**, 357–369 (2001)
228. V.V. Tuchin, D.M. Zhestkov, A.N. Bashkatov, E.A. Genina, Theoretical study of immersion optical clearing of blood in vessels at local hemolysis. Opt. Express **12**, 2966–2971 (2004)
229. G. Popescu, T. Ikeda, C.A. Best, K. Badizadegan, R.R. Dasari, M.S. Feld, Erythrocyte structure and dynamics quantified by Hilbert phase microscopy. J. Biomed. Opt. **10**(6), 060503-1–060503-3 (2005)
230. H. Kataiwa, A. Tanaka, H. Kitabata, T. Imanishi, T. Akasaka, Safety and usefulness of non-occlusion image acquisition technique for optical coherence tomography. Circ. J. **72**, 1536–1537 (2008)
231. Y. Ozaki, H. Kitabata, H. Tsujioka, S. Hosokawa, M. Kashiwagi, K. Ishibashi, K. Komukai, T. Tanimoto, Y. Ino, S. Takarada, T. Kubo, K. Kimura, A. Tanaka, K. Hirata, M. Mizukoshi, T. Imanishi, T. Akasaka, Comparison of contrast media and low-molecular-weight dextran for frequency-domain optical coherence tomography. Circ. J. **76** (2012). doi:10.1253/circj.CJ-11-1122 released online Feb. 3, 2012
232. M. Ghosn, V.V. Tuchin, K.V. Larin, Depth-resolved monitoring of glucose diffusion in tissues by using optical coherence tomography. Opt. Lett. **31**, 2314–2316 (2006)
233. M.G. Ghosn, V.V. Tuchin, K.V. Larin, Nondestructive quantification of analyte diffusion in cornea and sclera using optical coherence tomography. Invest. Ophthalmol. Vis. Sci. **48**, 2726–2733 (2007)
234. M.G. Ghosn, E.F. Carbajal, N. Befrui, V.V. Tuchin, K.V. Larin, Differential permeability rate and percent clearing of glucose in different regions in rabbit sclera. J. Biomed. Opt. **13**, 021110-1–021110-6 (2008)
235. K.V. Larin, V.V. Tuchin, Functional imaging and assessment of the glucose diffusion rate in epithelial tissues with optical coherence tomography. Quantum Electron. **38**, 551–556 (2008)
236. K.V. Larin, M.G. Ghosn, A.N. Bashkatov, E.A. Genina, N.A. Trunina, V.V. Tuchin, Optical clearing for OCT image enhancement and in-depth monitoring of molecular diffusion. IEEE J. Sel. Top. Quantum Electron. **18**(3), 1244–1259 (2012)
237. I.V. Larina, E.F. Carbajal, V.V. Tuchin, M.E. Dickinson, K.V. Larin, Enhanced OCT imaging of embryonic tissue with optical clearing. Laser Phys. Lett. **5**, 476–480 (2008)
238. N. Sudheendran, M. Mohamed, M. Ghosn, V.V. Tuchin, K.V. Larin, Assessment of tissue optical clearing as a function of glucose concentration using optical coherence tomography. J. Innov. Opt. Health Sci. **3**, 169–176 (2010)
239. K.V. Larin, T. Akkin, R.O. Esenaliev, M. Motamedi, T.E. Milner, Phase-sensitive optical low-coherence reflectometry for the detection of analyte concentrations. Appl. Opt. **43**, 3408–3414 (2004)
240. K.V. Larin, M. Motamedi, T.V. Ashitkov, R.O. Esenaliev, Specificity of noninvasive blood glucose sensing using optical coherence tomography technique: a pilot study. Phys. Med. Biol. **48**, 1371–1390 (2003)

241. A.I. Kholodnykh, I.Y. Petrova, K.V. Larin, M. Motamedi, R.O. Esenaliev, Precision of measurement of tissue optical properties with optical coherence tomography. Appl. Opt. **42**, 3027–3037 (2003)
242. K.V. Larin, M.S. Eledrisi, M. Motamedi, R.O. Esenaliev, Noninvasive blood glucose monitoring with optical coherence tomography – a pilot study in human subjects. Diabetes Care **25**, 2263–2267 (2002)
243. G. Vargas, A. Readinger, S.S. Dozier, A.J. Welch, Morphological changes in blood vessels produced by hyperosmotic agents and measured by optical coherence tomography. Photochem. Photobiol. **77**, 541–549 (2003)
244. A.T. Yeh, J. Hirshburg, Molecular interactions of exogenous chemical agents with collagen – implications for tissue optical clearing. J. Biomed. Opt. **11**, 014003 (2006)
245. R.O. Esenaliev, K.V. Larin, I.V. Larina, M. Motamedi, Noninvasive monitoring of glucose concentration with optical coherence tomography. Opt. Lett. **26**, 992–994 (2001)
246. M. Ghosn, E.F. Carbajal, N. Befrui, V.V. Tuchin, K.V. Larin, Concentration effect on the diffusion of glucose in ocular tissues. Opt. Lasers Eng. **46**, 911–914 (2008)
247. E.A. Genina, A.N. Bashkatov, V.V. Tuchin, M. Ghosn, K.V. Larin, T.G. Kamenskikh, Cortexin diffusion in human eye sclera. Quantum Electron. **41**, 407–413 (2011)
248. M. Ghosn, N. Sudheendran, M. Wendt, A. Glasser, V.V. Tuchin, K.V. Larin, Monitoring of glucose permeability in monkey skin in vivo using optical coherence tomography. J. Biophotonics **3**, 25–33 (2010)
249. M.G. Ghosn, S.H. Syed, N.A. Befrui, M. Leba, A. Vijayananda, N. Sudheendran, K.V. Larin, Quantification of molecular diffusion in arterial tissues with optical coherence tomography and fluorescence microscopy. Laser Phys. **19**, 1272–1275 (2009)
250. M.G. Ghosn, E.F. Carbajal, N. Befrui, A. Tellez, J.F. Granada, K.V. Larin, Permeability of hyperosmotic agent in normal and atherosclerotic vascular tissues. J. Biomed. Opt. **13**, 010505-1–010505-3 (2008)
251. K.V. Larin, M.G. Ghosn, S.N. Ivers, A. Tellez, J.F. Granada, Quantification of glucose diffusion in arterial tissues by using optical coherence tomography. Laser Phys. Lett. **4**, 312–317 (2007)
252. M.G. Ghosn, M. Mashiatulla, S.H. Syed, M.A. Mohamed, K.V. Larin, J.D. Morrisett, Permeation of human plasma lipoproteins in human carotid endarterectomy tissues: measurement by optical coherence tomography. J. Lipid Res. **52**(7), 1429–1434 (2012)
253. M.G. Ghosn, M. Mashiatulla, M.A. Mohamed, S.H. Syed, F. Castro-Chavez, J.D. Morrisett, K.V. Larin, Time dependent changes in aortic tissue during cold storage in physiological solution. Biochim. Biophys. Acta **1810**, 555–560 (2011)
254. H.Q. Zhong, Z.Y. Guo, H.J. Wei, C.C. Zeng, H.L. Xiong, Y.H. He, S.H. Liu, Quantification of glycerol diffusion in human normal and cancer breast tissues in vitro with optical coherence tomography. Laser Phys. Lett. **7**(4), 315–320 (2010)
255. Z. Zhu, G. Wu, H. Wei, H. Yang, Y. He, S. Xie, Q. Zhao, X. Guo, Investigation of the permeability and optical clearing ability of different analytes in human normal and cancerous breast tissues by spectral domain OCT. J. Biophotonics **5**(5–6), 1–8 (2012). doi:10.1002/jbio.201100106
256. Q.L. Zhao, J.L. Si, Z.Y. Guo, H.J. Wei, H.Q. Yang, G.Y. Wu, S.S. Xie, X.Y. Li, X. Guo, H.Q. Zhong, L.Q. Li, Quantifying glucose permeability and enhanced light penetration in *ex vivo* human normal and cancerous esophagus tissues with optical coherence tomography. Laser Phys. Lett. **8**(1), 71–77 (2011)
257. Q. Zhao, Z. Guo, H. Wei, H. Yang, S. Xie, In vitro investigation hyperosmotic agents diffusion of different depths in normal and malignant human esophagus tissues by optical coherence tomography. Quantum Electron. **41**(10), 950–955 (2011)
258. L.S. de Melo, R.E. de Araujo, A.Z. Freitas, D. Zezell, N.D. Vieira, J. Girkin, A. Hall, M.T. Carvalho, A.S. Gomes, Evaluation of enamel dental restoration interface by optical coherence tomography. J. Biomed. Opt. **10**, 064027 (2005)

259. D.P. Popescu, M.G. Sowa, M.D. Hewko, L.P. Choo-Smith, Assessment of early demineralization in teeth using the signal attenuation in optical coherence tomography images. J. Biomed. Opt. **13**, 054053 (2008)
260. P. Wilder-Smith, L. Otis, J. Zhang, Z. Chen, Dental OCT, in *Optical Coherence Tomography*, ed. by W. Drexler, J.G. Fujimoto (Springer, Berlin/Heidelberg, 2008), pp. 1151–1182
261. N.A. Trunina, V.V. Lychagov, V.V. Tuchin, OCT monitoring of diffusion of water and glycerol through tooth dentine in different geometry of wetting. Proc. SPIE **7563**, 75630U-1–75630U-7 (2010)
262. N.A. Trunina, V.V. Lychagov, V.V. Tuchin, Study of water diffusion in human dentin by optical coherent tomography. Opt. Spectrosc. **109**(2), 162–168 (2010)
263. V.V. Tuchin, A.N. Bashkatov, E.A. Genina, V.I. Kochubey, V.V. Lychagov, S.A. Portnov, N.A. Trunina, D.R. Miller, S. Cho, H. Oh, B. Shim, M. Kim, J. Oh, H. Eum, Y. Ku, D. Kim, Y. Yang, Finger tissue model and blood perfused skin tissue phantom. Proc. SPIE **7898**, 78980Z-1–78980Z-10 (2011)
264. A. Kishen, S. Vedantam, Hydromechanics in dentine: role of dentinal tubules and hydrostatic pressure on mechanical stress-strain distribution. Dent. Mater. **23**, 1296–306 (2007)
265. C.T. Hanks, J.C. Fat, J.C. Wataha, J.F. Corcoran, Cytotoxicity and dentin permeability of carbamide peroxide and hydrogen peroxide vital bleaching materials, in vitro. J. Dent. Res. **72**, 931–938 (1993)
266. V.V. Tuchin (ed.), *Handbook of Optical Sensing of Glucose in Biological Fluids and Tissues* (CRC Press/Taylor & Francis Group, London, 2009)
267. K.V. Larin, V.V. Tuchin, Monitoring of glucose diffusion in epithelial tissues with optical coherence tomography, in *Handbook of Optical Sensing of Glucose in Biological Fluids and Tissues*, ed. by V.V. Tuchin (CRC Press/Taylor & Francis Group, London, 2009), pp. 623–656
268. A.N. Bashkatov, E.A. Genina, V.V. Tuchin, Measurement of glucose diffusion coefficients in human tissues, in *Handbook of Optical Sensing of Glucose in Biological Fluids and Tissues*, ed. by V.V. Tuchin (CRC Press/Taylor & Francis Group, London, 2009), pp. 587–621
269. E.A. Genina, A.N. Bashkatov, V.V. Tuchin, Glucose-induced optical clearing effects in tissues and blood, in *Handbook of Optical Sensing of Glucose in Biological Fluids and Tissues*, ed. by V.V. Tuchin (CRC Press/Taylor & Francis Group, London, 2009), pp. 657–692
270. K.V. Larin, M.G. Ghosn, V.V. Tuchin, Noninvasive assessment of molecular permeability with OCT, in *Handbook of Photonics for Biomedical Science*, ed. by V.V. Tuchin (CRC Press/Taylor & Francis Group, London, 2010), pp. 410–428
271. E.A. Genina, K.V. Larin, A.N. Bashkatov, V.V. Tuchin, Glucose and other metabolites sensing in skin, in *Handbook of Biophotonics, Vol. 2: Photonics for Health Care*, ed. by J. Popp, V. Tuchin, A. Chiou, S.H. Heinemann (Wiley, Weinheim, 2011), pp. 835–853
272. M. Kinnunen, R. Myllylä, T. Jokela, S. Vainio, In vitro studies toward noninvasive glucose monitoring with optical coherence tomography. Appl. Opt. **45**(10), 2251–2260 (2006)
273. M. Kinnunen, S. Tausta, R. Myllylä, S. Vainio, Monitoring changes in the scattering properties of mouse skin with optical coherence tomography during an in vivo glucose tolerance test. Proc. SPIE **6535**, 65350B-1–65350B-10 (2007)
274. M. Kinnunen, R. Myllylä, S. Vainio, Detecting glucose-induced changes in in vitro and in vivo experiments with optical coherence tomography. J. Biomed. Opt. **13**(2), 021111-1–021111-7 (2008)
275. A. Popov, A. Bykov, S. Toppari, M. Kinnunen, A. Priezzhev, R. Myllylä, Glucose sensing in flowing blood and intralipid by laser pulse time-of-flight and optical coherence tomography techniques. IEEE J. Sel. Top. Quantum Electron. **18**(4), 1335–1342 (2012)
276. P.D. Agrba, M.Y. Kirillin, A.I. Abelevich, E.V. Zagaynova, V.A. Kamensky, Compression as a method for increasing the informativity of optical coherence tomography of biotissues. Opt. Spectrosc. **107**, 853–858 (2009)

277. G.A. Askar'yan, The increasing of laser and other radiation transport through soft turbid physical and biological media. Sov. J. Quantum Electron. **9**, 1379–1383 (1982)
278. C. Drew, T.E. Milner, C.G. Rylander, Mechanical tissue optical clearing devices: evaluation of enhanced light penetration in skin using optical coherence tomography. J. Biomed. Opt. **14**, 064019 (2009)
279. A.A. Gurjarpadhye, W.C. Vogt, Y. Liu, C.G. Rylander, Effect of localized mechanical indentation on skin water content evaluated using OCT. Int. J. Biomed. Imaging **2011**, 817250 (2011)
280. N. Guzelsu, J.F. Federici, H.C. Lim, H.R. Chauhdry, A.B. Ritter, T. Findley, Measurement of skin stretch via light reflection. J. Biomed. Opt. **8**, 80–86 (2003)
281. A.P. Ivanov, S.A. Makarevich, A.Y. Khairulina, Propagation of radiation in tissues and liquids with densely packed scatterers. J. Appl. Spectrosc. **47**, 662–668 (1988)
282. M.Y. Kirillin, P.D. Agrba, V.A. Kamensky, In vivo study of the effect of mechanical compression on formation of OCT images of human skin. J. Biophotonics **3**, 752–758 (2010)
283. S. Nickell, M. Hermann, M. Essenpreis, T.J. Farrell, U. Kramer, M.S. Patterson, Anisotropy of light propagation in human skin. Phys. Med. Biol. **45**, 2873–2886 (2000)
284. P. Rol, P. Niederer, U. Dürr, P.-D. Henchoz, F. Fankhauser, Experimental investigation on the light scattering properties of the human sclera. Laser Light Ophthalmol. **3**, 201–212 (1990)
285. C.G. Rylander, O.F. Stumpp, T.E. Milner, N.J. Kemp, J.M. Mendenhall, K.R. Diller, A.J. Welch, Dehydration mechanism of optical clearing in tissue. J. Biomed. Opt. **11**, 041117 (2006)
286. H. Shangguan, S. Prahl, S.L. Jacques, L.W. Casperson, K.W. Gregory, Pressure effects on soft tissues monitored by changes in tissue optical properties. Proc. SPIE **3254**, 366–371 (1998)
287. Y.P. Sinichkin, N. Kollias, G. Zonios, S.R. Utz, V.V. Tuchin, Reflectance and fluorescence spectroscopy of human skin in vivo, in *Optical Biomedical Diagnostics*, ed. by V.V. Tuchin (SPIE Press, Bellingham, 2002), pp. 725–785
288. M.E. Brezinski, *Optical Coherence Tomography: Principles and Applications* (Academic, Amsterdam/Boston, 2006)
289. V.V. Tuchin, Optical clearing of tissue and blood using immersion method. J. Phys. D: Appl. Phys. **38**, 2497–2518 (2005)
290. V.V. Tuchin, Optical immersion as a new tool to control optical properties of tissues and blood. Laser Phys. **15**(8), 1109–1136 (2005)
291. V.V. Tuchin, A clear vision for laser diagnostics. IEEE J. Sel. Top. Quantum Electron. **13**(6), 1621–1628 (2007)
292. E.A. Genina, A.N. Bashkatov, V.V. Tuchin, Tissue optical immersion clearing. Expert Rev. Med. Devices **7**(6), 825–842 (2010)
293. V.V. Tuchin, R.K. Wang, A.T. Yeh, Optical clearing of tissues and cells. J. Biomed. Opt. **13**, 021101-1 (2008)
294. V.V. Tuchin, M. Leahy, D. Zhu, Optical clearing for biomedical imaging in the study of tissues and biological fluids. J. Innov. Opt. Health Sci. **3**(3) (2010). doi:10.1142/S1793545810001076
295. V.V. Tuchin, Tissue and blood optical properties control, in *Advances in Biophotonics*, ed. by B. Wilson, V. Tuchin, S. Tanev. NATO Science Series I. Life and Behavioural Sciences, vol. 369 (Ios Press, Amsterdam, 2005), pp. 79–122
296. S. Tanev, W. Sun, N. Loeb, V. Tuchin, The finite-difference time-domain approach and its application to the modelling of light scattering by biological cells in absorbing and controlled extra-cellular media, in *Advances in Biophotonics*, ed. by B. Wilson, V. Tuchin, S. Tanev. NATO Science Series I. Life and Behavioural Sciences, vol. 369 (Ios Press, Amsterdam, 2005), pp. 45–78
297. R.K. Wang, V.V. Tuchin, Optical tissue clearing to enhance imaging performance for OCT, in *Optical Coherence Tomography: Technology and Applications*, ed. by W. Drexler, J.G. Fujimoto (Springer, Berlin, 2008), pp. 851–882

298. E.A. Genina, A.N. Bashkatov, K.V. Larin, V.V. Tuchin, Light–tissue interaction at optical clearing, in *Laser Imaging and Manipulation in Cell Biology*, ed. by F.S. Pavone (Wiley, Weinheim, 2010)
299. S.G. Proskurin, I.V. Meglinski, Optical coherence tomography imaging depth enhancement by superficial skin optical clearing. Laser Phys. Lett. **4**(11), 824–826 (2007)
300. M. Bonesi, S.G. Proskurin, I.V. Meglinski, Imaging of subcutaneous blood vessels and flow velocity profiles by optical coherence tomography. Laser Phys. **20**(4), 891–899 (2010)
301. J. Wang, Y. Liang, S. Zhang, Y. Zhou, H. Ni, Y. Li, Evaluation of optical clearing with the combined liquid paraffin and glycerol mixture. Biomed. Opt. Express **2**(8), 2329–2338 (2011)
302. X. Wen, S.L. Jacques, V.V. Tuchin, D. Zhu, Enhanced optical clearing of skin in vivo and OCT in-depth imaging. J. Biomed. Opt. **17**, 066022 (2012)